

Electric Dipole Moments of the Atoms, Molecules, Nuclei and Particles

T.E. Chupp,¹ P. Fierlinger,² M.J. Ramsey-Musolf,³ and J.T. Singh⁴

¹*Department of Physics,
University of Michigan, Ann Arbor,
Michigan 48109 USA*

²*Physik Department and Excellence-Cluster "Universe",
Technische Universität München,
85748 Garching bei München,
Germany*

³*Amherst Center for Fundamental Interactions and Department of Physics,
University of Massachusetts-Amherst, Amherst,
Massachusetts 01003 USA*

⁴*National Superconducting Cyclotron Laboratory and Department of Physics & Astronomy,
Michigan State University East Lansing,
Michigan 48824 USA*

A permanent electric dipole moment (EDM) of a particle or system is a separation of charge along its angular-momentum axis and is a direct signal of T-violation and, assuming CPT symmetry, CP violation. For over sixty years EDMs have been studied, first as a signal of a parity-symmetry violation and then as a signal of CP violation that would clarify its role in nature and in theory. Contemporary motivations include the role that CP violation plays in explaining the cosmological matter-antimatter asymmetry and the search for new physics. Experiments on a variety of systems have become ever-more sensitive, but provide only upper limits on EDMs. Theory at several levels is crucial: elementary-particle phenomenology connects the Standard Model and the θ parameter in QCD that must be exceptionally small, which could be explained by the existence of axions, which may also be the dark-matter particles. Connections to electroweak baryogenesis conclude that new physics is needed to explain the dominance of matter in the universe; nuclear theory provides connections of Standard-Model and Beyond-Standard-Model physics to the observable EDMs, and atomic and molecular theory reveal how CP-violation is manifest at that scale. Experimental and theoretical efforts continue to expand with new ideas and new questions, and this review provides a broad overview of theoretical motivations and interpretations as well as details about experimental techniques, experiments, and prospects. The intent is to provide specifics and context as this exciting field moves forward.

PACS numbers: 07.55.Ge, 07.55.Nk, 2.10.Dk, 3.15.Kr, 11.30.Er, 12.15.Ji, 21.10.Ky, 29.25.Dz

CONTENTS

I. Introduction	2	A. The Neutron	32
A. Experimental landscape	3	Magnetometers for Neutron EDM Experiments	34
B. Theoretical interpretation	5	Neutron-EDM Systematics	34
C. Reach and complementarity	7	Neutron-EDM Prospects	37
D. EDMs and baryogenesis	7	B. Paramagnetic atoms: Cs and Tl	39
II. Theoretical background	8	C. Paramagnetic polar molecules: YbF, ThO and HfF ⁺	41
A. CP/T Violation	8	D. Solid-state systems	43
B. General Framework	9	E. Diamagnetic Atoms and molecules	44
C. Low-Energy Parameters	11	F. Octupole collectivity in diamagnetic systems	45
D. EDMs in the Standard Model	11	G. Other prospects: Storage ring EDMs	48
E. Beyond-Standard-Model Physics	13	V. Interpretations of current and prospective experiments	51
F. From theory to experiment	17	A. Sole source	51
III. Experimental techniques	19	B. Global Analysis	51
A. Magnetic shielding	21	Paramagnetic systems: limits on d_e and C_S	51
Cryogenic shields	23	Hadronic parameters and C_T	52
B. Magnetometers	24	VI. Summary and Conclusions	53
Rb and Cs magnetometers	25		
C. Magnetic field-coil design and current sources	26	Acknowledgments	55
D. Ultra-cold Neutron Sources	27	References	55
IV. Experiments	32		

I. INTRODUCTION

Measurements and interpretation of the permanent Electric Dipole Moments or EDMs of particles and quantum systems have been a unique window into the nature of elementary particle interactions from the very first proposal of Purcell and Ramsey (1950) to search for a neutron EDM as a signal of parity-symmetry (P) violation. The neutron EDM was not observed then or since, and we now recognize, as quickly pointed out by Lee and Yang (1957) and Landau (1957a,b,c), that EDMs also violate time-reversal symmetry (T). An EDM is a direct signal of T-violation, and the CPT theorem (C is charge conjugation) therefore implies that observation of a P-odd/T-odd EDM is also a signal of CP violation. EDMs have become a major focus of contemporary research for several interconnected reasons:

- i. EDMs provide a direct experimental probe of CP violation, a feature of the Standard Model (SM) and Beyond-Standard-Model (BSM) physics;
- ii. the P-violating and T-violating EDM signal distinguishes the much weaker CP-violating interactions from the dominant strong and electromagnetic interactions;
- iii. CP violation is a required component of Sakharov's recipe for the baryon asymmetry, the fact that there is more matter than antimatter in the universe; however Standard-Model CP violation cannot produce the observed asymmetry, and new CP-violating interactions are required.

The EDM of a classical system \vec{d} is the vector separating the center of charge from the center of mass. In a non-degenerate system, \vec{d} must be parallel (or antiparallel) to the angular momentum of the system $\langle \vec{J} \rangle$, where \vec{J} is the angular-momentum. Thus, relative to the center of mass ($\vec{r} = 0$):

$$\vec{d} = \int \vec{r} \rho_Q d^3r = d \frac{\langle \vec{J} \rangle}{J}, \quad (1)$$

where ρ_Q is the electric-charge distribution. This is analogous to the the magnetic dipole moment (Ramsey, 1956)

$$\vec{\mu} = \int \vec{r} \times \vec{J}_Q d^3r = \mu \frac{\langle \vec{J} \rangle}{J}, \quad (2)$$

where \vec{J}_Q is the current density.

The interaction of a fermion with magnetic moment μ and EDM d with electric and magnetic fields can be written

$$\mathcal{L}_{\mathcal{EM}} = -\frac{\mu}{2} \bar{\Psi} \sigma^{\mu\nu} F_{\mu\nu} \Psi - i \frac{d}{2} \bar{\Psi} \sigma^{\mu\nu} \gamma^5 F_{\mu\nu} \Psi, \quad (3)$$

where Ψ is the fermion field, and $F_{\mu\nu} = \partial_\mu A_\nu - \partial_\nu A_\mu$ is the electromagnetic field tensor with A_μ the four-vector electromagnetic potential. The second term of Eq. 3, first written down by Salpeter (1958) in analogy to the anomalous magnetic moment term, reveals parity and time-reversal violation in the Dirac matrix γ^5 and the imaginary number i , respectively. The corresponding non-relativistic Hamiltonian for a quantum system is

$$H = -(\vec{\mu} \cdot \vec{B} + \vec{d} \cdot \vec{E}) = -(\mu \vec{J} \cdot \vec{B} + d \vec{J} \cdot \vec{E})/J. \quad (4)$$

The magnetic field \vec{B} and the angular momentum operator \vec{J} are both even under P but odd under T, while the electric field \vec{E} is odd under P but even under T. The second term, proportional to $\vec{J} \cdot \vec{E}$ is thus P-odd and T-odd, and a direct signal of CP violation.

A common approach to measuring an EDM is to apply a strong electric field and very well controlled and characterized magnetic field and to measure the shift in the energy, or more commonly the frequency of the splitting between magnetic sub-levels (*e.g.* often $|\Delta m_J| = 1$) when \vec{E} is changed. For a system with total angular momentum J , the EDM frequency shift for two levels is

$$|\Delta f| = \frac{|dE|}{2\pi\hbar J} |\Delta m_J| = 1. \quad (5)$$

The precision of a single frequency measurement depends on the interrogation time τ and the signal-to-noise ratio (SNR) for the measurement. The SNR depends on the specifics of the technique. For a count-rate-limited experiment, the statistical uncertainty of a single frequency measurement is given by $\sigma_f = 1/(2\pi\tau\sqrt{N})$ for N particle measured or interrogated. In phase-noise-limited experiments, for example those using a SQUID magnetometer, the frequency precision is limited the combination of the intrinsic noise density v_n of the device and the finite bandwidth $B = 1/\tau$ of the measurement. In these cases, the statistical uncertainty of a single frequency measurement is given by $\sigma_f = (\sqrt{3}v_n)/(2\pi V_0\tau^{3/2})$ for a constant signal size V_0 , and the SNR is given by $V_0/(v_n\tau)$ (for example see Chupp *et al.* (1994) or Chibane *et al.* (1995)). For a decaying signal, σ_f increases by a factor of order one, which depends on τ and the decay time-constant. The EDM sensitivity for a **pair** of frequency measurements with opposite electric field each lasting a time τ therefore scales as

$$\begin{aligned} \sigma_d &= \frac{\hbar J}{2\sqrt{2}E} \frac{1}{\sqrt{N}} \tau^{-1} & (\text{counting}) \\ \sigma_d &= \sqrt{\frac{3}{2}} \frac{\hbar J}{E} \frac{v_n}{V_0} \tau^{-3/2} & (\text{phase noise}) \end{aligned} \quad (6)$$

This shows that the experimental challenges are to have the largest possible electric field magnitude E , the longest possible coherence or observation time τ and the highest possible number of particles N or SNR V_0/v_n as well as an ideally small, stable and well characterized magnetic

field to suppress frequency fluctuations due to changes in the magnetic moment interaction $\vec{\mu} \cdot \vec{B}$. Experimenters also strive to find systems in which the EDM is in some way enhanced, basically due to the a large intrinsic (P-even, T-even) electric dipole moment and increased electric polarizability of the system, which is the case for a molecule or atomic nucleus with octupole collectivity. To date, all experimental EDM searches (see Table I) including the neutron, atoms (Cs, Tl, Xe, Hg and Ra) and molecules (TlF, YbF, ThO and HfF⁺) have results consistent with zero but also consistent with the Standard Model.

Figure 1 illustrates the scope of this review, showing the connections from a fundamental theory including the Standard Model and Beyond-Standard-Model physics through a series of theory levels at different energy scales to the experimentally accessible observables – EDMs – in a variety of systems. Standard-Model CP violation arises from a complex phase in the Cabibbo-Kobayashi-Maskawa (CKM) matrix parameterizing the weak interaction (Kobayashi and Maskawa, 1973) and in the gluon $G\tilde{G}$ contribution to the strong interaction, which is proportional to the parameter θ (Callan *et al.*, 1976; 't Hooft, 1976; Jackiw and Rebbi, 1976). The CKM contribution to any observable EDM is many orders of magnitude smaller than current upper limits, providing a window of opportunity for discovering EDMs that arise from a non-zero θ or Beyond-Standard-Model physics. In contrast to CKM-CP violation, contributions of Beyond-Standard-Model physics need not be suppressed unless the CP-violating parameters themselves are small, or the mass scales are high.

New Beyond-Standard-Model interactions are also required for baryogenesis to account for the cosmic matter-antimatter asymmetry. EDMs provide a particularly important connection to baryogenesis if the CP-violation energy scale is not too high compared to the scale of electroweak symmetry-breaking, and if the responsible P-odd/T-odd interactions are flavor diagonal (Morrissey and Ramsey-Musolf, 2012).

This review is intended as a broad summary of how EDM experiment and theory have reached this point and how it will progress. To do so the motivations and impact of EDM measurements along with a context for interpreting the results in terms of a set of P-odd/T-odd low-energy parameters are presented in Sec. II. State-of-the-art experimental techniques and improvements that will drive progress are presented in some detail in Sec. III followed by a review of the current status of all experiments and prospects for new and improved approaches. The interpretation of these experiments and the impact of improvements in the context of the low energy theory parameters is presented in Sec V. The conclusions emphasize what will be necessary from both theory and experiment for continued progress and, perhaps the discovery of an EDM.

We also draw attention to several from a long list of important and classic reviews that include or are fully devoted to EDMs by Garwin and Lederman (1959), Ramsey (1982), Ramsey (1990), Bernreuther and Suzuki (1991a), Commins (1993), Golub and Lamoreaux (1994), Khriplovich and Lamoreaux (1997), Commins (1999), Sandars (2001), Ginges and Flambaum (2004), Pospelov and Ritz (2005), Commins (2007), Dubbers and Schmidt (2011), Engel *et al.* (2013), and Roberts *et al.* (2015).

A. Experimental landscape

The neutron was the the objective of the early direct EDM measurements of Smith, Purcell and Ramsey due to the reasoning that it was a neutral hadronic (weakly interacting) system and would not be accelerated from the measurement region by a large static electric field (Purcell and Ramsey, 1950; Smith *et al.*, 1957). The early neutron-EDM measurements, culminating in 1977 used molecular-beam techniques developed to measure the neutron magnetic moment, which limited the observation time for a neutron transiting a meter-scale apparatus to milliseconds and line-widths of hundreds of Hz or more. The beam approach also had significant limitations due to a number of systematic effects including the interaction of the neutron magnetic moment with the motional magnetic field ($\vec{E} \times \vec{v}/c^2$) and leakage currents, both of which shifted the energy when the electric field was changed (Dress *et al.*, 1977). By 1980, advances in ultra-cold neutron (UCN) production at Institute Laue-Langevin (ILL) in Grenoble, France, enabled storage of neutrons in a “cell,” which mitigated the motional effects, leading to a series of increasingly precise neutron EDM measurements, which are discussed in section IV.A. As the rate of UCN production improved, leading to smaller statistical errors, the control of the magnetic field required advances in magnetic shielding and magnetometry discussed in Sec III. Comagnetometry, the use of a second species less sensitive to CP-violation but with a similar magnetic moment in the same measurement volume and at the same time mitigated magnetic-field instability and a number of systematic effects. The neutron-EDM experiments are rate/statistics limited with typically only a few thousand UCNs per measurement cycle, and advances require new UCN sources, which are discussed in detail in Sec III.D, and corresponding improvements to magnetic shielding, magnetometry and understanding of systematic effects.

The earliest limits on the proton and electron EDMs were established by studies of corrections to the Lamb shift in hydrogen (Feinberg, 1958; Sternheimer, 1959) and scattering of electrons from helium (Goldemberg, 1963). Starting in the 1960’s, experimenters turned their attention to stable atoms and molecules. It was recognized that these systems provided a rich set of possible contri-

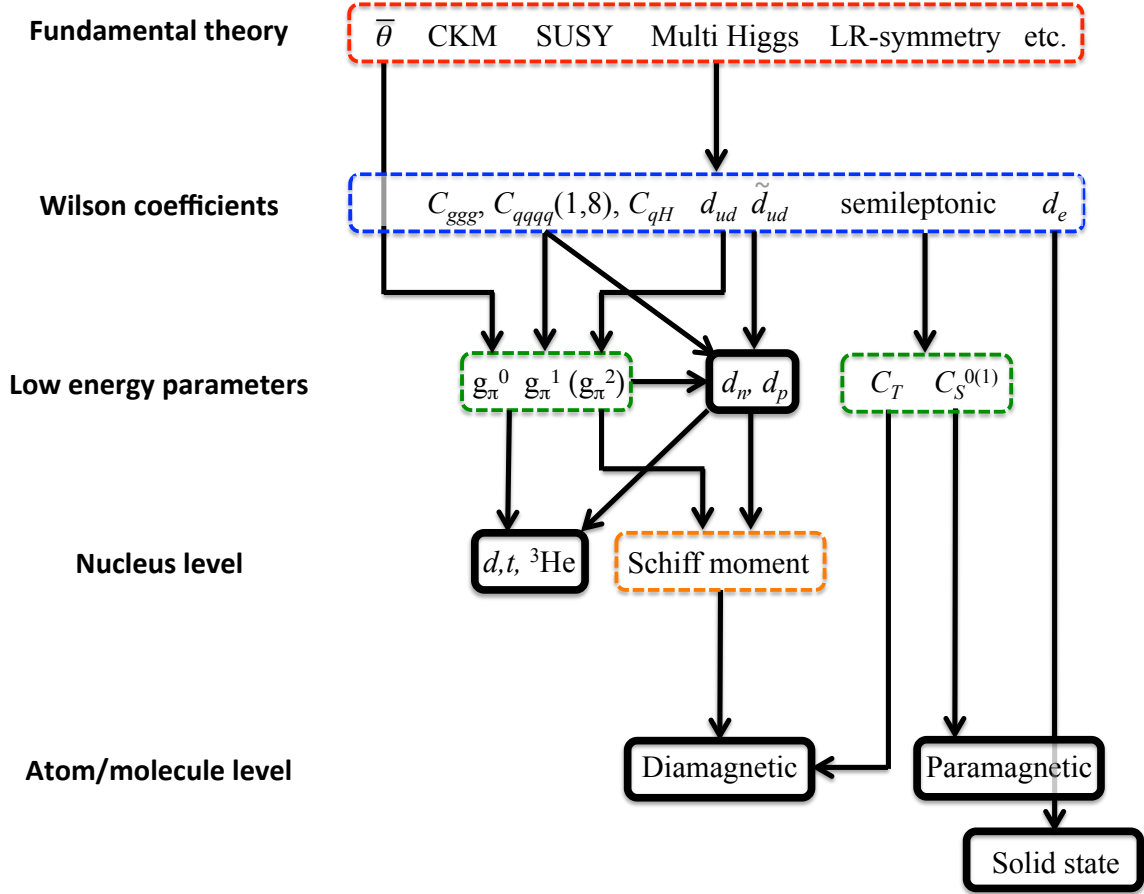


FIG. 1 (Color online) Illustration of the connections from a fundamental theory to an EDM in a measurable system. The dashed boxes indicate levels dominated by theory, and the solid boxes identify systems that are the object of current and future experiments. The fundamental CP-violating Lagrangian at the top, a combination of Standard Model and Beyond-Standard-Model physics, is reduced to the set of effective-field-theory Wilson coefficients that characterize interactions at the electroweak energy scale of ≈ 300 GeV, the vacuum-expectation value of the Higgs. The set of low-energy parameters defined in Sec. II enter calculations that connect the electroweak-scale Wilson coefficients directly to electrons and nuclei. Finally atomic, molecular and condensed-matter structure calculations connect the low-energy parameters to the observables in experimentally accessible systems.

butions to the P-odd/T-odd observables, but the charged constituents, the electron and nucleus, are significantly shielded from the large external field by the polarization of the atom. This is embodied in Schiff's theorem (Schiff, 1963), which states that for a bound system of point-like charged particles the net force and the net electric field at the position of each charged particle is exactly zero. The shielding is not perfect in the case of a nucleus of finite size and in the case of unpaired electron (paramagnetic systems) due to relativistic effects (Commins *et al.*, 2007). In fact for paramagnetic atoms there is an effective enhancement of the sensitivity to an electron EDM that is approximately $10Z^3\alpha^2$ as explained by Sandars (1965, 1966, 1968a,b). Moreover, an atomic EDM can arise due

to T and P violation in the electron-nucleus interaction that may have a scalar or tensor nature, and these effects also increase with Z . For these reasons EDM searches expanded to atomic and molecular beams in early experiments pioneered by Sandars and Lipworth (1964).

Paramagnetic systems with one or more unpaired electrons (Cs, Tl, YbF, ThO, HfF^+ *etc.*) are most sensitive to both the electron EDM d_e and the nuclear spin-independent component of the electron-nucleus coupling (C_S), which are likely to be several orders of magnitude stronger than tensor and pseudoscalar contributions, given comparable strength of the intrinsic couplings (Ginges and Flambaum, 2004). Diamagnetic systems, including ^{129}Xe , ^{199}Hg and ^{225}Ra atoms, the

molecule TIF are most sensitive to purely hadronic CP-violating sources that couple through the Schiff moment, the r^2 -weighted dipole distribution

$$S = \frac{1}{10} \langle r^2 \vec{\tau}_p \rangle - \frac{1}{6} Z \langle r^2 \rangle \langle \vec{r}_p \rangle. \quad (7)$$

The second term is proportional to the EDM of the nucleus, which is unobservable in a neutral atom and therefore subtracted. The Schiff-moment distribution is probed by the molecular electrons through the interaction

$$H = -4\pi \vec{\nabla} \rho(0) \cdot \vec{S}, \quad (8)$$

where $\vec{\nabla} \rho(0)$ is the gradient of the electron density at the nucleus. Flambaum and Ginges (2002) have shown that an effective model of the effect of the Schiff moment is a constant electric field along the spin of the nucleus so that as the atomic electrons penetrate the nucleus, the force moves the electron cloud with respect to the atom's center of mass and induces an EDM along the spin. (We note that Schiff's Theorem has been recently reformulated in work showing that these formulas may be approximations that may not be justified (Liu, 2007); however, there is not agreement on the validity of this reformulation (Sen'kov, 2008).) In addition, the EDM of a diamagnetic system can arise due to the tensor component of the electron-nucleus coupling C_T for atoms and molecules. The electron EDM and C_S contribute to the diamagnetic atoms in higher order. The magnetic quadrupole moment, a P-odd and T-odd distribution of currents in the nucleus is not shielded in the same way as electric moments and induces an atomic EDM by coupling to an unpaired electron (Derevianko, 2005). The magnetic quadrupole moment requires a paramagnetic atom with nuclear spin $I > 1/2$, and cesium is the only experimental system so far that meets these requirements. Murthy *et al.* (1989) have presented an analysis of their experiment on cesium that extracts the magnetic quadrupole moment.

EDM searches are not confined to neutral systems. Charged particles and ions can be contained in storage rings or with time-dependent fields, for example, the paramagnetic molecular ion HfF^+ was stored with a rotating electric field (Cairncross *et al.*, 2017), and the EDM of the muon was measured in conjunction with the $g - 2$, magnetic-moment anomaly measurements at Brookhaven (Bennett *et al.*, 2006). In the muon experiment, spin-precession due to the EDM coupling to the motional electric field ($\vec{v} \times \vec{B}$) was measured, and an upper limit on d_μ was reported (Bennett *et al.*, 2009). Though not a dedicated EDM measurement, the technique has demonstrated the possibility of a significantly improved measurement, which is motivated by theoretical suggestions that the fundamental leptons' sensitivity to CP-violation may scale with a power of the lepton mass (Babu *et al.*, 2001). Storage-ring EDM searches

have also been proposed for light nuclei, *i.e.* the proton, deuteron and $^3\text{He}^{++}$ - the helion (Rathmann *et al.*, 2013a). The electron EDM can also be measured in special ferro-electric and paramagnetic solid-state systems with quasi-free electron spins that can be subjected to applied electric and magnetic fields (Eckel *et al.*, 2012). We also note that the EDM of the Λ hyperon was measured in a spin-precession measurement (Pondrom *et al.*, 1981), and that limits on the τ lepton EDM and on neutrino EDMs have been derived, and are discussed, for example by Commins (1999, 2007).

A compilation of experimental results is presented in Table I, which separates paramagnetic (electron-spin dependent) systems from diamagnetic (nuclear and nucleon spin-dependent) systems, which are most sensitive to hadronic effects and nuclear-spin-dependent semi-hadronic contributions. In order to cast all results consistently, we have expressed the upper limits (u.l.) at 95% confidence levels.

B. Theoretical interpretation

The results on EDMs presented in Table I have significant theoretical impact in several contexts by constraining explicit parameters of Standard Model and Beyond-Standard-Model physics. The Standard Model has two explicit CP-violating parameters: the phase in the CKM matrix, and the coefficient $\bar{\theta}$ operator in the SM strong interaction Lagrangian. EDMs arising from the CKM-matrix vanish up to three-loops for the electron (Bernreuther and Suzuki, 1991b) and up to two loops for quarks (Shabalin, 1978, 1983). The leading contributions to the neutron EDM, however, arise from a combination of hadronic one-loop and resonance contributions, each a combination of two $\Delta S = 1$ hadronic interactions (one CP violating and one CP-conserving). The CP-violating $\Delta S = 1$ vertex is, itself, a one-loop effect, arising from the QCD ‘‘Penguin’’ process (See Fig. 2). The estimate of the corresponding neutron EDM is $(1 - 6) \times 10^{-32}$ e-cm (Seng, 2015), where the range reflects the present hadronic uncertainties. For both the electron and the neutron, the Standard-Model CKM contribution lies several orders of magnitude below the sensitivities of recent and next-generation EDM searches. The Penguin process generated by the exchange of a kaon between two nucleons induces CP-violating effects in nuclei; however Donoghue *et al.* (1987) and others show that this contribution is also many orders of magnitude below current experimental sensitivity for diamagnetic atom EDMs (Yamanaka and Hiyama, 2016). EDMs of the neutron and atoms also uniquely constrain the Standard-Model strong-interaction parameter $\bar{\theta}$ which sets the scale of strong CP violation as discussed in Sec. II).

Beyond-Standard-Model theories generally provide new degrees of freedom and complex CP-violating cou-

	Result	95% u.l.	ref.
Paramagnetic systems			
Xe ^m	$d_A = (0.7 \pm 1.4) \times 10^{-22}$	3.1×10^{-22} e-cm	<i>a</i>
Cs	$d_A = (-1.8 \pm 6.9) \times 10^{-24}$	1.4×10^{-23} e-cm	<i>b</i>
	$d_e = (-1.5 \pm 5.7) \times 10^{-26}$	1.2×10^{-25} e-cm	
	$C_S = (2.5 \pm 9.8) \times 10^{-6}$	2×10^{-5}	
	$Q_m = (3 \pm 13) \times 10^{-8}$	$2.7 \times 10^{-7} \mu_N R_{Cs}$	
Tl	$d_A = (-4.0 \pm 4.3) \times 10^{-25}$	1.1×10^{-24} e-cm	<i>c</i>
	$d_e = (-6.9 \pm 7.4) \times 10^{-28}$	1.9×10^{-27} e-cm	
YbF	$d_e = (-2.4 \pm 5.9) \times 10^{-28}$	1.2×10^{-27} e-cm	<i>d</i>
ThO	$\omega^{NE} = 2.6 \pm 5.8$ mrad/s		<i>e</i>
	$d_e = (-2.1 \pm 4.5) \times 10^{-29}$	9.7×10^{-29} e-cm	
	$C_S = (-1.3 \pm 3.0) \times 10^{-9}$	6.4×10^{-9}	
HfF ⁺	$2\pi f^{BD} = 0.6 \pm 5.6$ mrad/s		<i>f</i>
	$d_e = (0.9 \pm 7.9) \times 10^{-29}$	16×10^{-29} e-cm	
Diamagnetic systems			
¹⁹⁹ Hg	$d_A = (2.2 \pm 3.1) \times 10^{-30}$	7.4×10^{-30} e-cm	<i>g</i>
¹²⁹ Xe	$d_A = (0.7 \pm 3) \times 10^{-27}$	6.6×10^{-27} e-cm	<i>h</i>
²²⁵ Ra	$d_A = (4 \pm 6) \times 10^{-24}$	1.4×10^{-23} e-cm	<i>i</i>
TlF	$d = (-1.7 \pm 2.9) \times 10^{-23}$	6.5×10^{-23} e-cm	<i>j</i>
n	$d_n = (-0.21 \pm 1.82) \times 10^{-26}$	3.6×10^{-26} e-cm	<i>k</i>
Particle systems			
μ	$d_\mu = (0.0 \pm 0.9) \times 10^{-19}$	1.8×10^{-19} e-cm	<i>l</i>
Λ	$d_\Lambda = (-3.0 \pm 7.4) \times 10^{-17}$	7.9×10^{-17} e-cm	<i>m</i>

TABLE I Systems with EDM results and the most recent results as presented by the authors. When d_e is presented by the authors, the assumption is $C_S = 0$, and for ThO, the C_S result assumes $d_e = 0$. Q_m is the magnetic quadrupole moment, which requires a paramagnetic atom with nuclear spin $I > 1/2$. (μ_N and R_{Cs} are the nuclear magneton and the nuclear radius of ¹³³Cs, respectively.) We have combined statistical and systematic errors in quadrature for cases where they are separately reported by the experimenters. References; *a* (Player and Sandars, 1970); *b* (Murthy *et al.*, 1989); *c* (Regan *et al.*, 2002a); *d* (Hudson *et al.*, 2011); *e* (Baron *et al.*, 2014); *f* (Cairncross *et al.*, 2017); *g* (Graner *et al.*, 2016); *h* (Rosenberry, 2001); *i* (Parker *et al.*, 2015); *j* (Cho, 1991); *k* (Pendlebury *et al.*, 2015); *l* (Bennett *et al.*, 2009); *m* (Pondrom *et al.*, 1981).

plings that often induce EDMs at the one-loop level. The most widely-considered BSM scenarios for which implications have been analyzed include supersymmetry (Pospelov and Ritz, 2005; Ramsey-Musolf and Su, 2008), the two-Higgs model (Inoue *et al.*, 2014), and left-right symmetric models.

A complementary, model-independent framework for EDM interpretation relies on effective field theory (EFT), presented in detail Section (Sec II.F). The EFT approach assumes that the Beyond-Standard-Model particles are sufficiently heavy that their effects can be compiled into a set of residual weak-scale, non-renormalizable operators involving only Standard-Model fields. The corresponding operators are dimension six and effectively depend on $(v/\Lambda)^2$, where $v = 246$ GeV is the Higgs vacuum-expectation-value and Λ is the energy scale of the new physics. The strength of each operator's contribution

is characterized by a corresponding Wilson coefficient. There are twelve dimension-6 Beyond-Standard-Model Wilson coefficients in all representing the intrinsic electron and quark EDMs (3), quark chromo-EDMs (2), a CP-violating three gluon operator (1), four-fermion operators (5), and a quark-Higgs boson interaction (1) - plus θ . Experimental EDM results constrain the Wilson coefficients, while a given Beyond-Standard-Model theory provides predictions for the Wilson coefficients in terms of the underlying model parameters.

Interactions involving light quarks and gluons are, of course, not directly accessible to experiment. Consequently, it is useful to consider their manifestation in a lower energy effective theory below the hadronic scale, $\Lambda_{\text{had}} \sim 1$ GeV, involving electrons, photons, pions, and nucleons. Hadronic matrix elements of the quark and gluon EFT operators then yield the hadronic operator coefficients. At lowest non-trivial order, one obtains the electron EDM (d_e); scalar, pseudoscalar, and tensor electron-nucleon interactions (C_S , C_P , and C_T , respectively¹); short-range neutron and proton EDMs (\bar{d}_n^{sr} and \bar{d}_p^{sr}); isoscalar, isovector, and isotensor pion-nucleon couplings ($\bar{g}_\pi^{(i)}$, $i = 0, 1, 2$); and a set of four-nucleon operators. In the context of this hadronic-scale EFT, it is appropriate to express the combination of contributions to a measured atomic EDM for paramagnetic, diamagnetic and nucleons as

$$d_i = \sum_j \alpha_{ij} C_j, \quad (9)$$

where i labels the system, and j labels the specific low-energy parameter (*e.g.*, d_e , C_S , *etc.*). The $\alpha_{ij} = \partial d_i / \partial C_j$ are provided by theoretical calculations at various scales from atomic to nuclear to short-range and are presented in Sec. II. Note that the coefficients α_{ij} have various labels in the literature for notation developed for the different experimental systems.

One approach to interpreting the experimental limits assumes that the EDM in a specific system arises from only one source – the “sole-source” approach. In the sole-source approach, the constraint on each parameter is derived assuming that all other contributions are negligible and so one experimental result may appear to set limits on a large number of individual CP-violating parameters. An alternative approach – the global analysis presented in Chupp and Ramsey-Musolf (2015) and Sec. V – assumes simultaneous non-zero values of the dominant parameters globally constrained by the experimental results. In the global analysis, paramagnetic systems are used to set limits on the electron EDM d_e

¹ Each interaction has an isoscalar and isovector component, which we have suppressed here for notational simplicity.

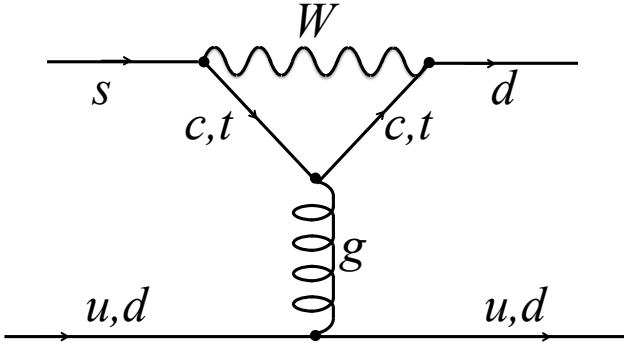


FIG. 2 Penguin diagram giving the Standard Model CKM $\Delta S = 1$ CP-violating effective interaction. Adapted from Pospelov and Ritz (2005).

and the nuclear spin-independent electron-nucleus coupling C_S . Diamagnetic systems set limits on four dominant parameters: two pion-nucleon couplings ($\bar{g}_\pi^{(0)}, \bar{g}_\pi^{(1)}$), a specific isospin combination of nuclear spin-dependent couplings, and the a “short distance” contribution to the neutron EDM, \bar{d}_n^{sr} . There is, unfortunately, significant variation and uncertainty in the α_{ij} , in particular for the nuclear and hadronic calculations, which lead to softening the constraints on the low-energy parameters.

C. Reach and complementarity

EDMs arising from Beyond-Standard-Model CP violation depend on a combination of factors, including new CP-violating phases, ϕ_{CPV} , the mass scale Λ associated with the new particles, and the underlying dynamics. In general, an elementary fermion EDM can be expressed as

$$d \approx (10^{-16} \text{e} - \text{cm}) \left(\frac{v}{\Lambda} \right)^2 (\sin \phi_{\text{CPV}})(y_f F) \quad , \quad (10)$$

where $v = 246$ GeV is the Higgs vacuum expectation value, y_f is a Yukawa coupling typically associated with the Standard-Model fermions in the system of interest, and F encodes the dynamics, which may be perturbative or non-perturbative and will differ depending on the system. For an electron EDM that arises through perturbative dynamics at the one-loop level, $F \sim g^2/(16\pi^2)$ where g is the Beyond-Standard-Model coupling strength. The present electron EDM upper limit of $\approx 1 \times 10^{-28}$ e-cm implies that $\Lambda \gtrsim 1 - 2$ TeV for g of order the Standard-Model $\text{SU}(2)_L$ gauge coupling strength, and $\sin \phi_{\text{CPV}} \approx 1$. This energy scale for Λ , which is comparable to the reach of the neutron and diamagnetic atom EDM limits, rivals the Beyond-Standard-Model physics reach of the LHC. It is important to note that exceptions to these naïve estimates of mass scale sensitivity can occur, for example at the level of the underlying elementary particle physics, an EDM may be enhanced by contributions of heavy fermion intermediate states, *e.g.*, the top

quark, leading to the presence of a larger Yukawa coupling in Eq. (10). In paramagnetic atoms and molecules an EDM may also be generated by a nuclear-spin independent scalar T-odd/P-odd electron-quark interaction at tree-level, which generally scales with the number of nucleons. In this case, the resulting mass reach for current experimental sensitivities is as high as $\sim 13,000$ TeV, as discussed in Section V. Models that generate EDMs at two-loop or higher-loop order allow for lighter Beyond-Standard-Model particles with CP-violating interactions.

For the Schiff moment, the additional power of r^2 in Eq. (7) implies that for a given underlying source of CP-violation, the contribution to a diamagnetic atomic or molecular EDM is suppressed compared to that of the neutron by $(R_N/R_A)^2$, where R_N and R_A are the nuclear and atomic radii, respectively. As a concrete illustration the bound on $\bar{\theta}$ arising from the ^{199}Hg EDM limit is comparable to the bound from d_n , even though the respective EDM limits differ by nearly four orders of magnitude (see Table I).

An example of unique constraints set by of EDM searches is found in the strong CP contribution to the neutron EDM given by Crewther *et al.* (1979) and Pospelov and Ritz (1999) and Shindler *et al.* (2015)

$$d_n \approx (10^{-16} \text{e} - \text{cm}) \bar{\theta} \quad . \quad (11)$$

The parameter $\bar{\theta}$ is naïvely expected to be of order unity; however assuming this is the only contribution to the neutron EDM, the current upper bound, from Table I implies $|\bar{\theta}| \lesssim 10^{-10}$. The corresponding bound obtained from the ^{199}Hg EDM limit is comparable. This severe constraint on $\bar{\theta}$ has motivated a variety of theoretical explanations, the most widely considered is the existence of a spontaneously-broken Peccei-Quinn symmetry and an associated particle - the axion. The axion is also a candidate for the observed relic density of cold dark matter. The axion proposal has been very compelling and has spawned a number of experimental endeavors summarized, for example by Asztalos *et al.* (2010).

D. EDMs and baryogenesis

Baryogenesis, the generation of a net asymmetry of matter over antimatter in the early universe, requires three components as first explained by Sakharov (1991): 1) departure from thermodynamic equilibrium (assuming CPT invariance), 2) violation of baryon number and 3) both C-violating and CP-violating processes. A number of baryogenesis scenarios that satisfy these requirements have been proposed, each typically focusing on a certain era in cosmic history and corresponding energy scale. Among the most widely considered and experimentally testable is electroweak baryogenesis. For a recent review of electroweak baryogenesis,

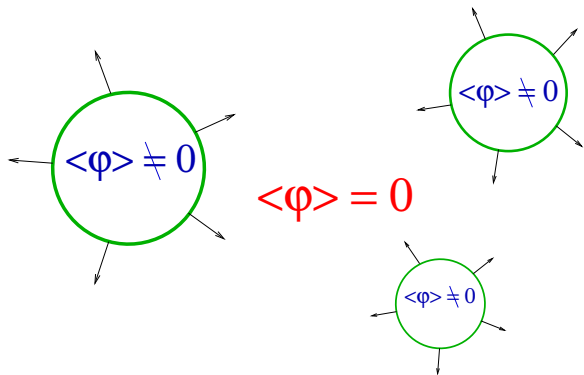


FIG. 3 (Color online) Bubble nucleation during first order electroweak phase transition. Figure © IOP Publishing Ltd and Deutsche Physikalische Gesellschaft; reproduced from Morrissey and Ramsey-Musolf (2012) by permission of IOP Publishing.

see Morrissey and Ramsey-Musolf (2012); see also Riotto and Trodden (1999) and Dine and Kusenko (2003) for more general baryogenesis reviews. In this scenario, the universe proceeds from initial conditions of a hot, radiation-dominated plasma containing zero net baryon number in which $SU(2)_L \times U(1)_Y$ electroweak symmetry has not yet been broken by the Higgs mechanism and the Higgs vacuum-expectation value is $\langle\phi_H\rangle = 0$. As the plasma cools below the electroweak scale ($\approx 100\text{GeV}$), the Higgs field takes on a non-zero vacuum-expectation value ($\langle\phi_H\rangle \neq 0$), thereby breaking electroweak symmetry. This requires that the phase transition be first-order associated with the nucleation of broken phase bubbles in the background symmetric phase. C-violating and CP-violating interactions at the bubble walls bias electroweak sphalerons² in the $\langle\phi_H\rangle = 0$ phase into making a net $B + L$ charge that diffuses into the $\langle\phi_H\rangle \neq 0$ bubbles. Sphaleron transitions inside the bubbles must be sufficiently quenched (*i.e.*, the transition must be “strongly first order”) in order to preserve the $B + L$ asymmetry. The bubbles containing the $B + L$ asymmetry expand, collide, and eventually coalesce into the universe that persists to the present epoch as illustrated in Fig. 3.

In principle, the Standard Model with CP-violation from the CKM matrix provides all of the ingredients for this scenario; however the phase transition cannot be first order for a Higgs mass greater than $\sim 70\text{ GeV}$. Given the observed Higgs mass $m_H = 125.09 \pm 0.24\text{ GeV}$ (Aad *et al.*, 2015), a first order phase transition cannot have occurred in a purely SM universe. Even if the value of m_H were small enough to accommodate a first order electroweak phase transition, the effects of CKM CP-violation are too feeble to have resulted in the observed

matter-antimatter asymmetry. Thus, electroweak baryogenesis requires BSM physics for two reasons: generation of a strong, first order electroweak phase transition and production of sufficiently large CP-violating asymmetries during the transition. New particle searches at colliders may discover new interactions responsible for the a first-order phase transition (Assamagan *et al.*, 2016; Contino *et al.*, 2016), but it is EDMs that provide the most powerful probe of the new CP-violating interactions.

Electroweak baryogenesis provides an additional constraint on the Beyond-Standard-Model mass scale Λ and on CP-violating phase(s) that set the scale of EDMs. Eq. 10 shows that experimental limits on EDMs constrain the ratio $\sin\phi_{\text{CPV}}/\Lambda^2$ but do not separately constrain Λ and $\sin\phi_{\text{CPV}}$; however the requirements for electroweak baryogenesis do provide complementary constraints on the mass scale and CP-violating phases. We illustrate this in Fig. 4 from Li *et al.* (2009), which shows constraints on parameters of the minimal supersymmetric Standard Model (MSSM) needed to generate the observed matter-antimatter asymmetry and the corresponding EDMs that would arise. The horizontal and vertical axes give the soft SUSY-breaking *bino* mass parameter M_1 and the CP-violating “bino phase” $\sin(\Phi_M) = \sin\text{Arg}(\mu M_1 b^*)$. The green band shows the relationship between these parameters needed to produce the matter-antimatter asymmetry, while the nearly horizontal lines indicate values of the neutron (left panel) and electron (right panel) EDMs. The EDMs have been computed in the limit of heavy *sfermions*, so that EDMs arise from two-loop graphs containing the electroweak *gauginos*. Note that the present d_e limit roughly excludes the region $d_e > 10^{-28}\text{ e-cm}$, while the current neutron-EDM bound does not yet constrain the indicated parameter space. The next generation electron and neutron EDM experiments are expected to probe below $d_e < 10^{-29}\text{ e-cm}$ and $d_n < 10^{-27}\text{ e-cm}$.

II. THEORETICAL BACKGROUND

A. CP/T Violation

Parity (P), Time Reversal (T) and Charge Conjugations (C) are the discrete symmetry transformations of quantum mechanics and quantum field theory. Experiment shows that the strong and electromagnetic interactions are symmetric under C, P and T separately and under CP and T, but that the weak interaction is maximally antisymmetric under P and C involving only left-handed neutrinos and right-handed antineutrinos. CP is also violated in weak decays of kaons and b-mesons. Symmetry under the combined transformations of C, P and T or CPT is consistent with experiment and is also required for any Lorentz-invariant quantum field theory as embodied in the CPT theorem (Jost, 1957; Lüders, 1954;

² An electroweak sphaleron is a static gauge-Higgs field configuration associated with a saddle point of the energy functional (Klinkhamer and Manton, 1984).

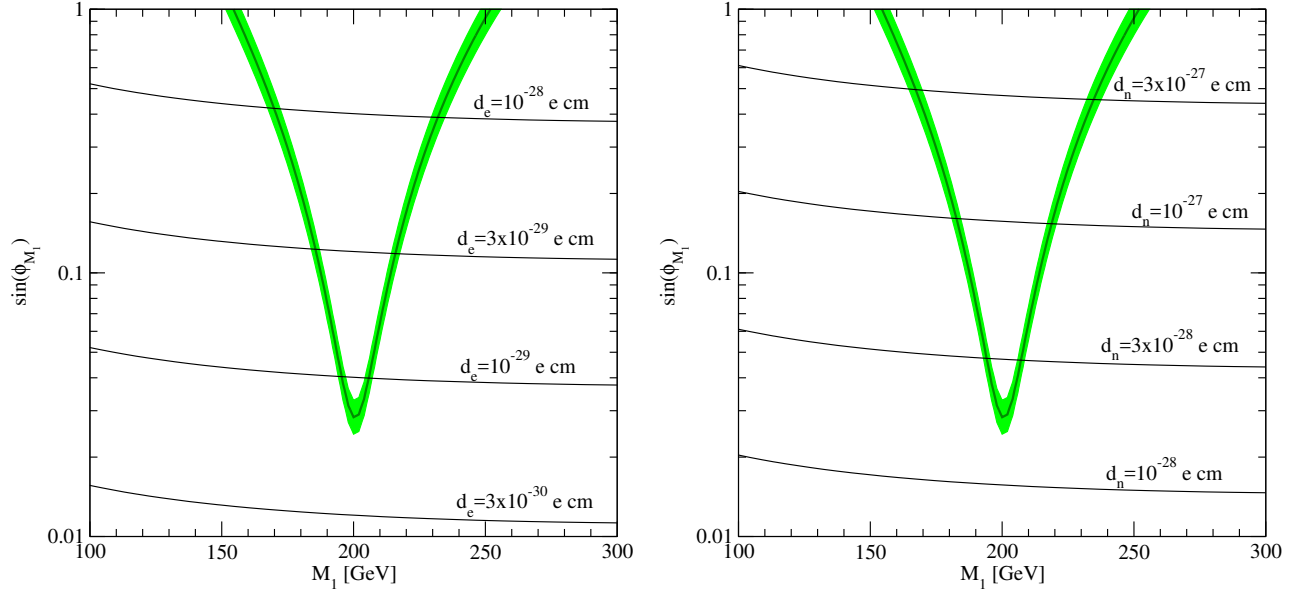


FIG. 4 (Color online) Sensitivity of the electron EDM (left panel) and neutron EDM (right panel) to the baryon asymmetry in the MSSM. Horizontal axis gives the bino soft mass parameter, M_1 . Vertical axis gives sine of the relative phase of M_1 , the supersymmetric μ parameter, and the soft Higgs mass parameter b . Green band indicates the values of these parameters needed to obtain the observed baryon asymmetry. Nearly horizontal lines give contours of constant EDMs. Figure originally published in Li *et al.* (2009).

Tureanu, 2013).

Parity, a unitary transformation described by $(t, \vec{r}) \rightarrow (t_P, \vec{r}_P) = (t, -\vec{r})$, reverses the handedness of the coordinate system, *i.e.* $\hat{x} \times \hat{y} = \hat{z}$ while $\hat{x}_P \times \hat{y}_P = -\hat{z}_P$, *etc.* Particles have intrinsic parity, that is the field describing a particle acquires a phase of ± 1 under the parity transformation. For fermions, particles and antiparticles have opposite intrinsic parity.

The time reversal transformation is described by $(t, \vec{r}) \rightarrow (t_T, \vec{r}_T) = (-t, \vec{r})$, but when this is applied to wave functions or fields not only is motion reversed (e.g. $\vec{p} \rightarrow \vec{p}$ and $\vec{J} \rightarrow -\vec{J}$) but the imaginary phase is reversed as well, *i.e.* time reversal includes complex conjugation. Moreover for scattering and decay processes, the initial and final state are reversed, which is a complication for interpreting any experiment such as detailed balance or decay correlations measurements, which are subject to final state corrections, for example due to the phase shift of a final state charged particle moving in a coulomb field (Callan and Treiman, 1967). Thus the *anti-unitary* time-reversal transformation involves motion reversal, complex conjugation and reversal of initial and final states. For an EDM, however, the initial and final states are the same, so there is no complication from final-state like effects and a definitive observation of an EDM is a direct signature of T-violation and, invoking the CPT theorem, of CP-violation.

Charge conjugation transforms particles into antiparticles, reversing charge without reversing the handedness or spin. It is interesting to note, therefore, that CPT

symmetry requires the EDM of a particle d and the EDM of its antiparticle \bar{d} given by eq. 1 be equal in magnitude and opposite in sign:

$$d\langle \vec{J} \rangle \xrightarrow{C} \bar{d}\langle \vec{J} \rangle \xrightarrow{P} +\bar{d}\langle \vec{J} \rangle \xrightarrow{T} \bar{d}\langle -\vec{J} \rangle = -\bar{d}\langle \vec{J} \rangle, \quad (12)$$

And similarly for the magnetic moments:

$$\mu\langle \vec{J} \rangle \xrightarrow{C} \bar{\mu}\langle \vec{J} \rangle \xrightarrow{P} +\bar{\mu}\langle \vec{J} \rangle \xrightarrow{T} \bar{\mu}\langle -\vec{J} \rangle = -\bar{\mu}\langle \vec{J} \rangle. \quad (13)$$

B. General Framework

As indicated by Fig. 1, EDMs in experimentally accessible systems arise from CP-violation at a fundamental level that is manifest at several energy or length scales. Fundamental theory incorporating Standard Model CKM and $\bar{\theta}$ and contributions together with Beyond-Standard-Model physics is contained in the Lagrangian

$$\mathcal{L}_{\text{CPV}} = \mathcal{L}_{\text{CKM}} + \mathcal{L}_{\bar{\theta}} + \mathcal{L}_{\text{BSM}}. \quad (14)$$

The general framework that connects this to experiment, Effective Field theory (EFT), absorbs higher-energy processes into a set of operators that contribute at a scale Λ resulting in a set of weak scale, non-renormalizable operators involving only Standard-Model fields. The corresponding amplitudes scale as $(v/\Lambda)^{d-4}$, where d is the operator's canonical dimension and $v = 246$ GeV is the Higgs vacuum expectation value.

\mathcal{O}_{fW}	$(\bar{F}\sigma^{\mu\nu}f_R)\tau^I\Phi W_{\mu\nu}^I$	fermion $SU(2)_L$ dipole
\mathcal{O}_{fB}	$(\bar{F}\sigma^{\mu\nu}f_R)\Phi B_{\mu\nu}$	fermion $U(1)_Y$ dipole
\mathcal{O}_{uG}	$(\bar{Q}\sigma^{\mu\nu}T^A u_R)\tilde{\varphi}G_{\mu\nu}^A$	u-quark Chromo EDM
\mathcal{O}_{dG}	$(\bar{Q}\sigma^{\mu\nu}T^A d_R)\varphi G_{\mu\nu}^A$	d-quark Chromo EDM
Q_{ledq}	$(\bar{L}^j e_R)(\bar{d}_R Q^j)$	CP-violating semi-leptonic
$Q_{lequ}^{(1)}$	$(\bar{L}^j e_R)\epsilon_{jk}(\bar{Q}^k u_R)$	
$Q_{lequ}^{(3)}$	$(\bar{L}^j \sigma_{\mu\nu} e_R)\epsilon_{jk}(\bar{Q}^k \sigma^{\mu\nu} u_R)$	
$\mathcal{O}_{\tilde{G}}$	$f^{ABC}\tilde{G}_{\mu\nu}^A G_{\nu\rho}^{B\rho} G_{\rho\mu}^C$	CP-violating 3 gluon
$Q_{quqd}^{(1)}$	$(\bar{Q}^j u_R)\epsilon_{jk}(\bar{Q}^k d_R)$	CP-violating four quark
$Q_{quqd}^{(8)}$	$(\bar{Q}^j T^A u_R)\epsilon_{jk}(\bar{Q}^k T^A d_R)$	
$Q_{\varphi ud}$	$i(\tilde{\varphi}^\dagger D_\mu \varphi)\bar{u}_R \gamma^\mu d_R$	quark-Higgs

TABLE II Dimension-six P-odd/T-odd operators that induce atomic, hadronic, and nuclear EDMs. Here φ is the SM Higgs doublet, $\tilde{\varphi} = i\tau_2 \varphi^*$, and $\Phi = \varphi$ ($\tilde{\varphi}$) for $I_3^f < 0$ ($I_3^f > 0$). The notation is adapted from ref (Engel *et al.*, 2013).

The $\bar{\theta}$ term in \mathcal{L}_{CPV} enters at EFT dimension $d = 4$, while CKM-generated fermions EDMs are dimension five, but electro-weak ($SU(2) \times U(1)$ gauge invariance requires the coupling to through the Higgs field making these effectively dimension six. Beyond-Standard-Model physics enters at dimension six and higher *i.e.*

$$\mathcal{L}_{BSM} \rightarrow \mathcal{L}_{CPV}^{\text{eff}} = \sum_{k,d} \alpha_k^{(d)} \left(\frac{1}{\Lambda}\right)^{d-4} \mathcal{O}_k^{(d)}, \quad (15)$$

where $\alpha_k^{(d)}$ is the Wilson coefficient for each operator $\mathcal{O}_k^{(d)}$, and where k denotes all operators for a given d that are invariant under the unbroken Standard-Model gauge symmetries ($SU(2)$ and $U(1)_B$), and the operators contain only Standard-Model fields; however when considering only first generation Standard-Model fermions and Standard-Model bosons, it is sufficient to consider only $d = 6$. At this order, the relevant set of operators, *i.e.* the “CP-violating sources”, listed in Table II, include the fermion $SU(2)_L$ and $U(1)_Y$ electroweak dipole operators and the $SU(3)_C$ chromo-electric-dipole operators; a set of four fermion semi-leptonic and non-leptonic operators; a CP-violating three-gluon operator; and a CP-violating fermion-Higgs operator. After electroweak symmetry-breaking, the dipole operators induce the elementary fermion EDMs and chromo-EDMs as well as analogous fermion couplings to the massive electroweak gauge bosons that are not directly relevant to the experimental observables discussed in this review. The fermion-Higgs operator induces a four-quark CP-violating operator whose transformation properties are distinct from the other four-quark operators listed in Table II.

The second term of the electromagnetic Lagrangian (Eq 3) describes the EDM interaction for an elementary fermion f , which couples left-handed to right-handed

fermions. Letting the Wilson coefficient $\alpha_{fV_k}^{(6)} = g_k C_{fV_k}$, where k refers to the gauge fields B, W, G .

$$\begin{aligned} \mathcal{L}_{\text{EDM}} &= -i \frac{d_f}{2} \bar{\Psi} \sigma^{\mu\nu} \gamma^5 F_{\mu\nu} \Psi \\ &= \frac{1}{\Lambda^2} (g_B C_{fB} \mathcal{O}_{fB} + 2I_3^f g_W C_{fW} \mathcal{O}_{fW}). \end{aligned} \quad (16)$$

Here the fermion EDM that couples to the EM field is

$$\begin{aligned} d_f &= -\frac{\sqrt{2}e}{v} \left(\frac{v}{\Lambda}\right)^2 (\text{Im } C_{fB} + 2I_3^f \text{Im } C_{fW}) \\ &= -(1.13 \times 10^{-13} \text{ e fm}) \left(\frac{v}{\Lambda}\right)^2 \text{Im } C_{f\gamma} \end{aligned} \quad (17)$$

where

$$\text{Im } C_{f\gamma} = \text{Im } C_{fB} + 2I_3^f \text{Im } C_{fW} \quad (18)$$

and I_3^f is the third component of weak isospin for fermion f . The chromo-EDM (CEDM) \tilde{d}_q corresponds to a CP-violating quark-gluon interaction that is conveniently written as

$$\mathcal{L}_{\text{CEDM}} = -i \sum_q \frac{g_3 \tilde{d}_q}{2} \bar{q} \sigma^{\mu\nu} T^A \gamma_5 q G_{\mu\nu}^A, \quad (19)$$

where T^A ($A = 1, \dots, 8$) are the generators of the QCD color group.

Due to electroweak gauge invariance, the coefficients of the operators that generate EDMs and chromo-EDMs ($Q_{q\tilde{G}}, Q_{f\tilde{W}}, Q_{f\tilde{B}}$) contain explicit factors of the Higgs field with Yukawa couplings $Y_f = \sqrt{2}m_f/v$, and we can write $\text{Im } C_{f\gamma} \equiv Y_f \delta_f$, *etc.* so that

$$d_f = -(1.13 \times 10^{-3} \text{ e fm}) \left(\frac{v}{\Lambda}\right)^2 Y_f \delta_f, \quad (20)$$

and

$$\tilde{d}_q = -(1.13 \times 10^{-3} \text{ fm}) \left(\frac{v}{\Lambda}\right)^2 Y_q \tilde{\delta}_q. \quad (21)$$

In general, we expect $\delta_q \sim \delta_\ell$, thus the up and down-quark EDMs would be comparable, but light quark EDM d_q would be roughly an order of magnitude larger than the electron EDM. As noted earlier, exceptions to this expectation can arise when the Higgs couples to heavy degrees of freedom in the loop graphs that generate quark EDMs and CEDMs.

Considering only first generation fermions, there are fifteen independent weak scale coefficients. Translating the electroweak dipole operators into the elementary fermion EDMs and neglecting couplings to massive gauge bosons leads to a set of twelve $d = 6$ CP-violating sources – in addition to the $\bar{\theta}$ parameter – that induce atomic, hadronic and nuclear EDMs.

C. Low-Energy Parameters

As indicated in Fig. 1, the Wilson coefficients are connected to the experimental observables at the hadronic scale, $\Lambda_{\text{had}} \sim 1$ GeV, through a set of low-energy parameters involving pions, and nucleons in place of quarks and gluons as well as photons and electrons. Considering first purely hadronic interactions, the starting point is a T-odd/P-odd (or TVPV) effective, non-relativistic Lagrangian containing pions and nucleons (Engel *et al.*, 2013):

$$\begin{aligned} \mathcal{L}_{\pi NN}^{\text{TVPV}} = & -2\bar{N} (\bar{d}_0 + \bar{d}_1 \tau_3) S_\mu N v_\nu F^{\mu\nu} \\ & + \bar{N} \left[\bar{g}_\pi^{(0)} \vec{\tau} \cdot \vec{\pi} + \bar{g}_\pi^{(1)} \pi^0 + \bar{g}_\pi^{(2)} (3\tau_3 \pi^0 - \vec{\tau} \cdot \vec{\pi}) \right] N, \end{aligned} \quad (22)$$

where S_μ is the spin of a nucleon N having velocity v_ν . A set of four-nucleon interactions that are currently being studied and are not considered in this discussion. The combinations $\bar{d}_0 + \bar{d}_1 \tau_3 = \bar{d}_0 \mp \bar{d}_1$ correspond to the short-range contributions to the neutron and proton EDMs. The quark EDMs generate contributions to the $\bar{d}_{0,1}$ while the quark CEDMs, the three-gluon operator, and the CP-violating four-quark operators (including the operator induced by $Q_{\varphi ud}$) will generate both the $\bar{d}_{0,1}$ and the $\bar{g}^{1,2,3}$. In practice, the sensitivity of the isotensor coupling $\bar{g}_\pi^{(2)}$ is significantly suppressed compared to that of $\bar{g}_\pi^{(0)}$ and $\bar{g}_\pi^{(1)}$. The T-odd/P-odd pion-nucleon interactions parameterized by the couplings $\bar{g}_\pi^{(i)}$, contribute to nucleon EDMs as well as to nucleon-nucleon interactions that generate the Schiff moment.

The semi-leptonic operators $\mathcal{O}_{\ell edq}$ and $\mathcal{O}_{\ell equ}^{(1,3)}$ induce an effective nucleon spin-independent (NSID) and nuclear spin-dependent electron-nucleon interactions, described by the scalar (S) and tensor (T) interactions:

$$\mathcal{L}_S = -\frac{G_F}{\sqrt{2}} \bar{e} i \gamma_5 e \bar{N} \left[C_S^{(0)} + C_S^{(1)} \tau_3 \right] N \quad (23)$$

$$\mathcal{L}_T = \frac{8G_F}{\sqrt{2}} \bar{e} \sigma_{\mu\nu} e v^\nu \bar{N} \left[C_T^{(0)} + C_T^{(1)} \tau_3 \right] S^\mu N + \dots, \quad (24)$$

where the Dirac matrices act on the electron wave function, G_F is the Fermi constant and N is a nucleon spinor, the sum over all nucleons is implied, and where the $+\dots$ indicate sub-leading contributions arising from the electron-scalar-nucleon-pseudoscalar interaction.

The coefficients $C_{S,T}^{(0,1)}$ can be expressed in terms of the underlying semileptonic operator coefficients and the

nucleon scalar and tensor form factors:

$$\begin{aligned} C_S^{(0)} &= -g_S^{(0)} \left(\frac{v}{\Lambda} \right)^2 \text{Im } C_{eq}^{(-)} \\ C_S^{(1)} &= g_S^{(1)} \left(\frac{v}{\Lambda} \right)^2 \text{Im } C_{eq}^{(+)} \\ C_T^{(0)} &= -g_T^{(0)} \left(\frac{v}{\Lambda} \right)^2 \text{Im } C_{\ell equ}^{(3)} \\ C_T^{(1)} &= -g_T^{(1)} \left(\frac{v}{\Lambda} \right)^2 \text{Im } C_{\ell equ}^{(3)} \end{aligned} \quad (25)$$

where

$$C_{eq}^{(\pm)} = C_{\ell edq} \pm C_{\ell equ}^{(1)} \quad . \quad (26)$$

and the isoscalar and isovector form factors $g_\Gamma^{(0,1)}$ are given by

$$\frac{1}{2} \langle N | [\bar{u} \Gamma u + \bar{d} \Gamma d] | N \rangle \equiv g_\Gamma^{(0)} \bar{\psi}_N \Gamma \psi_N, \quad (27)$$

$$\frac{1}{2} \langle N | [\bar{u} \Gamma u - \bar{d} \Gamma d] | N \rangle \equiv g_\Gamma^{(1)} \bar{\psi}_N \Gamma \tau_3 \psi_N, \quad (28)$$

where $\Gamma = 1$ and $\sigma_{\mu\nu}$, respectively (Engel *et al.*, 2013).

D. EDMs in the Standard Model

CP violation in the CKM matrix leads to non-vanishing coefficients of the $d = 6$ CP-violating sources at the multi-loop level. The primary theoretical interest has been the elementary fermion EDMs. The CKM lagrangian for mixing of left-handed down-type quarks to up-type quarks is

$$\mathcal{L}_{\text{CKM}} = -\frac{ig_2}{\sqrt{2}} \sum_{p,q} V^{pq} \bar{U}_L^p W^+ D_L^q + \text{h.c.} \quad (29)$$

Here g_2 is the weak coupling constant, W_μ^+ is the charged weak gauge field $U_L^p = u, c, t$ and $D_L^p = d, s, b$ are a generation- p left-handed up-type and down-type quark fields, V^{pq} denotes the element of the CKM matrix. The constraints from unitarity and quark-field rephasing for the three quark generations allow four free parameters: three magnitudes and a CP-violating phase. Writing

$$V_{\text{CKM}} = \begin{bmatrix} V^{ud} & V^{us} & V^{ub} \\ V^{cd} & V^{cs} & V^{cb} \\ V^{td} & V^{ts} & V^{tb} \end{bmatrix} \quad (30)$$

the CP violating effects are proportional to the Jarlskog invariant $\bar{\delta} = \text{Im}(V_{us} V_{cs}^* V_{cb} V_{ub}^*) \approx 5 \times 10^{-5}$. The value of $\bar{\delta}$ is derived from global analyses of a variety of CP-violating observables in the neutral kaon and B -meson systems (Charles *et al.*, 2015; Olive *et al.*, 2014). (Note that in the literature, $\bar{\delta}$ is sometimes expressed to leading order in the three CP-conserving mixing angles and CP-violating phase in the CKM matrix.)

The electron EDM arises at four-loop level and has been estimated by Ng and Ng (1996a) to be

$$d_e^{\text{CKM}} \approx \frac{eG_F}{\pi^2} \left(\frac{\alpha_{EM}}{2\pi} \right)^3 m_e \bar{\delta} \approx 10^{-38} \text{ e-cm}. \quad (31)$$

For the neutron, the contribution of the valence u - and d -quarks has been computed by Czarnecki and Krause (1997) to be

$$d_d \approx \frac{m_d m_c^2 \alpha_S G_F^2 \bar{\delta}}{108 \pi^5} \times f\left(\ln \frac{m_b^2}{m_c^2}, \ln \frac{m_W^2}{m_b^2}\right) \approx -0.7 \times 10^{-34} \text{ e-cm} \quad (32)$$

$$d_u \approx \frac{m_u m_s^2 \alpha_S G_F^2 \bar{\delta}}{216 \pi^5} \times f\left(\ln \frac{m_b^2}{m_s^2}, \ln \frac{m_c^2}{m_s^2}, \ln \frac{m_b^2}{m_c^2}, \ln \frac{m_W^2}{m_b^2}\right) \approx -0.15 \times 10^{-34} \text{ e-cm}, \quad (33)$$

where the f 's are functions of the natural logarithms of the mass ratios $\frac{m_b^2}{m_s^2}$, *etc.*. The valence-quark contribution to the neutron EDM is

$$d_n^{\text{CKM}} = \frac{4}{3} d_d - \frac{1}{3} d_u \approx -1.1 \times 10^{-34} \text{ e-cm}. \quad (34)$$

A significantly larger contribution to d_n (and d_p) arises from “long distance” meson-exchange contributions, for example that shown in Fig. 5, where the CP-violating $\Delta S = 1$ hadronic vertices are generated by the Penguin process of Fig. 2, while the CP-conserving $\Delta S = 1$ couplings arise from the tree-level-strangeness-changing charged current interaction (Eq. 29). A full compilation of diagrams and corresponding results for Standard-Model neutron and proton EDMs based on heavy baryon chiral perturbation theory is provided by Seng (2015):

$$|d_{n,p}| \approx (1 - 6) \times 10^{-32} \text{ e-cm} \quad (35)$$

where the range reflects the present uncertainty in various low energy constants that enter the heavy baryon effective Lagrangian and an estimate of the higher order terms neglected in the heavy baryon expansion.

For ^{199}Hg EDM, which has an unpaired neutron, the CKM contribution enters the Schiff moment through the P-odd/T-odd NN interaction mediated by kaon exchange (Donoghue *et al.*, 1987). Flambaum *et al.* (1986b) present an estimate of S using the one-body effective P-odd/T-odd potential for a valence nucleon

$$\hat{W} = \frac{G_F}{\sqrt{2}} \frac{\eta_a}{2m_N} \vec{\sigma}_a \cdot \vec{\nabla} \rho_A(\vec{r}) \quad , \quad (36)$$

where $\rho_A(\vec{r})$ is the nuclear density and

$$\eta_a = (N/A) \eta_{an} + (Z/A) \eta_{ap} \quad , \quad (37)$$

with $a = n$ or p . The resulting Standard-Model estimate for the Schiff moment and atomic EDM are

$$S(^{199}\text{Hg}) \approx -1.4 \times 10^{-8} \eta_{np} \text{ e fm}^3 \\ d_A(^{199}\text{Hg}) = -3.9 \times 10^{-27} \eta_{np} \text{ e cm} \quad , \quad (38)$$

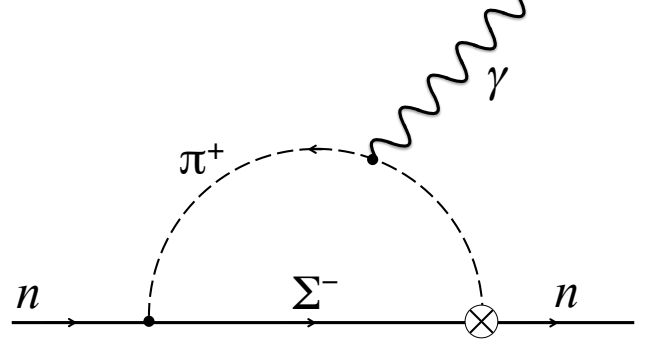


FIG. 5 Representative chiral loop contribution to the neutron EDM arising in from the Standard Model CKM CP-violation. The \otimes indicates a CP-violating $\Delta S = 1$ vertex such as that shown in Fig. 2, while the \bullet corresponds to a CP-conserving $\Delta S = 1$ interaction. Adapted from Pospelov and Ritz (2005).

where we have used $d_A(^{199}\text{Hg}) = (2.8 \times 10^{-4} \text{ fm}^{-2}) S$. In the Standard Model the η_{np} , *etc.* are proportional to $G_F \bar{\delta}$. Donoghue *et al.* (1987) corrected an earlier computation of η_{np} by properly taking into account the constraints from chiral symmetry resulting in $\eta_{np} \approx -10^{-9}$ and

$$|d_A(^{199}\text{Hg})^{\text{CKM}}| \lesssim 10^{-35} \text{ e cm} \quad . \quad (39)$$

The EDMs of unpaired nucleons also contribute to the Schiff moment and atom's EDM. For ^{199}Hg the unpaired neutron is dominant (Dmitriev and Sen'kov, 2003), and this contribution can be estimated using the Standard-Model estimate for d_n as

$$d_A(^{199}\text{Hg})^{\text{CKM}(n)} \approx 4 \times 10^{-4} d_n, \text{ i.e., giving} \quad (40)$$

$$|d_A(^{199}\text{Hg})^{\text{CKM}(n)}| \lesssim 2.4 \times 10^{-35} \text{ e-cm}, \quad (41)$$

which is comparable to the pion-nucleon contribution.

CP violation in the strong-interaction arises from the term in the QCD Lagrangian formed by gluon field $G_{\mu\nu}$ combined with its dual $\tilde{G}_{\mu\nu} = \epsilon_{\mu\nu\alpha\beta} G^{\alpha\beta} / 2$:

$$\mathcal{L}_{\bar{\theta}} = -\frac{\alpha_S}{16\pi^2} \bar{\theta} \text{Tr} \left(G^{\mu\nu} \tilde{G}_{\mu\nu} \right) \quad , \quad (42)$$

where α_S is the strong coupling constant.³ This will contribute to the neutron and proton EDM directly as well as inducing a nuclear Schiff moment

³ Following (Grzadkowski *et al.*, 2010), $\epsilon_{0123} = 1$. This sign convention is opposite that used by Pospelov and Ritz (2005) and elsewhere. Consequently, $\mathcal{L}_{\bar{\theta}}$ carries an overall -1 compared to what frequently appears in the literature.

through the T-odd/P-odd (isospin-zero) pion-nucleon coupling (Crewther *et al.*, 1979; Pospelov and Ritz, 1999; Shindler *et al.*, 2015). For the neutron, the results fall in the range

$$d_n^{\bar{\theta}} \approx -(0.9 - 1.2) \times 10^{-16} \bar{\theta} \text{ e-cm}. \quad (43)$$

Thus experimental constraints on EDMs in hadronic systems can be used to set an upper bound on $\bar{\theta}$. Assuming this interaction is the sole source of CP-violation, the upper bound on $\bar{\theta} \lesssim 10^{-10}$ from either d_n or $d_A(^{199}\text{Hg})$, neglecting uncertainties associated with the hadronic and nuclear many-body computations required in each case. As we discuss in Sec. V, allowing for multiple sources of CP violation can weaken this upper bound considerably, but the resulting constraint is nonetheless severe: $\bar{\theta} \lesssim 10^{-6}$. Either way, the tiny value allowed for a non-vanishing $\bar{\theta}$ parameter gives rise to the “strong CP problem.” This may be addressed by the axion solution, which postulates an axion field $a(x)$ that couples to gluons with the Lagrangian

$$\mathcal{L}_a = \frac{1}{2} \partial^\mu a \partial_\mu a - V(a) - \frac{a(x)}{f_a} \frac{\alpha_S}{8\pi} G^{\mu\nu} \tilde{G}_{\mu\nu}. \quad (44)$$

The first term is the kinetic energy, $V(a)$ is the axion potential and the third term is the axion-gluon coupling, and f_a the axion decay constant, which is analogous to the pion-decay constant. The ground-state is the minimum of the axion potential, which shifts the value of $\bar{\theta} \rightarrow \bar{\theta} + \frac{\langle a \rangle}{f_a}$ and could lead to cancelations that suppress $\bar{\theta}$.

Neutrino masses established by neutrino oscillations give rise to a 3×3 neutrino-mixing matrix with a single CP-violating phase analogous to the CKM phase. If neutrinos are Majorana particles, two-loop contributions d_e are possible (Ng and Ng, 1996a); however, this turns out to make a small contribution unless the neutrino masses are very specifically tuned (Archambault *et al.*, 2004)

E. Beyond-Standard-Model Physics

Observational and theoretical motivations for physics beyond the Standard Model include the need to explain dark matter, non-vanishing neutrino masses, the observed matter-antimatter asymmetry, and considerations of naturalness, which require a mechanism to solve the “hierarchy problem” associated with loop corrections to weak scale physics. In general, Beyond-Standard-Model scenarios that address these issues provide new mechanisms of CP-violation that also generate EDMs. Scenarios introduced to solve the hierarchy problem suggest the existence of new particles with masses $\lesssim 1$ TeV. Here, we discuss the EDM implications of a few representative Beyond-Standard-Model scenarios of current interest: supersymmetry (SUSY), left-right symmetric models, and extended Higgs sectors.

SUSY introduces symmetry between fermions and bosons, postulating an extra Higgs doublet and a set of new particles - “superpartners” of the Standard-Model particles called squarks, sleptons and gauginos. With this spectrum of new particles come new couplings and, most importantly, new CP-violating phases. Though there is currently no direct experimental evidence for SUSY or SUSY particles, the theory is well motivated by providing a mechanism for solving the hierarchy problem, unifying the gauge couplings, and by providing the new particles as potential dark matter candidates. In the minimal supersymmetric extension of the Standard Model (MSSM), there exist 40 additional CP-violating phases a subset of which can induce EDMs at the one-loop level. Representative one-loop contributions to the elementary fermion EDMs and quark chromo-EDMs are shown in Figs. 6 and 7, respectively. In each case, the external gauge boson can couple to any internal superpartner carrying the appropriate charge (electric charge for the fermion EDM or color for the chromoEDM).

It is useful to adopt several simplifying assumptions:

- i. there is a single mass scale M_{SUSY} common to all superpartners;
- ii. there is a common relative phase ϕ_μ between the supersymmetric Higgs/Higgsino mass parameter μ and the three SUSY-breaking gaugino masses, M_j ($j = 1, 2, 3$);
- iii. the SUSY-breaking trilinear interactions involving scalar fermions and the Higgs have a common phase, ϕ_A .

The resulting one-loop EDMs and CEDMs depend on M_{SUSY} and the two phases taking the form of Eqs. (20-21) with $\Lambda \rightarrow M_{\text{SUSY}}$, y_f the Yukawa coupling for the fermion of interest, are (Pospelov and Ritz, 2005; Ramsey-Musolf and Su, 2008)

$$\begin{aligned} \delta_e &= -\frac{1}{\sqrt{32\pi^2}} \left[\frac{g_1^2}{12} \sin \phi_A + \left(\frac{5g_2^2}{24} + \frac{g_1^2}{24} \right) \sin \phi_\mu \tan \beta \right] \\ \delta_q &= -\frac{1}{\sqrt{32\pi^2}} \left[\frac{\sqrt{2}g_3^2}{9} \left(\sin \phi_\mu R_q - \sin \phi_A \right) + \dots \right] \\ \tilde{\delta}_q &= -\frac{1}{\sqrt{32\pi^2}} \left[\frac{5g_3^2}{18\sqrt{2}} \left(\sin \phi_\mu R_q - \sin \phi_A \right) + \dots \right], \end{aligned} \quad (45)$$

where we have followed the opposite sign convention for the trilinear phase ϕ_A compared to Ref. (Ramsey-Musolf and Su, 2008). Here the $g_{1,2,3}$ are the gauge couplings, $\tan \beta = v_u/v_d$ is the ratio of the vacuum-expectation values of the two Higgs doublets, the “ $+\dots$ ” indicate contributions from loops involving electroweak gauginos, $R_d = \tan \beta$, and $R_u = \cot \beta$ for down quarks and up quarks, respectively. Turning to the 4-fermion and 3-gluon operators: SUSY scenarios with large $\tan \beta$ can generate

EDMs from CP- violating 4-fermion operators (Demir *et al.*, 2004; Lebedev and Pospelov, 2002). The Weinberg three-gluon operator receives contributions at the two-loop level from squark-gluino loops and at the three-loop level from diagrams involving the Higgs bosons. Naïvely $\sin \phi_\mu$ and $\sin \phi_A$ are expected to be $\mathcal{O}(1)$, and electroweak baryogenesis typically requires larger phases than at least a subset of the superpartner masses well below the TeV scale (Morrissey and Ramsey-Musolf, 2012).

An analysis of EDM results from d_e , d_n and $d_A(^{199}\text{Hf})$ by Pospelov and Ritz (2005) finds that $|\phi_{\mu,A}| \lesssim 10^{-1}$ for $M_{\text{SUSY}} = 500$ GeV, *i.e.* much less than naïve expectations, leading to the so-called SUSY-CP problem (Dimopoulos and Sutter, 1995). A more general analysis that does not rely on the assumption of phase universality yields somewhat relaxed constraints but does not eliminate the SUSY CP-problem (Li *et al.*, 2010). Ibrahim and Nath (1998) have pointed out that the individual phases need not be small themselves if there are sufficient cancellation contributions; however the dependence of d_e on ϕ_μ in Eq. 45 makes this “cancellation scenario” somewhat less plausible.

Giudice and Romanino (2004) and Kane *et al.* (2010) have considered a scenario in which the squark and slepton masses are considerably heavier than 1 TeV, while the electroweak gauge bosons and Higgsinos remain relatively light, leading to less constrained phases. Present LHC constraints on squark masses are consistent with this possibility, though the LHC slepton mass bounds are much weaker. In this regime of heavy squarks and sleptons, electroweak baryogenesis proceeds via CP-violating bino and/or wino interactions in the early universe, while EDMs of first generation fermions arise at two-loop order through the chargino-neutralino “Barr-Zee diagrams” shown in Fig. 8 (Barr and Zee, 1990). Applying this scenario to supersymmetric baryogenesis and relaxing the phase universality assumption leads to the results given in Fig. 4, showing that improvements in the sensitivities to d_e and d_n by one and two orders of magnitude, respectively, would probe the entire CP-violating parameter space for MSSM baryogenesis (Cirigliano *et al.*, 2010, 2006; Li *et al.*, 2009; Morrissey and Ramsey-Musolf, 2012). Note that supersymmetric electroweak baryogenesis requires not only sufficient CP-violation, but also a strong first order electroweak phase transition. LHC measurements of Higgs boson properties now render this possibility unlikely in the minimal model (Curtin *et al.*, 2012; Katz *et al.*, 2015); however, see Liebler *et al.* (2016). On the other hand, extensions of the MSSM with gauge singlet superfields presently allow for the needed first-order phase transition. In the context of these “next-to-minimal scenarios, the aforementioned CP-violating sources could give rise to the observed baryon asymmetry as indicated in Fig. 4.

The discovery of the 125 GeV Higgs boson has raised anew the possibility that it might be one of a num-

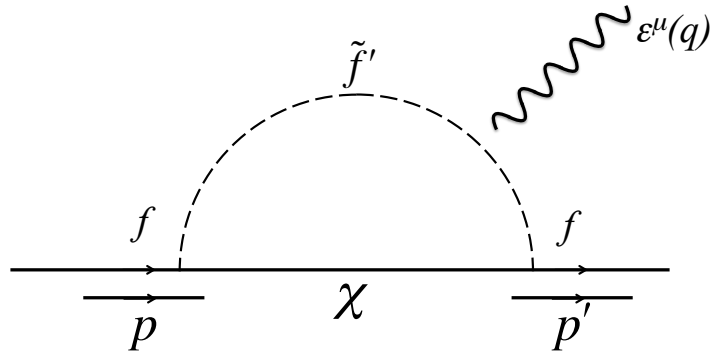


FIG. 6 One-loop fermion EDM generated by coupling to SUSY particles, f' and χ . Adapted from Ellis *et al.* (2008)).

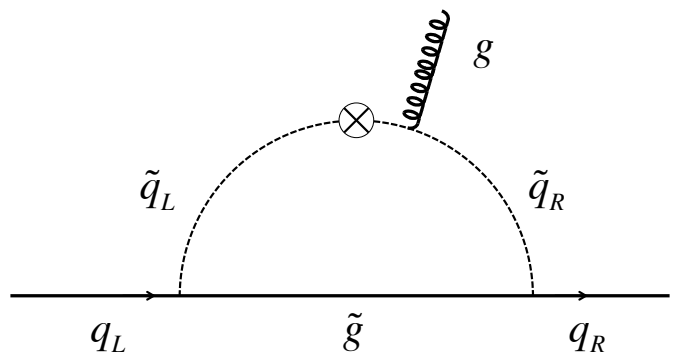


FIG. 7 An example of Beyond-Standard-Model couplings of the chromo-EDM to the gluon field g . The crossed-circle indicates interactions that mix the left- and right-handed squarks. Figure from Tardiff (2012).

ber of scalars, and a wide array of possibilities for the “larger” Higgs sector have been considered over the years. One scenario that has been studied extensively is the Two-Higgs-Doublet model, wherein the requirements of supersymmetry restrict the form of the scalar potential and the couplings of the two Higgs doublets to the Standard-Model fermions. In the more general context, the Two-Higgs-Doublet model allows for a variety of additional CP-violating phases, beyond those of the Standard Model, that can give rise to EDMs. The phases may arise in the scalar potential and/or the amplitudes for scalar-fermion interactions. The implications of new CP-violating phases in the Two-Higgs-Doublet model have been analyzed by Inoue *et al.* (2014), who consider a potential that manifests a softly-broken Z_2 symmetry in order to avoid constraints from the absence of flavor-changing neutral currents. (A Z_2 symmetry is a discrete symmetry under phase reversals of the relevant fields.) In the absence of CP-violation the scalar spectrum con-

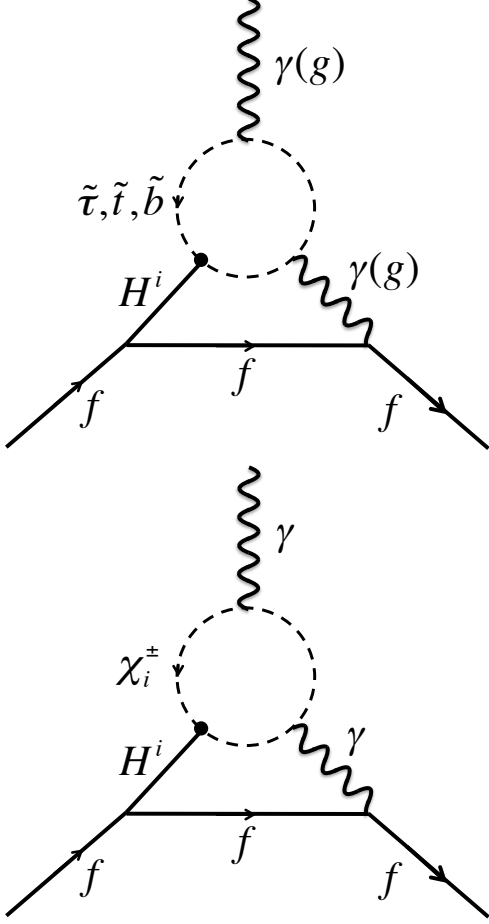


FIG. 8 Example two-loop Barr-Zee diagrams that give rise to a fermion EDM (coupling through γ) or CEDM (coupling through g). Here $\tilde{\tau}$ is the τ -slepton, \tilde{t} and \tilde{b} are squarks and χ is the chargino. Adapted from Barr and Zee (1990).

tains two charged scalars, H^\pm , and three neutral scalars: the CP-even H^0 and h^0 and the CP-odd A^0 . With the presence of CP-violating phases in the potential, the three neutral scalars mix to form the neutral mass eigenstates, h_i , one of which is identified with the 125 GeV Standard-Model-Higgs-like scalar. This CP-mixing translates into CP-violating phases in the couplings of the h^i to SM fermions, thereby inducing EDMs. In a variant of the Two-Higgs-Doublet model considered by Inoue *et al.* (2014), the requirements of electroweak symmetry-breaking imply that there exists only one CP-violating phase in the scalar sector α_b , which is responsible for both CP mixing among the scalars and the generation of EDMs. The latter arise from the Barr-Zee diagrams shown in Fig. 8.

Constraints on α_b as a function of $\tan\beta$ set by present and prospective EDM results are shown in Fig. 9 for the “type II” Two-Higgs-Doublet model (for an enumeration of the various variants of the Two-Higgs-Doublet

model, see, *e.g.*, Ref. (Barger *et al.*, 1990). The type II scenario has the same Yukawa structure as the MSSM.). The d_e limit from ThO is generally the most restrictive, except in the vicinity of $\tan\beta \sim 1$ and ~ 10 . Bian *et al.* (2015) have pointed out that the vanishing sensitivity to d_e near $\tan\beta \sim 1$ arises from a cancellation between the effects of the induced CP-violating couplings of the Higgs-like scalar to the electron and the corresponding couplings to the $hF^{\mu\nu}\tilde{F}_{\mu\nu}$ operator associated with the upper loop of the Barr-Zee diagrams. The neutron and ^{199}Hg EDMs are not susceptible to the same cancellation mechanism as the electron and provide additional constraints near $\tan\beta \sim 1$. The middle and far right panels show the sensitivity of prospective future EDM searches, including anticipated results of from ^{225}Ra (Bishof *et al.*, 2016). The reach of a ten times more sensitive d_e search would extend somewhat beyond the constraints from neutron and atomic searches, except in the cancellation regions. More optimistically, any non-zero result could indicate whether or not the observed EDM is consistent with CP violation in the Two-Higgs-Doublet model and help narrow the parameter space⁴.

Left Right Symmetric Models postulate the existence of a $SU(2)_L \times SU(2)_R \times U(1)_{B-L}$ symmetry, in which parity-violation of the Standard Model arises from spontaneous breakdown of the $SU(2)_R$ symmetry at a scale above the electroweak scale with $M_{W_R} \gg M_{W_L}$. This gives rise to a second CKM-like matrix for the right-handed charged-current couplings of W_L with a new CP-violating phase. Spontaneous symmetry breaking induces mixing between left-handed W_L and right-handed W_R gauge bosons, and the mass eigenstates become a mixture of W_L and W_R :

$$\begin{aligned} W_1^+ &= \cos\xi W_L^+ + \sin\xi e^{-i\alpha} W_R^+ \\ W_2^+ &= -\sin\xi e^{i\alpha} W_L^+ + \cos\xi W_R^+ \end{aligned} \quad (46)$$

where α is the CP-violating phase associated with the gauge boson mixing. This phase, along with the left- and right-handed CKM phases, can lead to one-loop quark EDMs arising from $W_{1,2}$ exchange. Retaining only the contribution from α and taking $|\sin\xi| \lesssim 10^{-3}$ as implied by tests of CKM matrix unitarity, the resulting short-range contribution to the neutron EDM is

$$|\bar{d}_n^{sr}| \lesssim (3 \times 10^{-14} \text{ e fm}) \left(1 - \frac{M_1^2}{M_2^2}\right) \cos\theta_L \cos\theta_R \sin\alpha, \quad (47)$$

where $\theta_{L,R}$ denote the left-handed and right-handed Cabibbo angles. The upper bound on the contribution to the neutron EDM is an order of magnitude less than

⁴ As indicated by Inoue *et al.* (2014), there exist considerable hadronic and nuclear theory uncertainties associated with the d_n and d_A sensitivities

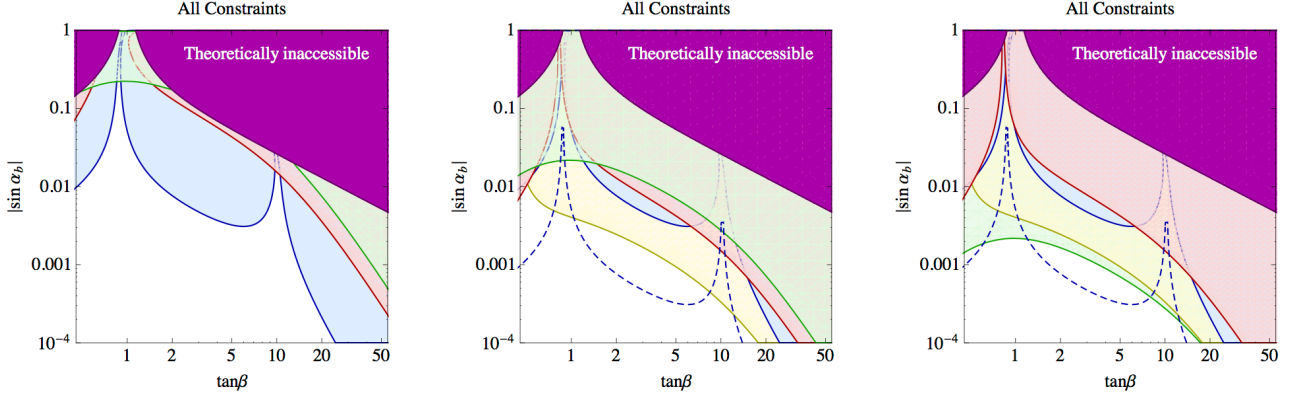


FIG. 9 (Color online) EDM results a for the Type II Two-Higgs-Doublet model. Horizontal axes show the ratio of up- and down-type Higgs vacuum expectation values. Vertical axes show the CP-violating phase that enters mixing of CP-even and CP-odd scalars. Purple regions are excluded by consistency with electroweak symmetry breaking. Left panel: current constraints from d_e (blue), d_n (green), and $d_A(^{199}\text{Hg})$. Middle panel: impact of improving present constraints by one order of magnitude, where blue dashed line indicates the prospective reach of d_e . The yellow region indicates the reach of a future $d_A(^{225}\text{Ra})$ with a sensitivity of $10^{-27} e \text{ cm}$. Right panel gives same future constraints but with d_n having two orders of magnitude better sensitivity than the present limit. Figure from Inoue *et al.* (2014).

the current limits on d_n , though the analysis should be revisited to include the quark CEDM contributions.

In addition, W_L - W_R mixing gives rise to a unique, four-quark CP-violating operator that, in turn, generates the T-odd/P-odd π - NN coupling $\bar{g}_\pi^{(1)}$ discussed in Sec. II.C.

$$\bar{g}_\pi^{(1)} \Big|_{\text{LRSM}} \approx 10^{-4} \left(1 - \frac{M_1^2}{M_2^2} \right) \sin \xi \cos \theta_L \cos \theta_R \sin \alpha \quad . \quad (48)$$

The resulting mercury atomic EDM is

$$|d_A(^{199}\text{Hg})| \lesssim (1.1 \times 10^{-11} e \text{ fm}) \quad (49) \\ \times \left(1 - \frac{M_1^2}{M_2^2} \right) \cos \theta_L \cos \theta_R \sin \alpha \quad ,$$

where we have again used an approximate upper bound $|\sin \xi| \lesssim 10^{-3}$ and have followed Ref. (Engel *et al.*, 2013) in taking a_1 at the midpoint of the range given in Table V. Given the significantly larger coefficient in Eq. (49) compared to that in Eq. (47), together with the stronger mercury atom EDM bound, we observe that the atomic EDM results currently place the most severe constraints on the CP violation associated with W_L - W_R mixing. There is, however, an important caveat: the contribution of $\bar{g}_\pi^{(1)}$ to the ^{199}Hg Schiff moment has significant nuclear theory uncertainties, and it is possible that the sensitivity is considerably weaker than indicated in Eq. 49. On the other hand, the nuclear many body computations for this contribution to the Schiff moments of other nuclei of experimental interest, such as ^{129}Xe , appear to be more reliable providing motivation for active pursuit of improved experiments on ^{129}Xe , $^{221/223}\text{Rn}$ and ^{225}Ra .

New phases could in principle also affect CP-violation in flavor-violating process such as meson mixing or in rare B -meson decays, and give complementary information on the model parameters (Altmannshofer *et al.*, 2008) that could push the new physics scale well beyond the 10 TeV. Even so, due to the generic flavor mixing, the electron and neutron EDMs are proportional to heavy-quark and lepton masses, and the experimental limits push to probe scales of 1000 TeV in some cases. An explicit example of such a case is given by the mini-split SUSY framework for which current EDM bounds already probe masses up to 100 TeV (Altmannshofer *et al.*, 2013; Arkani-Hamed *et al.*, 2012; Arvanitaki *et al.*, 2013; Hall and Nomura, 2012; Ibe and Yanagida, 2012; McKeen *et al.*, 2013).

Recent work has also considered the constraints that EDMs may place on CP-violating couplings of other SM particles, such as the Higgs boson or top quark. McKeen *et al.* (2012) computed constraints on the CPV Higgs-diphoton coupling, $hF_{\mu\nu}\tilde{F}^{\mu\nu}$, and showed that the corresponding relative impact of this operator on the rate for the decay $h \rightarrow \gamma\gamma$ at the 10^{-4} level, well below the expected sensitivity at the LHC or future Higgs factories. This constraint may be weaker in specific models, such as those containing vector-like fermions (see also Chao and Ramsey-Musolf (2014) for the connection with baryogenesis). Chien *et al.* (2016) investigated the constraints on dimension-six operators that couple the Higgs boson to quarks and gluons, and find that the impact of hadronic and nuclear physics uncertainties is pronounced. Cirigliano *et al.* (2016a,b) and Fuyuto and Ramsey-Musolf (2017) considered the constraints on the

top quark EDM from d_e and find that the bounds are three orders of magnitude stronger than obtained from other sources.

F. From theory to experiment

Experiments probe P-odd/T-odd observables in systems that combine a number of scales as illustrated in Fig. 1. For the neutron and proton, the fundamental CP-violating interactions discussed above arise from two sources: a short range contribution (denoted by $\bar{d}_{n,p}^{\text{sr}}$) and a long range contribution arising from the P-odd/T-odd pion-nucleon interactions. Storage ring experiments also have the potential to directly probe EDMs of light nuclei, namely, the deuteron ($^2\text{H}^+$) and helion ($^3\text{He}^{++}$) discussed in Sec. IV.G. The EDMs of these systems arise from the constituent nucleon EDMs as well as P-odd/T-odd nucleon-nucleon interactions arising from pion-exchange and from four-nucleon contact interactions. Paramagnetic atoms and molecules are most sensitive to the electron EDM and the nuclear-spin-independent electron-nucleus coupling. In diamagnetic atoms the dominant contributions are the nuclear-spin dependent electron-nucleus interaction and the Schiff moment, which also arises from long-range pion exchange and short range four-nucleon interactions. The following summarizes the contributions of these low-energy parameters to the experimentally accessible systems.

Nucleons:

Long-range contributions to the nucleon EDMs have been computed using chiral perturbation theory (see, *e.g.*, Fig. 10). The magnitude of $\bar{g}_\pi^{(2)}$ is expected to be suppressed by a factor of 100 or more relative to $\bar{g}_\pi^{(0)}$ and $\bar{g}_\pi^{(1)}$ based on chiral symmetry considerations, and is typically neglected in the computation of the nucleon EDMs (Chupp and Ramsey-Musolf, 2015). The result to next-to-next-to-leading order is (Seng *et al.*, 2014):

$$\begin{aligned} d_n &= \bar{d}_n^{\text{sr}} - \frac{eg_A}{8\pi^2 F_\pi} \left\{ \bar{g}_\pi^{(0)} \left[\ln \frac{m_\pi^2}{m_N^2} - \frac{\pi m_\pi}{2m_N} \right] \right. \\ &\quad \left. + \bar{g}_\pi^{(1)} \frac{(\kappa_1 - \kappa_0)}{4} \frac{m_\pi^2}{m_N^2} \ln \frac{m_\pi^2}{m_N^2} \right\} \\ d_p &= \bar{d}_p^{\text{sr}} + \frac{eg_A}{8\pi^2 F_\pi} \left\{ \bar{g}_\pi^{(0)} \left[\ln \frac{m_\pi^2}{m_N^2} - \frac{2\pi m_\pi}{m_N} \right] \right. \\ &\quad \left. - \frac{\bar{g}_\pi^{(1)}}{4} \left[\frac{2\pi m_\pi}{m_N} + \left(\frac{5}{2} + \kappa_0 + \kappa_1 \right) \frac{m_\pi^2}{m_N^2} \ln \frac{m_\pi^2}{m_N^2} \right] \right\}, \end{aligned} \quad (50)$$

where $g_A \approx 1.27$ is the nucleon isovector axial coupling, κ_0 and κ_1 are the isoscalar and isovector nucleon anomalous magnetic moments, respectively, and the low-energy coefficients \bar{d}_n^{sr} and \bar{d}_p^{sr} encode remaining short range contributions. Note that the $\bar{d}_{n,p}^{\text{sr}}$ are linear combinations of

the $\bar{d}_{0,1}$ given in Eq. (22). Computations of the $\bar{d}_{n,p}^{\text{sr}}$ and $\bar{g}_\pi^{(i)}$ in terms of the fundamental CP-violating interactions are reviewed by Engel *et al.* (2013) and updated in *e.g.*, Bhattacharya *et al.* (2015b); Bouchard *et al.* (2016); Seng and Ramsey-Musolf (2016); and Shindler *et al.* (2015). For example,

$$\bar{g}_\pi^0 \approx (0.005 - 0.04)\bar{\theta} + \dots, \quad (51)$$

where the range represents the present theoretical uncertainty and where the ellipses indicates BSM contributions (Engel *et al.*, 2013).

Light Nuclei:

Experimental approaches to storage-ring measurements of the EDMs of the deuteron (D or $^2\text{H}^+$) and helion (h or $^3\text{He}^{++}$) are discussed in Sec. IV.G. For the deuteron, the EDM has contributions from the nucleon moments as well as the pion-exchange contribution, leading to (Baisou *et al.*, 2015) [see also (Song *et al.*, 2013; Stetcu *et al.*, 2008; de Vries *et al.*, 2011; Wirzba *et al.*, 2017; Yamanaka, 2017)

$$d_D = d_n + d_p + [(0.0028 \pm 0.0003)g_\pi^0 + (0.18 \pm 0.02)\bar{g}_\pi^1] \text{e-fm}. \quad (52)$$

For the helion ($^3\text{He}^{++}$), the proton spins are nearly completely paired (Friar *et al.*, 1990) and the neutron EDM dominates the one-body contribution:

$$d_h = 0.9d_n - 0.05d_p + [(0.10 \pm 0.03)\bar{g}_\pi^0 + (0.14 \pm 0.03)\bar{g}_\pi^1] \text{e-fm}. \quad (53)$$

Note that the contributions from the four-nucleon contact interactions have not been included here.

Paramagnetic systems:

In paramagnetic systems with one or more unpaired electrons, there is a net electric field \vec{E}_{eff} at the electron's average position that is generally much greater than a laboratory electric field (many V/Å or GV/cm). Consequently the EDMs of paramagnetic atoms and P-odd/T-odd observables in polar molecules are dominated by the electron EDM and the nuclear-spin-independent electron-nucleon interaction, which couples to a scalar (S) component of the nucleus current. Taking the nuclear matrix element of the interactions given in Eq. (23) and assuming non-relativistic nucleons lead to the atomic Hamiltonian

$$\hat{H}_S = \frac{iG_F}{\sqrt{2}} \delta(\vec{r}) \left[(Z + N)C_S^{(0)} + (Z - N)C_S^{(1)} \right] \gamma_0 \gamma_5, \quad (54)$$

The resulting atomic EDM d_A is given by

$$d_A^{\text{para}} = \rho_A^e d_e - \kappa_S^{(0)} C_S, \quad (55)$$

where

$$C_S \equiv C_S^{(0)} + \left(\frac{Z - N}{Z + N} \right) C_S^{(1)}, \quad (56)$$

and where ρ_A^e and $\kappa_S^{(0)}$ are obtained from atomic and hadronic computations.

For polar molecules, the effective Hamiltonian is

$$\hat{H}_{\text{mol}} = [W_d d_e + W_S (Z + N) C_S] \vec{S} \cdot \hat{n} + \dots, \quad (57)$$

where \vec{S} and \hat{n} denote the unpaired electron spin and the unit vector along the intermolecular axis, respectively. The quantities $W_d \propto E_{eff}$ and W_S that give the sensitivities of the molecular energy to the electron EDM and electron-quark interaction are obtained from molecular structure calculations (Fleig and Nayak, 2013; Ginges and Flambaum, 2004; Meyer and Bohn, 2008; Mosyagin *et al.*, 1998; Petrov *et al.*, 2007; Skripnikov, 2017; Skripnikov *et al.*, 2013). The resulting ground state matrix element in the presence of an external electric field \vec{E}_{ext} is

$$\langle \text{g.s.} | \hat{H}_{\text{mol}} | \text{g.s.} \rangle = [W_d d_e + W_S (Z + N) C_S] \eta(E_{\text{ext}}), \quad (58)$$

with

$$\eta(E_{\text{ext}}) = \langle \text{g.s.} | \vec{S} \cdot \hat{n} | \text{g.s.} \rangle_{E_{\text{ext}}}. \quad (59)$$

This takes into account the orientation of the internuclear axis and the internal electric field with respect to the external field, *i.e.* the electric polarizability of the molecule. This leads to the observable, a P-odd/T-odd frequency shift measured in molecular experiments discussed in Sec. IV.C.

Diamagnetic atoms and molecules:

The EDMs of diamagnetic atoms of present experimental interest arise from the nuclear Schiff moment and the nuclear-spin-dependent electron-nucleon interaction, which couples to the tensor (T) nuclear current. The Schiff moment, accounting for both contributions from the EDM's of unpaired nucleons and the long-range pion-nucleon coupling, can be written

$$S = s_N d_N + \frac{m_N g_A}{F_\pi} \left[a_0 \bar{g}_\pi^{(0)} + a_1 \bar{g}_\pi^{(1)} + a_2 \bar{g}_\pi^{(2)} \right], \quad (60)$$

where contributions from the unpaired nucleon EDM's are given by $S(d_N) = s_n d_n + s_p d_p$ (Ban *et al.*, 2010; Dmitriev and Sen'kov, 2003; Dzuba *et al.*, 1985b), $g_A \approx 1.27$ is the nucleon axial-vector coupling and $F_\pi = 92.2$ MeV is pion decay constant. For the nuclear Schiff moment, values of $a_{0,1,2}$ from Eq. 60 for ^{199}Hg , ^{129}Xe , ^{225}Ra and TlF are presented in Table V. The values of the $a_{0,1,2}$ depend on the details of the assumed nucleon-nucleon interaction; however note that there is no single consistent approach for all nuclei of interest. As discussed above, each isospin component may be particularly sensitive to a subset of the possible CP-violating interactions. For example, the QCD parameter $\bar{\theta}$ contributes most strongly to $\bar{g}_\pi^{(0)}$, while the effect of W_L - W_R mixing in the Left-Right Symmetric Model shows up most strongly in $\bar{g}_\pi^{(1)}$.

The nucleon EDM long-range and short-range contributions to the Schiff moment can be separated using Eq. 50 to write

$$S = s_N \bar{d}_N^{sr} + \left[\frac{m_N g_A}{F_\pi} a_0 + s_N \alpha_{n\bar{g}_\pi^{(0)}} \right] \bar{g}_\pi^{(0)} + \left[\frac{m_N g_A}{F_\pi} a_1 + s_N \alpha_{n\bar{g}_\pi^{(1)}} \right] \bar{g}_\pi^{(1)}, \quad (61)$$

where the coefficients $\alpha_{N\bar{g}_\pi^{(0,1)}}$, given in Table IV, are the factors multiplying $\bar{g}_\pi^{(0)}$ and $\bar{g}_\pi^{(1)}$ in Eq. 50, and the smaller $\bar{g}_\pi^{(2)}$ pion-nucleon contribution to S has been dropped.

Contributions from the electron-nucleus interaction are revealed in the Hamiltonian resulting from Eq. (24):

$$\hat{H}_T = \frac{2iG_F}{\sqrt{2}} \delta(\vec{r}) \left[C_T^{(0)} + C_T^{(1)} \tau_3 \right] \vec{\sigma}_N \cdot \vec{\gamma}, \quad (62)$$

where the sum over all nucleons is again implicit; τ_3 is the nucleon isospin Pauli matrix, $\vec{\sigma}_N$ is the nucleon spin Pauli matrix, and $\vec{\gamma}$ acts on the electron wave function. Including the effect of \hat{H}_T , the individual nucleon EDMs d_N , and the nuclear Schiff moment S (Eq. 7), one has

$$d_A^{dia} = \kappa_S S - \left[k_{C_T}^{(0)} C_T^{(0)} + k_{C_T}^{(1)} C_T^{(1)} \right], \quad (63)$$

where κ_S and $k_{C_T}^{(0,1)}$ give the sensitivities of the d_A^{dia} to the Schiff moment and the isoscalar and isovector electron-quark tensor interactions and are provided in Tables IV and V. As indicated in Eq. 25, the isoscalar and isovector tensor couplings depend on the same Wilson coefficient $\text{Im } C_{\ell equ}^{(3)}$, so their values differ only due to the different nucleon form factors $g_T^{(0,1)}$. Until recently, there has been limited information on the nucleon tensor form factors $g_T^{(0,1)}$. Computations using lattice QCD have now obtained $g_T^{(1)} = 0.49(03)$ (Bhattacharya *et al.*, 2016) and $g_T^{(0)} = 0.27(03)$ (Bhattacharya *et al.*, 2015a)⁵. For the diamagnetic atoms of experimental interest (Hg, Xe, Ra) the nuclear matrix elements are dominated by the contribution from a single, unpaired neutron while for TlF, to a good approximation the proton is unpaired. We therefore replace the last term in brackets in Eq. (63) with $k_T^n C_T^n$ or $k_T^p C_T^p$, for an unpaired neutron or proton, respectively, where

$$C_T^n = - \left[g_T^{(0)} - g_T^{(1)} \right] \left(\frac{v}{\Lambda} \right)^2 \text{Im } C_{\ell equ}^{(3)} \approx -0.76 C_T^{(0)} \\ C_T^p = - \left[g_T^{(0)} + g_T^{(1)} \right] \left(\frac{v}{\Lambda} \right)^2 \text{Im } C_{\ell equ}^{(3)} \approx +2.45 C_T^{(0)}. \quad (64)$$

⁵ Note that the numerical values of the tensor couplings given in these references are two times larger than quoted here, owing to differences in normalization conventions.

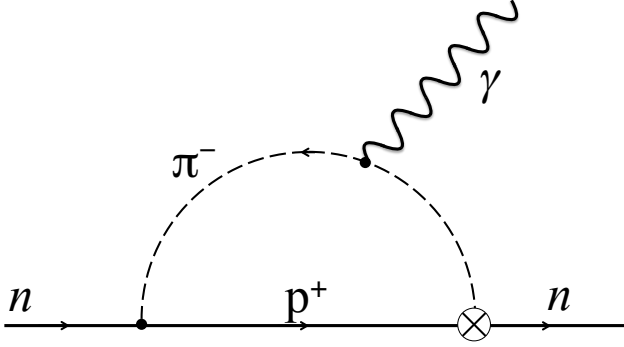


FIG. 10 Representative long-range, pion-exchange contributions to the neutron EDM. The cross represents the CP-violating vertex, while the closed circle is the CP-conserving vertex. Adapted from Pospelov and Ritz (2000).

Table IV provides the coefficients for the dependence of d_A^{dia} on $\bar{g}_\pi^{(0)}$, $\bar{g}_\pi^{(1)}$, and \bar{d}_n^{sr} .

In summary, contributions to the EDM's systems accessible to experiment can be expressed in terms of the following set of low-energy parameters:

1. The lepton EDMs; the electron EDM d_e contributes in first order to the EDMs of paramagnetic atoms and molecules.
2. Two isospin components of the nuclear-spin-independent eN coupling $C_S^{0,1}$; since most of the heavy-atom systems have a roughly equal ratio of neutrons to protons this can be reduced to a single average $\bar{C}_S = C_S^0 - \frac{(N-Z)}{A} C_S^1 \approx C_S^0$.
3. The nuclear-spin-dependent eN coupling labeled by $C_T^{(0,1)}$, most important in diamagnetic atoms and molecules.
4. The short-range contribution to the nucleon EDMs $\bar{d}_{n,p}^{sr}$.
5. The pion-nucleon couplings labeled $\bar{g}_\pi^{(i)}$ that contribute to the nucleon and nuclear EDMs and to the Schiff moments of nuclei. Given that the sensitivity of $\bar{g}_\pi^{(2)}$ to the CP-violating interactions is highly suppressed, we will omit it in the following.

We therefore separate paramagnetic atoms and molecules from diamagnetic systems and also separate nucleon and fundamental-fermion EDMs, as follows:

Paramagnetic atoms

$$d_{para} = \eta_{d_e} d_e + k_{C_S} \bar{C}_S \quad (65)$$

Polar molecules

$$\Delta\omega_{para}^{PT} = \frac{-d_e E_{eff}}{\hbar} + k_{C_S}^\omega \bar{C}_S \quad (66)$$

Diamagnetic atoms

$$d_{dia} = \kappa_S S(\bar{g}_\pi^{0,1}, d_N) + k_{C_T^{(0)}} C_T^{(0)} + \dots \quad (67)$$

Nucleons

$$d_{n,p} = d_{n,p}^{lr}(\bar{g}_\pi^{0,1}) + \bar{d}_{n,p}^{sr} \quad (68)$$

Charged leptons

$$d_e, d_\mu, (d_\tau) \quad (69)$$

The coefficients η , k and κ are presented in Tables III, IV and V.

Note that the other contributions enter the atomic and molecular systems at higher order, but are less important; however due to the exquisite sensitivity of the ^{199}Hg EDM measurement, the higher order contribution of the electron EDM d_e does have an impact. Additionally, experiments in paramagnetic solid-state systems with quasi-free electrons are directly sensitive to d_e .

III. EXPERIMENTAL TECHNIQUES

The crux of any EDM measurement is to project the effect of the coupling to an electric field in the background of much larger magnetic effects using the unique P-odd/T-odd signature. Most EDM experiments using beams or cells are magnetic resonance approaches that measure the energy or, more commonly, frequency given in Eq. 5 of transitions between magnetic sub levels in the presence of a well-controlled magnetic field B , and electric field E aligned either parallel or anti-parallel to B . Storage-ring experiments with charged particles measure the result of the additional torque on the spin due to $\vec{d} \times \vec{E}$, where \vec{E} may arise in part from the motional field $\vec{v} \times \vec{B}$. In solid-state electron-EDM experiments, the observable is proportional to $\vec{B} \cdot \vec{E}$, where only one field is applied and the other measured - for example a strong electric field \vec{E}_{applied} would polarize electron spins in the material giving rise to an observable magnetic field $\vec{B}_{\text{observed}}$.

Because every system of interest has a magnetic moment, the magnetic environment is crucial and the magnetic field must be characterized in space and time. Magnetic shielding, magnetic sensors external to the EDM volume and comagnetometers that monitor the magnetic field within the EDM volume during the EDM measurement are all essential elements of past and future experiments. Comagnetometer species are chosen because they are less sensitive to P-odd/T-odd effects than the key species. For example the comagnetometer for the neutron-EDM experiment of Baker *et al.* (2006) was ^{199}Hg , and for Cs and Tl beam experiments Na was used (Regan *et al.*, 2002a; Weisskopf, 1968). The measurement of the ^{129}Xe EDM utilized ^3He as the comagnetometer species.

System	$\alpha_{d_e} = \eta_e$	$\alpha_{C_S} = W_S$	$\alpha_{C_S}/\alpha_{d_e}$
Cs	123 (100-138)	7.1×10^{-19} e-cm (7.0-7.2)	5.8×10^{-21} (e-cm) (0.6-0.7) $\times 10^{-20}$
Tl	-573 (-562-716)	-7×10^{-18} e-cm (-5-9)	1.2×10^{-20} (e-cm) (1.1-1.2) $\times 10^{-20}$
YbF	$-3.5 \times 10^{25} \frac{\text{rad/s}}{e\text{-cm}}$ (-2.9-3.8)	-2.9×10^5 rad/s (-4.6-6.8)	8.6×10^{-21} (e-cm) (8.0-9.0) $\times 10^{-21}$
ThO	$-1.6 \times 10^{26} \frac{\text{rad/s}}{e\text{-cm}}$ (-1.3-1.6)	-2.1×10^6 rad/s (-1.4-2.1)	1.3×10^{-20} (e-cm) (1.2-1.3) $\times 10^{-20}$
HfF ⁺	$3.5 \times 10^{25} \frac{\text{rad/s}}{e\text{-cm}}$ (-3.4-3.6)	2.0×10^6 rad/s (1.9-2.1)	5.7×10^{-20} (e-cm) (5.3-6.2)

TABLE III Sensitivity to d_e and C_S and the ratio $\alpha_{C_S}/\alpha_{d_e}$ for observables in paramagnetic systems based on atomic theory calculations. Ranges (bottom entry) for coefficients α_{ij} representing the contribution of each of the T-odd/P-odd parameters to the observed EDM of each system. See Ginges and Flambaum (2004) and Engel *et al.* (2013) for Cs and Tl. For YbF, theory results are compiled in Dzuba *et al.* (2011), for ThO results are from Meyer and Bohn (2008), Dzuba *et al.* (2011), and Skripnikov *et al.* (2013), and for HfF⁺ from Petrov *et al.* (2007), Fleig and Nayak (2013) and Skripnikov (2017). (Note that for YbF and ThO, $\alpha_{d_e} = eE_{eff}/\hbar = \pi W_d$, with W_d given in (Engel *et al.*, 2013); for HfF⁺, $\alpha_{d_e} = eE_{eff}/\hbar$ (Cairncross *et al.*, 2017) and $\alpha_{C_S} = W_S = W_{T,P} \frac{Z+N}{Z}$ with $W_{T,P}$ given by (Skripnikov, 2017).)

System	$\partial d^{exp}/\partial d_e$	$\partial d^{exp}/\partial C_S$	$\partial d^{exp}/\partial C_T^{(0)}$	$\partial d^{exp}/\partial g_\pi^0$	$\partial d^{exp}/\partial g_\pi^1$	$\partial d^{exp}/\partial \bar{d}_n^{sr}$
neutron				1.5×10^{-14}	1.4×10^{-16}	1
¹²⁹ Xe	-0.0008 -4.4-(-5.6)	-4.4×10^{-23} -4.4-(-5.6)	-6.1×10^{-21} -6.1-(-9.1)	-0.4×10^{-19} -23.4-(1.8)	-2.2×10^{-19} -19-(-1.1)	1.7×10^{-5} 1.7-2.4
¹⁹⁹ Hg	-0.014 -0.014-0.012	-5.9×10^{-22}	3.0×10^{-20} 3.0-9.0	-11.8×10^{-18} -38-(-9.9)	0 (-4.9-1.6) $\times 10^{-17}$	-5.3×10^{-4} -7.7-(-5.2)
²²⁵ Ra			5.3×10^{-20}	1.7×10^{-15} 6.9-0.9	-6.9×10^{-15} -27.5-(-3.8)	$(-1.6-0) \times 10^{-3}$
TlF	81	2.9×10^{-18}	2.7×10^{-16}	1.9×10^{-14} 0.5-2	-1.6×10^{-13}	0.46 -0.5-0.5

TABLE IV Coefficients for P-odd/T-odd parameter contributions to EDMs for diamagnetic systems and the neutron in units of e-cm except for $\partial d^{exp}/\partial \bar{d}_n^{sr}$, which is dimensionless. The second line for each entry is the reasonable range for each coefficient. The $\partial d^{exp}/\partial d_e$ and $\partial d^{exp}/\partial C_S$ are from (Ginges and Flambaum, 2004) and are based on (Martensson-Pendrill, 1985) and (Martensson-Pendrill and Oster, 1987) for ¹²⁹Xe and ¹⁹⁹Hg. The $\partial d^{exp}/\partial d_e$ and $\partial d^{exp}/\partial C_S$ and for TlF are compiled in (Cho, 1991). The $\partial d^{exp}/\partial C_T^{(0)}$ are adjusted for the unpaired neutron in ¹²⁹Xe, ¹⁹⁹Hg and ²²⁵Ra using k_T from (Ginges and Flambaum, 2004) and for ²²⁵Ra from (Dzuba *et al.*, 2009). The $\bar{g}_\pi^{(0)}$, $\bar{g}_\pi^{(1)}$ and \bar{d}_n^{sr} coefficients for atoms and molecules are based on data provided in Table V; the range for ²²⁵Ra corresponds to $0 \leq s_n \leq 2$ fm². For TlF, the unpaired neutron is replaced by an unpaired proton and the “best value” assumes $\bar{d}_p^{sr} = -\bar{d}_n^{sr}$, *i.e.* mostly isovector in analogy to the anomalous magnetic moment, while the range is defined by $|\bar{d}_p^{sr}| \leq |\bar{d}_n^{sr}|$.

System	$\kappa_S = \frac{d}{S}$ (cm/fm ³)	$a_0 = \frac{S}{13.5\bar{g}_\pi^0}$ (e-fm ³)	$a_1 = \frac{S}{13.5\bar{g}_\pi^1}$ (e-fm ³)	$a_2 = \frac{S}{13.5\bar{g}_\pi^2}$ (e-fm ³)	s_N (fm ²)
¹²⁹ Xe	0.27×10^{-17} (0.27-0.38)	-0.008(-0.005-(-0.05))	-0.006(-0.003-(-0.05))	-0.009(-0.005-(-0.1))	0.63
¹⁹⁹ Hg	-2.8×10^{-17} (-4.0-(-2.8))	0.01 (0.005-0.05)	± 0.02 (-0.03-0.09)	0.02(0.01-0.06)	1.895 ± 0.035
²²⁵ Ra	-8.5×10^{-17} (-8.5-(-7.0))	-1.5 (-6-(-1))	+6.0 (4-24)	-4.0 (-15-(-3))	
TlF	-7.4×10^{-14}	-0.0124	0.1612	-0.0248	0.62

TABLE V Best values and ranges (in parenthesis) for atomic EDM sensitivity to the Schiff-moment and dependence of the Schiff moments on $\bar{g}_\pi^{(0)}$ and $\bar{g}_\pi^{(1)}$; κ_S and s_N . References: TlF: (Coveney and Sandars, 1983a); Hg: (Dzuba *et al.*, 2002; Flambaum *et al.*, 1986a); Xe: (Dzuba *et al.*, 1985a, 2002); Ra: (Dzuba *et al.*, 2002; Spevak *et al.*, 1997a). Values for a_0 , a_1 and a_2 are compiled in (Engel *et al.*, 2013) The value of s_n is from (Dzuba *et al.*, 1985b) for ¹²⁹Xe and from (Dmitriev and Sen'kov, 2003) for ¹⁹⁹Hg; there is no available calculation of s_n for ²²⁵Ra. The value for s_p for TlF is derived from (Cho, 1991).

EDM measurements in many systems require determining frequency differences with precision of nHz (10^{-9} Hz) or less by some means with measurement times much less than 10^9 seconds. Another interesting feature for stored atoms and neutrons is the need to correct for the Earth's rotation as well as the accumulated quantum phase or Berry's phase that arises due to the combination of motional magnetic field $(\vec{v} \times \vec{E})/c^2$ with magnetic-field gradients.

A. Magnetic shielding

A critical component of EDM experiments is the magnetic shielding, which mitigates electromagnetic distortions in time and space. Neutron and proton EDM experiments in particular require large volumes with stringent magnetic shielding requirements. For example, improving the current limit on the neutron EDM by two orders of magnitude requires magnetic-field gradients less than 0.3 nT/m (see sec. IV.A). The temporal stability of the magnetic gradient must be better than $100 \text{ fTm}^{-1}\text{s}^{-1}$ over the 100-300 s neutron-storage time. This requires a strong damping factor (also commonly called "shielding factor") of external perturbations at extremely low frequencies, *i.e.* between 1-100 mHz. It is also crucial to reverse the magnetic field orientation in the lab, which requires magnetic shields that can tolerate large changes of the field *inside* the shield. Whereas small scale high-quality cryogenic magnetically shielded environments have already been achieved, *e.g.* (Cabrera, 1988; Kornack *et al.*, 2007), shielding for large-scale next-generation experiments presents a different scale of challenge, addressed by recent advances in room-temperature, active and passive magnetic shielding techniques (Altarev *et al.*, 2015a, 2014; Sun *et al.*, 2016).

Passive magnetic shielding is based on surrounding the volume of interest with a high-magnetic-permeability material generally called mu-metal or permalloy. Permalloy is applied in thicknesses of order 1-4 mm rolled into welded cylinders or cones (Yashchuk *et al.*, 1999) or assembled as sheets. A passive shield is best characterized by the reduction in the amplitude of magnetic field variations at a *i.e.* the frequency-dependent damping factor or shielding factor $SF(f)$. A second crucial characteristic is the residual field and gradient inside the shield, which is affected by a procedure called degaussing or equilibration.

It is useful to provide analytic approximations for static fields as guidelines for cylindrical shields composed of permalloy cylinders with permeability μ , thickness t and radius R (Sumner *et al.*, 1987), with the caveat that actual results for damping factors at low frequencies, in particular for multi-layer shields, may differ significantly. The transverse damping factor for a single shield is ap-

proximately given by

$$SF^T \approx 1 + \mu t / 2R. \quad (70)$$

The transverse shielding factor for multiple layers is approximately a product of damping factors; for n layers the transverse shielding factor is approximately

$$SF^T \approx SF_n^T \prod_{i=1}^{n-1} SF_i^T (1 - (\frac{R_i}{R_{i+1}})^2). \quad (71)$$

The air-gaps between layers can be optimized for a given material, thickness and number of layers. Axial shielding is generally less effective and depends on the ratio of the length of the cylinder to the radius $a = L/R$ and the distribution of magnetic flux over the cylinder walls and ends, which is characterized measured quantities α and β ($\alpha \leq 1$ and $1 \leq \beta \leq 2$):

$$SF^A \approx 1 + (\frac{2\kappa(a)}{1 + a + \alpha a^2/3}) SF^T, \quad (72)$$

where

$$\begin{aligned} \kappa(A) = & (1 + \frac{1}{4a^3})\beta - \frac{1}{a} \\ & + 2\alpha \{ \ln(a + \sqrt{1 + a^2}) - 2(\sqrt{1 + \frac{1}{a^2}} - \frac{1}{a}) \}. \end{aligned} \quad (73)$$

In general, effective design of shields is aided by finite-element approaches (*e.g.* Opera, Comsol, *etc.*).

The state of the art in 2017, set up at the TU München at the FRM-II reactor, is a magnetic shielded box with inside dimensions $1.54 \text{ m} \times 1.54 \text{ m} \times 2.2 \text{ m}$ shown in fig. 11 (Altarev *et al.*, 2014). The following advances in the technique of magnetic shielding were implemented for the TU München shield (Altarev *et al.*, 2014):

- Increased thickness of the metal sheets, as well as width and length of individual sheets, which are connected at many places to form one closed shell of shielding material with 5 cm overlap at the edges;
- Fewer material joints, effected with large rectangular sheets (sizes of $3000 \text{ mm} \times 750 \text{ mm}$ with 1-1.6 mm thickness are typical maximum commercially available dimensions), which are mounted in pairs with perpendicular orientation;
- A gap of 8 cm between shield layers does not degrade performance, in contrast to previous design criteria that suggested a significantly larger spacing of the layers helps obtain good shielding performance;
- Balancing the tradeoff of a small residual field and large shielding factor has led to a thinner (2mm) inner shield layer of the permalloy Krupp Magnifer⁶.

⁶ Krupp Magnifer is a commercial product from VDM Metals GmbH, Plettenberger Strasse 2, 58791 Werdohl, Germany

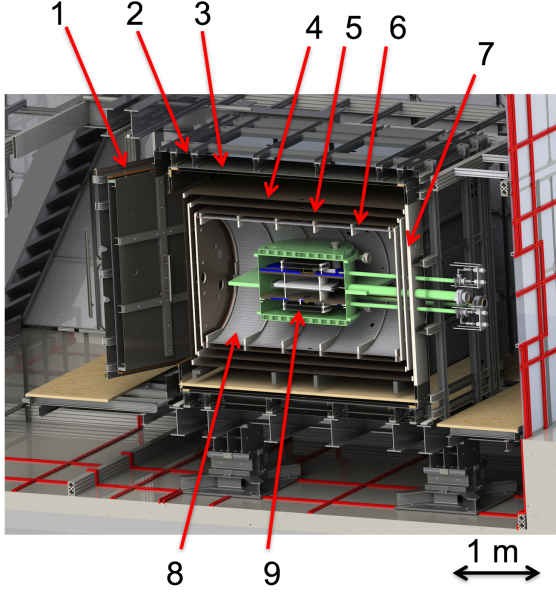


FIG. 11 (Color online) Cut through the magnetic shield of the TU München EDM experiment. The outer magnetically shielded room (MSR) is described in detail in ref. (Altarev *et al.*, 2015a). Item (1) is the large door of the MSR, (2) the outer magnetic shield made from 2 mm Magnifer, (3) 2 mm Magnifer shell together with the 8 mm aluminum shell for radio-frequency shielding. Inside this shell, a rail system is mounted to bring in the Insert with 3 shells and the experiment. Item (4) is the outer 2 mm Magnifer shell of the insert, (5) the 4 mm middle shell and (6) the 2 mm inner shell of the insert; item (7) is the insert door. Item (8), inside the insert is the NMR magnet described in Fig 16, and (9) the chamber containing the EDM experiment.

- The layers are arranged with outer layers of 2 mm Krupp Magnifer, 8 mm of aluminum, and 2 mm of Magnifer and three inner layers of, respectively 2 mm, 4 mm and 2 mm of Krupp Magnifer (see Fig. 11).

The TU-München shielded box has a residual field of a few-hundred pT, and a gradient of $|\nabla B| = 100$ pT/m. An inner shield constructed of a single-layer permalloy cylinder with 1.4 m diameter and 2.1 m length mounted inside this box had an internal magnetic field of $|B| < 100$ pT over a volume of over $(0.5 \text{ m})^3$. An alternative inner shield consisted of a single-layer 1.8 m-cubic box with residual field $|B| < 100$ pT and gradient $|\nabla B| < 25$ pT/m over a $(0.8 \text{ m})^3$ volume. The damping factor inside the box for low-amplitude variations of the external field ($\sim 1 \mu\text{T}$) exceeds 10^6 at the 0.001 Hz low-frequency limit of the measurements, reducing effects caused by typical external distortions (crane operation, people with tools, doors, cars and other machinery within 10's of meters distance from the shield and major transportation such

as subway trains or electric buses 100's of meters away) to below 1 pT. Typically ambient magnetic field drifts are up to 1000-times smaller at night, and drifts of ~ 10 fT and gradient < 100 fT/m have been recorded at all positions inside the shields.

A comparison of three leading magnetic-shield installations including the TU-München shield is presented in Table VI. The Berlin-Magetically-Shielded Room (BMSR-II) is a large scale/walk-in user facility with small residual fields (Bork *et al.*, 2002), and the Boston Medical-Center shield (Boston), used for biomagnetism research is composed of three permalloy layers and three aluminum layers resulting in a large damping factor at the relatively high frequency of 1 Hz (Cohen *et al.*, 2002). Note that direct comparison of shields is difficult due to the unknown and different measurement conditions.

Magnetic equilibration is a procedure based on commonly known degaussing techniques developed to achieve extremely small residual fields and gradients (Altarev *et al.*, 2015a,b; Sun *et al.*, 2016; Thiel *et al.*, 2007; Voigt *et al.*, 2013). Magnetic equilibration based on the developments of Voigt *et al.* (2013) used coils wound around the edges of each shell of a cuboid shield to generate strong magnetic flux with a sinusoidal AC current of several Hz frequency and linearly or exponentially decreasing amplitude. The result of the procedure is a superposition of damped fields from outside the shield, residual magnetization of the shield material, distortions caused by holes and other imperfections, and applied internal fields. It is found that holes up to 130 mm and overlaps of the shielding layers do not notably change the damping factor or the residual fields at the center of the shields, whereas overlaps do not cause distortions close to the walls. (Altarev *et al.*, 2014). A residual field gradient of order 1 nT/m over about 1 m^3 was reached after applying the equilibration procedure in all three directions in space for typically 100 s in each direction. Recently Altarev *et al.* (2015b) implemented the L-shaped coil arrangement shown in Fig 12, which enables magnetic saturation of all shells at once in a much shorter total time (< 50 s) with similarly small residual fields inside the shield. Numerical simulations have been compared to measurements showing that equilibration can be successfully fully modeled (Sun *et al.*, 2016). This is an important detail, as it is necessary to reverse the direction of the magnetic holding field and equilibrate the shields regularly during an experiment to control systematic effects.

Magnetic shielding for a proposed experiment to measure the EDM of the proton (see Sec. IV.G) in an electrostatic storage ring (zero applied magnetic field) with up to 800 m circumference presents a new set of challenges (Anastassopoulos *et al.*, 2016), and a toroidal shield made up of a number of three meter long cylinders is the most cost-effective option. To achieve proton-EDM sensitivity of $< 10^{-29}$ e-cm, the magnetic field must

Shield	f [Hz]	$B_{ext.}$ [μT]	SF(f)
TUM MSR both shells	0.01	2 (peak-to-peak)	279
TUM Insert	0.01	2 (pp)	$\sim 50,000$
TUM MSR + Insert	1.25	32 (pp)	$> 16,700,000$
TUM MSR + Insert	0.333	32 (pp)	$\sim 8,000,000$
TUM MSR + Insert	0.01	6.4 (pp)	$\sim 2,000,000$
TUM MSR + Insert	0.003	3.2 (pp)	$\sim 1,400,000$
TUM MSR + Insert + Cylinder	0.003	6.4 (pp)	$> 6,000,000^a$
BMSR-II	0.01	1 (rms) ^b	75000
BMSR-II	1	1 (rms)	2,000,000
Boston	0.01	1 (rms)	1630
Boston	1	1 (rms)	200,000

^a transverse shielding factor

^b rms value of a sinusoidal excitation

TABLE VI Measured damping factor $SF(f)$ of three shield-installations as function of external excitation strengths $B_{ext.}$ (either peak-to-peak or root mean square) and frequency f for very low frequencies. The TUM shield is at the Technical University of München (Altarev *et al.*, 2015a, 2014), BMSR-II is the Berlin Magnetically-Shielded Room at PTB (Bork *et al.*, 2002), and Boston refers to the BOSTON shield (Cohen *et al.*, 2002).

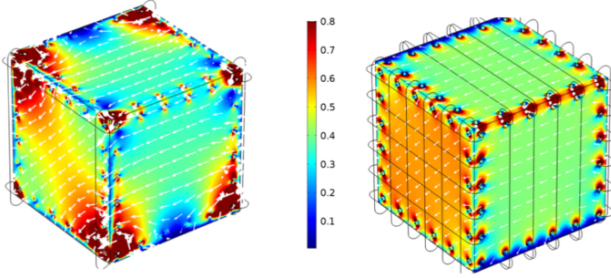


FIG. 12 (Color online) Magnetization of a permalloy box with equilibration coils. Left: Original L-shaped configuration with coils at the corners. Right: Distributed L-shaped configuration with coils arranged over the surfaces. The coils are solid lines. The color scale shows the magnetization in the permalloy in arbitrary units. Figure provided by Z. Sun.

be less than a few nT at any point, and the integrated transverse magnetic field along the path of the proton orbit must be less than ~ 25 pT for static fields. With counter-rotating proton beams, the important frequencies are 1-10 kHz, and the low-frequency shielding factor is therefore less crucial. With maximum acceptable distortions from the outside of $0.1 \mu T$ at 0.01 Hz (slower day-night drifts can usually be compensated or removed via frequent magnetic equilibration), the SF at 0.01 Hz is approximately 1000. Magnetic equilibration of a shield of this length would require equilibration of the individual cylindrical sections. Residual magnetization may build up near the equilibration coils due to non-uniformity of the magnetic flux at the ends of the cylinders. This can be compensated by a short ring of permalloy placed inside the shield, which corrects the magnetic distortions

caused by the equilibration coils (item 2 in Fig. 13).

Permalloy shielding has a number of characteristics that must be taken into account in shield design. These include

- i. the temperature dependence of the magnetic properties of the shielding material especially in the case of applied fields inside the shield, which in many cases coupled magnetically to the shield, may cause a temperature dependence of fields and gradients for the experiment;
- ii. a (magnetizable) conductor close to the experiment produces Johnson noise, which in turn causes magnetic-field noise (Lee and Romalis, 2008), also a consideration for the aluminum RF-shielding layer;
- iii. temperature differences also cause slowly changing magnetic fields in many conductors, which put additional constraints on the design of the experimental apparatus inside shields.

As an additional note, there are also permalloy foils available, which can be bent and wound around experimental apparatus for shielding purpose. Such materials are thin and are applied in many layers. The shielding factors obtained with such configurations tend to show a stronger directional dependence depending on the assembly. Also, the effective permeability of the material, once assembled, is significantly smaller than that of the raw material due to mechanical tension and air gaps.

Cryogenic shields

Cryogenic shielding, based on the Meissner effect with Type-1 superconductors *e.g.* Pb, has been envisioned for low-temperature EDM experiments. In contrast to

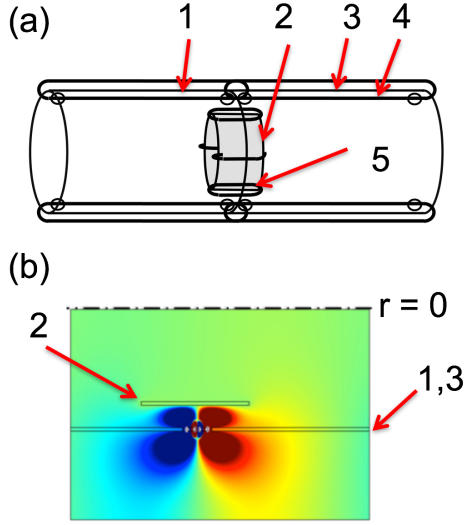


FIG. 13 (Color online) A possible solution for shielding of long experiments: (a) shows the basic concept of rings (1,3) (or comparable geometries), which are connected in segments. A correction ring (2) compensates for the magnetic distortions caused by the magnetic equilibration coils (4), which are wound around each ring. The compensation rings can also be equilibrated (5). Figure (b) shows a detail of a simulation of magnetic distortions caused by equilibration with rotation symmetry (dash-dotted line). (1,3) represent the walls of the shield with holes where currents for equilibration have been applied; (2) is the correction ring.

permalloy-based passive shields, cryogenic shields stabilize both external perturbations and instabilities in the applied magnetic field. Also, the residual magnetic field inside a cryogenic shield is frozen during the transition to superconductivity. Filippone *et al.* (2014) developed a prototype shield 4 m long with 1.2 m diameter, which provided a gradient less than 1 nT/m over 0.1 m volume. A disadvantage of cryogenic shielding is that the magnetic field cannot be reversed without warming up the shield.

In operation, the superconducting shield is surrounded by a room-temperature shield so that it can be cooled below the critical temperature in a small external field. Another approach is a hybrid combination of room-temperature and superconducting materials, for example a cylinder wrapped with METGLAS⁷ (Plaster, 2015). Magnetic-field noise less than $100 \text{ fT}/\sqrt{\text{Hz}}$ at $f = 0.01 \text{ Hz}$ has been achieved in hybrid configurations measured

⁷ METGLAS is commercial product

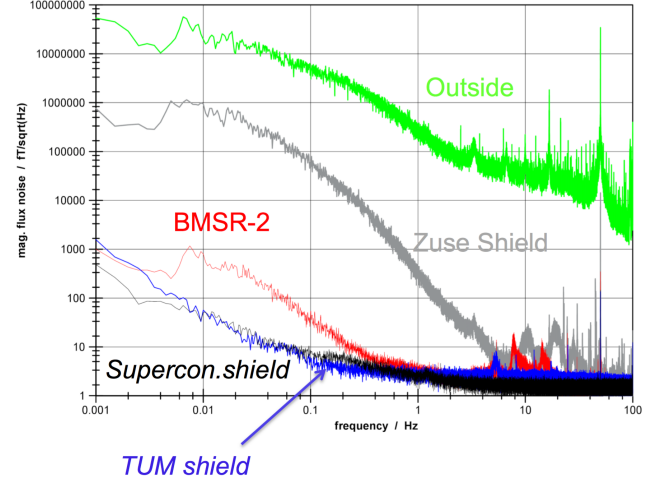


FIG. 14 (Color online) Comparison of noise in different shields measured with SQUIDs. Note that the noise of the SC shield (a cylinder cooled down to SC temperature inside the low magnetic field environment BMSR-II) and the cubic shields of the TUM MSR both show comparable performance. At very low frequencies, the intrinsic noise of the (different) SQUID systems combined and the integration time to record data for this plot dominate the performance; at high frequencies, the noise level is dominated by the experimental setup to perform the measurement. Figure provided with permission by M. Burghoff.

by Burghoff (2015). Figure 14 provides a comparison of damping factors for several shield configurations including the cryogenic shield placed inside the Berlin MSR-II.

Shields for cold-atom magnetometers with $<0.5 \text{ m}$ typical dimensions reach larger damping factors but worse residual fields and gradients. Shields used for atomic fountain interferometers have both much lower damping factors and larger residual fields (Dickerson *et al.*, 2012).

B. Magnetometers

Magnetometers measure the magnetic field at specific positions or averaged over specific volumes near the EDM experiment, with vector or scalar magnetic-field information. Magnetometers are classified either as external magnetometers, located in some way adjacent to the HV region, and comagnetometers that occupy the same volume at the same time as the EDM measurement. External magnetometer measurements can be used to estimate the magnetic flux through the EDM experiment volume, *i.e.* 4π magnetometry (Lins, 2016; Nouri *et al.*, 2015; Nouri and Plaster, 2014a,b) provides complementary information that may be sufficient without the complications of injecting the comagnetometer species into the EDM measurement chambers; however this requires that the interior of the EDM chamber be well characterized and the generation of magnetized spots inside the EDM

chamber can be continuously monitored *e.g.* by carefully monitoring electrostatic breakdowns.

Comagnetometers were first deployed in the electron-EDM Cs-beam measurement by Weisskopf (1968) and the Tl beam by Regan *et al.* (2002b). For atomic-EDM measurements, the concept relies on the Z dependence of sensitivity to the combination of P-odd/T-odd effects (*e.g.* electron EDM, electron-nucleus couplings and the Schiff moment) but comparable magnetic moments so that a frequency shift common to both species would arise from any magnetic-field source. Generally, atomic EDMs scale approximately as Z^2 for diamagnetic atoms and Z^3 for paramagnetic atoms. In principle, however, an experiment really measures the *difference* of the species' EDMs.

A comparison of the sensitivity and accuracy of commonly used magnetometers is presented in Fig. 15. Sensitivity characterizes the smallest change in the magnetic field that can be detected and generally improves with the measurement time, at least for short times. Sensitivity is clearly important for frequency stability and for monitoring systematic effects such as leakage currents. Accuracy, which is essentially calibration stability, is required for two (or more) separated magnetometers used, for example, to determine static and time-changing magnetic-field gradients.

Rb and Cs magnetometers

Alkali-metal magnetometers (usually Rb or Cs) have been developed and implemented since the inception of optical pumping, and their sensitivity and stability has been improved and optimized for a variety of experiments. Recently, Cs has been the main focus of magnetometers for EDM measurements because sufficient vapor density is attainable at low temperatures and due to the availability of optical components including diode lasers and optical fibers. Typically a Cs optical magnetometer uses glass cells with spin polarized or aligned vapor, read out via the transmission of resonant polarized light or optical rotation of off-resonant light.

Several magnetometer schemes are feasible, and the most common are called M_x magnetometers (Bloom, 1962) and NMOR sensors (Pustelny *et al.*, 2006). M_x sensors that monitor the Larmor frequency of atomic spins in a static field, *e.g.* along \hat{z} , using a perpendicular resonant oscillating field along \hat{x} ; NMOR refers to Nonlinear Magneto-Optical Rotation of linear polarization, which can be used for magnetometry when the light is modulated in frequency or intensity at the Larmor frequency. Though M_x magnetometers generally have simpler design and better stability over longer times, the RF magnetic fields (Aleksandrov *et al.*, 1995), may lead to cross talk among multiple sensors placed in close vicinity to each other. Metal cans as Faraday shields are used to

mitigate these crosstalk effects, but introduce magnetic-field Johnson noise. NMOR is a fully optical technique, and sensors can be built without any metallic components. Additionally, because the atoms can be prepared with a distribution of magnetic sub levels that has an alignment and no net magnetic moment, magnetic cross talk to other sensors is significantly reduced.

For Cs spin magnetometers, the frequencies for a typical magnetic field of $1 \mu\text{T}$ are 3.5 and 7 kHz for M_x and NMOR modes respectively. Typical response times are on the order of 10-100 ms. Operation modes include continuous pumping at the resonance frequency, self-oscillation and free precession decay, depending on the type of information needed (Budker and Romalis, 2007). In particular, free precession decay is systematically cleaner due to smaller interactions with pumping laser, whereas forced oscillation or self-oscillation may be affected by light shifts during the measurement, for example, a drift of the laser power can shift the center frequency of the resonance signal. A quantitative test of light-shifts has been undertaken by Patton *et al.* (2014).

The walls of the evacuated alkali metal vapor cells are generally coated with paraffin or other materials to improve wall-relaxation times T_2 (Singh *et al.*, 1972). Spin-relaxation times as long as $T_2 \sim 1\text{-}2$ s were observed for paraffin, and as long as 60 s in alkene-coated cells (Alexandrov *et al.*, 2002). Spin-exchange between atoms is a fundamental limitation that has been suppressed by increasing the alkali-metal density or attaining very high polarization in spin-exchange-relaxation-free of SERF magnetometers (Kominis *et al.*, 2003). Even the longest observed T_2 's are much less than the duration of a typical EDM measurement, and many independent measurements are in effect added incoherently to obtain the sensitivity for a measurement time τ :

$$\sigma_B \approx \frac{1}{2\pi\gamma} \sqrt{\frac{1}{N_A T_2 \tau}}, \quad (74)$$

where gyromagnetic ratio is $\gamma = 3.5 \text{ kHz}/\mu\text{T}$ for Cs and N_A is the effective number of spins observed in a time T_2 . For observation times τ up to about 10 s, the typically observed best sensitivity of these magnetometers is (Dang *et al.*, 2010)

$$\sigma_B \sim 1 - 10 \frac{\text{fT}}{\sqrt{\text{Hz}}} \times \frac{1}{\sqrt{\tau}}. \quad (75)$$

The dependence on τ of Eq. 74 does not hold for times greater than about 10-20 seconds due to many sources of instability, *i.e.* drifts in Cs density, laser intensity, light polarization, fibers and electronics as well as, for example temperature dependent interactions of the Cs spins with the vapor-cell walls.

Magnetometers that measure a single frequency proportional to the magnitude of a magnetic field provide information that is intrinsically a scalar. Several tech-

niques to extract vector information have been developed by Pustelny *et al.* (2006) and Afach *et al.* (2015) among others. In addition light-shift based approaches are very promising (Zhivun *et al.*, 2014). Laser-driven Cs atomic magnetometers can also be operated in an array, driven by the same laser source and optimized to disentangle noise and drifts of the system from the experiment, though the possibility of cross talk requires care in the deployment.

Optically pumped external and internal magnetometers with either ^3He or ^{199}Hg have also been proposed for the neutron EDM measurements by Ramsey (1984) and Green *et al.* (1998). The spins are optically pumped and then set to precess freely in the magnetic field. For ^{199}Hg , the readout is optical (Romalis *et al.*, 2001), whereas for ^3He , the precessing magnetization is monitored by either SQUID magnetometers (Allmendinger *et al.*, 2014; Kuchler *et al.*, 2016) or by Cs magnetometers (Koch *et al.*, 2015). For ^3He and ^{199}Hg nuclear spins, the transverse polarization life-times T_2^* are on the order of the duration of a neutron EDM measurement or longer. In the limit of low laser power, light-shift effects for Hg are negligible and do not show significant systematic effects. The practical sensitivity limit of ^{199}Hg magnetometers is a few fT for a 100 s integration time for both typical readout options using linearly and circularly polarized light, for different reasons. For ^{199}Hg , the Larmor frequency is $7.79 \text{ Hz}/\mu\text{T}$, which limits the bandwidth for monitoring magnetic field variations to about 1 Hz. Details of the ^{199}Hg comagnetometer for the ILL neutron-EDM measurements are provided in Sec. IV.A. Transverse spin-life-times $T_2 \sim 10^3 \text{ s}$ are easily possible for ^3He and have been demonstrated even for large volume cells (comparable to the dimensions of a neutron EDM chamber) at a few mbar pressures (F.Allmendinger *et al.*, 2014). The ^3He pressure is generally several mbar, as the detection of the polarization requires a measurable magnetic field at the position of the Cs or SQUID sensor. This in turn also causes an interaction of the He magnetometer with the neutrons in the EDM chamber and limits the pressure. A ^3He pressure of few mbar is a possible compromise up to an EDM sensitivity for the neutron of 10^{-28} e-cm . With a He cell, a wide variety of cell shapes and sizes can be chosen due to the low wall relaxation rates.

The determination of the shape and uniformity of the magnetic field is important to (i) determine geometric phases and (ii) find spurious leakage currents due to the HV applied across the measurement cell. For a neutron EDM measurement, the magnetic field over the whole experiment volume of $\sim 0.5 \text{ m}^3$ and during the entire few-hundred second duration of the measurement must be known at the fT scale, preferably with a bandwidth exceeding the typical spin precession frequencies. This requires specific arrangements of scalar and vector magnetometers to determine gradients and the sources of distortions. While the precision of individual sensor systems

can be $\text{fT}/\sqrt{\text{Hz}}$, the accuracy and long-term stability are typically limited by the absolute calibration and effects like the magnetic field caused by a sensor itself, typically on the scale of pT.

Two-photon magnetometry was originally suggested for ^{129}Xe as an alternative to ^{199}Hg used in the neutron-EDM measurement (Baker *et al.*, 2006) due to the smaller neutron-absorption cross section. Since the 147 nm single photon transition in Xe is too far in the UV, two 256 nm photons could be used for the free-precession measurement (Degenkolb, 2016). For ^{129}Xe magnetometry, the spin polarized gas sample would be prepared by SEOP (Rosen *et al.*, 1999). Ultrafast-two-photon spectroscopy (Zinkstok *et al.*, 2006) has the advantages of high peak intensity (two-photon absorption is proportional to the intensity squared) and coherence that allows two photons of different frequencies to combine to probe all atoms within the Doppler profile. Homogeneous broadening due to buffer gas collisions also helps cover the Doppler profile. Both the magnetometry signal and the efficiency for harmonic generation of the UV light depend on the laser's peak intensity, resulting in a considerable enhancement for an ultra-fast pulsed laser compared to a continuous-wave laser of the same average power. Picosecond pulses are a good compromise between high peak intensity and lower damage to crystals and optics since the dominant damage mechanisms scale with average intensity (Degenkolb, 2016). One particularly important feature of two-photon-magnetometry is the spatial resolution possible due to the quadratic dependence of the scattering rate on laser intensity I for two-photon transitions when atom diffusion is restricted by the buffer gas. Since the laser beam can be focused to a small waist and high intensity along the propagation direction, the scattering rate is highly position dependent and can be used to map out a magnetic field with resolution on the order of 1 mm.

C. Magnetic field-coil design and current sources

A crucial component of all EDM experiments is the applied magnetic field, which is generally required to be uniform and stable. Uniform fields are based on well-known techniques, but EDM experiments have brought new innovations. Stability requires both magnetic shielding discussed above and stability of the applied field, generally meaning stable currents. While current sources with relative stability approaching 10^{-7} over a 100 s integration time, effective stability of up to three orders of magnitude better is often required. However, at this scale it is difficult to disentangle the performance of the magnetic field sensor from the current instability. Ultra-stable current sources designed for very specific currents, loads have been developed by standard techniques of PI or PID feedback of the current sensed with low-temperature-

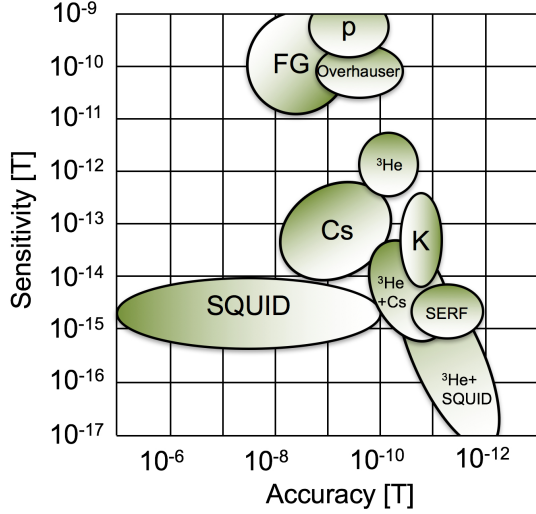


FIG. 15 (Color online) Sensitivity vs. accuracy of sensors used for low-field magnetometry in precision measurements in typical state-of-the-art configurations for flux-gate (FG), ^3He , alkali-metal magnetometers with Cs and K, spin-exchange-relaxation-free (SERF) magnetometers and combinations of ^3He and Cs or SQUID readout. The large area in parameter space is defined by the time constants and bandwidths of the systems, which result in a combination of drifts and noise. The term “sensitivity” is used to describe the response of the sensor to changes in the magnetic field, whereas “accuracy” is used here to describe the capability of resolving absolute fields, which is less important for EDM comagnetometry.

coefficient resistors compared to ultra-stable voltage references. Selection of discrete components to optimize offset drifts, gain-bandwidth product for different stages of the circuit and temperature stabilization of crucial components can provide routine performance of 10^{-7} and better. Feedback from magnetometers has been used to effectively stabilize magnetic fields to one part in 10^{11} over 1000 second time scales (Rosenberry, 2001).

The basic cylindrical coil is often called the cosine-theta coil, which is based on the principle that the surface current density for a uniformly magnetized cylinder with magnetization \vec{M} is $\vec{J} = \vec{M} \times \hat{n}$, *e.g.* for $\vec{M} = M\hat{y}$, $|J_z| \propto |\hat{y} \times \hat{n}| = \sin(\frac{\pi}{2} - \theta) = \cos(\theta)$ (θ is the angle measured from the x -axis). For a finite length cylinder, the end-cap wires can be positioned to reduce end effects as determined by calculations. Often permalloy is used as a flux return (Altarev *et al.*, 2012b), see *e.g.* Fig 16. Here, for an applied field of μT , the transverse magnetic fields should not exceed 0.1 nT.

Another very interesting approach to coil design for a source free volume ($\vec{\nabla} \times \vec{H} = 0$) is provided by solving Laplace’s equation for a magnetic scalar potential ϕ_B that satisfies the requirement, for example, of a uniform field $\vec{B} = B_0\hat{z}$ within a cylindrical volume. The currents on the surface of the volume correspond to equipotential lines, *i.e.* the current-carrying wires should run along

1/8 geometry of a B_0 coil

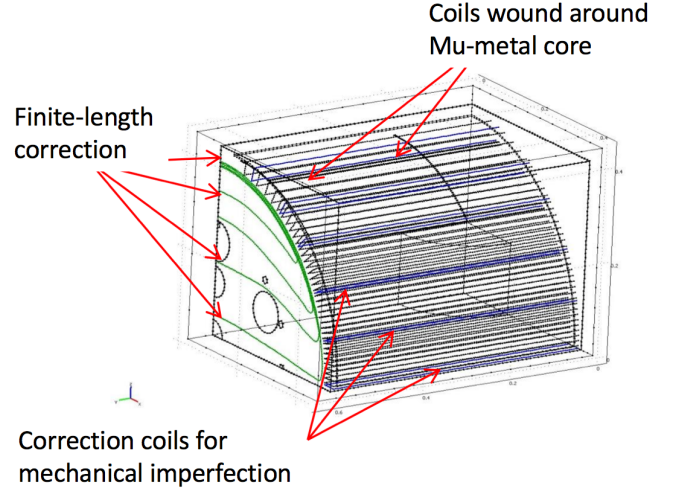


FIG. 16 (Color online) B_0 coil from the TUM apparatus. The coil consists of a closed box of mu-metal with a mu-metal cylinder inside the shield. The main coil is wound around the cylinder (see text); end coils and correction coils compensate for the finite length and imperfections in the geometry.

equally spaced equipotential surfaces. For the cylinder with uniform field, this of course also corresponds to the cosine-theta configuration; however this approach is particularly useful for different shapes of coil form, *e.g.* a rectangular box and other field profiles (Crawford, 2015).

As a side note, the characterization of field coils suitable for next-generation measurements requires a vector map over an extended volume with a resolution of transverse magnetic fields 10,000 times smaller than the main field direction. The precision of most components that meet the requirements of low magnetic impact is typically limited to an angular precision of few $\times 10^{-3}$ rad. Applying time dependent fields in different spatial directions may be used to help calibrating probes, but the procedures remain difficult.

D. Ultra-cold Neutron Sources

Ultra-cold neutrons (UCN), introduced by Zeldovich (1959) have velocities less than about 7 m/s, corresponding to kinetic energies $E_{kin} < \sim 260$ neV, temperatures of mK and wavelengths of ten’s of nm (Golub *et al.*, 1991). As a result of the long wavelength, the interaction of UCNs with material surfaces is characterized by a potential energy called the Fermi energy V_F that is positive for most materials. If $KE < V_F$, neutrons are repelled from the chamber walls for any angle of incidence and thus can be stored in a bottle, providing the working definition of UCNs. In Table VII we list UCN properties and potential energies in gravitational and magnetic barrier.

UCN Kinetic Energy	KE	$< 260 \text{ neV}$
UCN Velocity	v_{UCN}	$< 7 \text{ m/s}$
Neutron mass	m_n	$1.6798 \text{ kg}=939.565 \text{ MeV}$
Gravitational energy	$m_n g$	102 neV/m
Magnetic moment	μ_n	-60.4 neV/T
Gyromagnetic ratio	γ_n	$= \frac{2\mu_n}{\hbar} = 2\pi \times 29.16 \text{ MHz/T}$

TABLE VII Properties of UCNs and neutrons relevant to the neutron EDM experiments.

This shows that UCNs can be gravitationally confined in an approximately 2.5 m deep gravitational well and by a 4.33 T magnetic bottle.

UCN are in principle present in any moderated neutron source, which can be characterized by the neutron-density spectrum

$$\frac{d\rho(v_n)}{dv_n} = \frac{2\Phi_0}{\sqrt{\alpha}} \frac{v_n^2}{\alpha} \exp(-v_n^2/\alpha), \quad (76)$$

where $\alpha = 2k_B T/m$. For a thermal neutron source with core flux $\Phi_0 \sim 10^{15} \text{ cm}^{-3} \text{ s}^{-1}$ integrating eq. 76 up to 7 m/s results in a UCN density of

$$\rho_{UCN} = \int_0^{7 \text{ m/s}} \frac{d\rho(v_n)}{dv_n} dv_n \approx 100 \text{ cm}^{-3}. \quad (77)$$

Within cold moderators, typically at 20K, the density of UCN inside the moderator is increased to 10^3 cm^{-3} ; however UCN densities available to experiments are strongly reduced due to losses of UCN during extraction from the source and during transport to the experiment.

The best thermal UCN source is illustrated in Fig. 17 (Steyerl and Malik, 1989). Neutrons with $v_n < 20 \text{ m/s}$ are extracted from a 20K solid D_2 moderator through a vertically mounted neutron guide, slowing as they rise 17 m in the gravitational potential. The neutron guide is a tube that transports neutrons using total reflection from the surface, with the criterion being the normal component of the velocity $v_\perp \leq \sqrt{2V_F/m_n}$. At the end of the guide the neutrons reflect from the receding copper blades of a "turbine." The turbine blades act as moving mirrors that shift the neutrons to lower velocity. After several recoils, neutrons exit the turbine. Densities up to 10 UCN cm^{-3} are available for experiments,

Most modern UCN sources are based on superthermal conversion introduced by Golub and Pendelbury (1977). This achieves higher phase-space density than thermal sources using a medium that is not in thermal equilibrium with the neutrons. For example, figure 18 shows the dispersion curves for a free neutron and for thermal excitations in superfluid-helium (SF-He), a typical choice for a superthermal source material. The curves cross at two points: $E_0 = 0$ and $E_1 = E_0 + \Delta$, where $\Delta \approx 1 \text{ meV}$ corresponding to neutron wavelength $\lambda_n = 8.9 \text{ \AA}$ (Golub *et al.*, 1991). This is effectively a two-state system, and

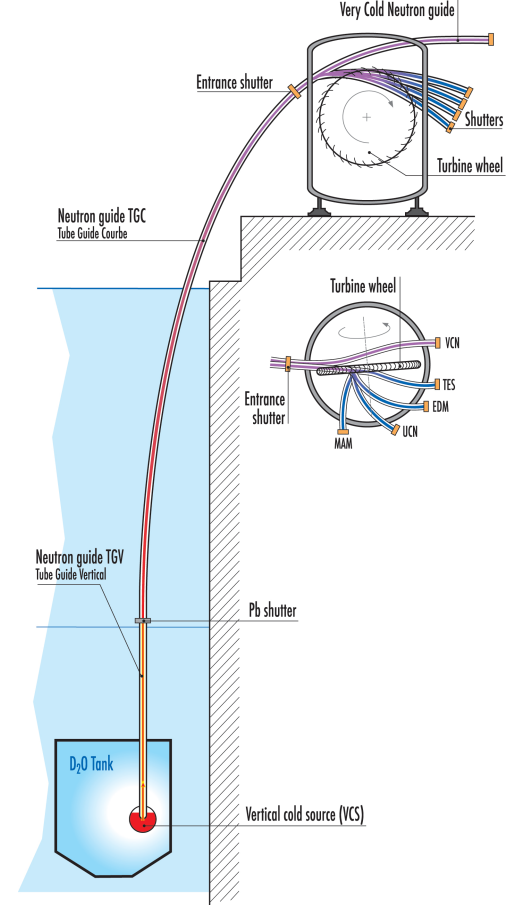


FIG. 17 (Color online) UCN source at PF2 at The Institut Laue Langevin in Grenoble, France (ILL). Neutrons from the low-energy tail of the cold-neutron spectrum are guided upward and loose energy in the gravitational potential. The turbine further shifts the spectrum to longer wavelengths to produce UCN that are provided to a number of experiments including the EDM. Figure provided by ILL (Institut-Laue-Langevin, 2008).

neutrons at E_1 can resonantly transfer their energy to the SF-He resulting in final neutron energy near $E_0 = 0$ with a small spread due to the effective width of the excitations. The probability for the neutrons to absorb the energy from an excitation Δ and to excite a state in the medium are related via the principle of detailed balance (Golub *et al.*, 1991),

$$\frac{\sigma(E_{UCN} \rightarrow E_{UCN} + \Delta)}{E_0 \rightarrow E_{UCN}} = \frac{E_{UCN} + \Delta}{E_{UCN}} e^{-\Delta/k_B T} \quad (78)$$

For incident neutron energy $k_B T \geq \Delta$, the medium will accumulate "down-scattered" neutrons, while the reverse process is exponentially suppressed. This enables the accumulation of neutrons at low energy and an increase of

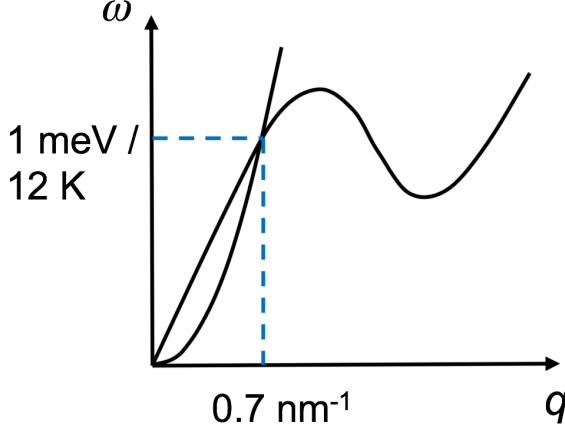


FIG. 18 (Color online) Single phonon dispersion curve with minimum at $q \approx 2 \text{ nm}^{-1}$ and the free neutron $E_n = p_n^2/2m_n$ intersect at $E_n = 0$ and $E_n = 0.7 \text{ nm}^{-1}$ or $\lambda_n = 8.9 \text{ Å}$.

the phase space density of the neutrons without violating Liouville's theorem, as the UCN and quasi-particle excitations in SF-He are both part of the thermal system. The superfluid transition requires temperatures below 2.17 K; however due to thermal up-scattering, a temperature of $\leq 0.6 \text{ K}$ is optimal for SF-He.

A second-generation SF-He source at ILL (SUN2) is shown in Fig. 19 (Leung *et al.*, 2016). The SF-He is held in a container with inner surfaces that have a large Fermi-potential *e.g.* for beryllium $V_F = 252 \text{ neV}$, or with the help of magnetically enhanced confinement (Zimmer and Golub, 2015). The cryogenics package (not shown) dissipates 60 mW at 0.6K. Less than part-per-billion ^3He contamination in the superfluid is essential due to the strong absorption of neutrons on ^3He . Neutrons with 8.9 Å wavelength enter the SF-He container through one of the UCN reflecting walls. Neutron beams available for such sources are typically cold beams that are guided to experiments 10's of meters distance from the neutron source. Neutron fluxes at ILL for the H172A beamline are $2.62 \times 10^7 \text{ neutrons cm}^{-2}\text{s}^{-1}\text{Å}^{-1}$ (Piegsa *et al.*, 2014). The UCN density for a UCN lifetime τ_{tot} inside the helium source is

$$\rho_{UCN} = \tau_{tot} N_{SF} \int \frac{d\Phi_0(E_0)}{dE_0} \sigma(E_0 \rightarrow E_{UCN}) dE_0, \quad (79)$$

where $\sigma(E_{UCN} + \Delta \rightarrow E_{UCN})$ is the down-conversion cross section, and N_{SF} is the SF-He density. The specific production rate $N_{SF}\sigma(E_0 \rightarrow E_{UCN})$ in helium has been calculated by Golub and Pendelbury (1977) to be $N_{SF}\sigma = (4.55 \pm 0.25) \times 10^{-8} \frac{d\Phi_0}{d\lambda}$ at $E_0 = 8.9 \text{ Å}$, compared to $N_{SF}\sigma = (3.47 \pm 0.13) \times 10^{-8} \frac{d\Phi_0}{d\lambda}$, which was measured by Baker *et al.* (2003).

Minimizing losses during UCN production are critical for achieving high UCN densities. The loss rate is ultimately

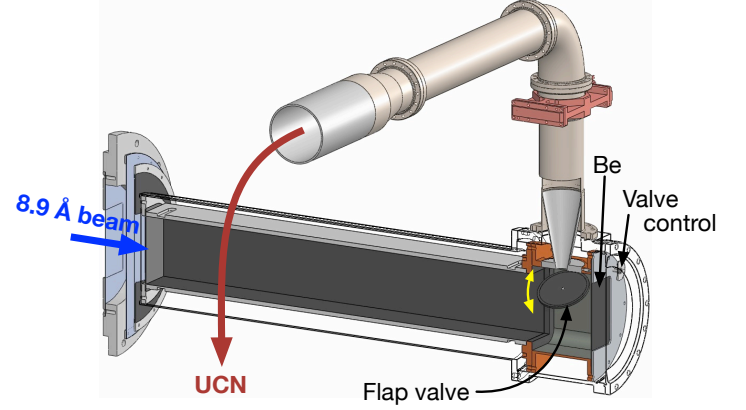


FIG. 19 (Color online) Schematic diagram of the ILL SUN2 source described in the text. Figure adapted from Leung *et al.* (2016) by K. Leung and O. Zimmer.

limited by the neutron lifetime τ_n with additional contributions for a total loss rate:

$$\frac{1}{\tau_{tot}} = \frac{1}{\tau_{up}} + \frac{1}{\tau_{walls}} + \frac{1}{\tau_{slits}} + \frac{1}{\tau_{abs}} + \frac{1}{\tau_n} \quad (80)$$

1. The thermal up-scattering rate $1/\tau_{up}$ is small at the typical operating temperature of about 0.8 K (see eq. 78), and below 0.6 K performance does not further improve (Piegsa *et al.*, 2014).
2. The wall collision losses $1/\tau_{wall} = \mu\nu$ are defined by the energy dependent parameters, loss probability per wall collision $\mu \approx 10^{-4}$ and the wall collision frequency in the trap $\nu \sim 10 - 50 \text{ s}^{-1}$, given in Table VIII.
3. $1/\tau_{slits}$ is related to the mechanical precision of the trap, which defines the leakage of UCN out of the trap, which has been reduced with low-temperature Fomblin oil (a fluorinated, hydrogen free fluid with low-neutron-absorption) (Serebrov *et al.*, 2008)
4. τ_{abs} is the UCN absorption due mostly to ^3He in the trap.

In practice, τ_{tot} greater than 150 s has been achieved in demonstration setups (Piegsa *et al.*, 2014), as well as densities of $220 \text{ cm}^{-3}\text{s}^{-1}$ with a Fermi-potential of the trap of effectively only 74 neV. Here, low-temperature Fomblin oil was used to also close gaps and slits in the trap volume. As a side note, such a low energetic spectrum is very advantageous for EDM measurements, as

losses, depolarization and velocity-dependent systematic effects are smaller.

Many factors limit UCN-source performance including, Fermi potential of wall materials, other contributions to storage lifetime, heat input due to the geometry of the extraction guide and through the neutron entrance, source volume dimensions, beam size, and beam divergence. UCN densities can be increased to 10^3 cm^{-3} with an optimized 8.9 \AA neutron beam larger storage volumes, less dilution and surface-coating improvements.

Extraction of the UCN from the source to the experiment (Masuda *et al.*, 2002; Piegsa *et al.*, 2014) requires either a window or a vertical exit from the superfluid He chamber such as indicated in Fig. 19. For a superfluid He source, the UCN are accumulated in the source volume during production and filling of the experimental volume reduces the density in proportion to the ratio of the source volume relative to the total volume of the source, guides, and experiment. The experiment should therefore be placed close to the source, and the ratio of source volume to experiment volume should be as large as possible.

An interesting side note is that UCN production is a coherent phenomenon in superfluid helium. Thus the polarization of an incident neutron beam is preserved, and it is possible to produce polarized UCN from an already polarized beam cold-neutron beam. Another consideration is UCN production in a high magnetic field, which can also provide a highly polarized sample of neutrons as required for an EDM measurement (Zimmer and R., 2015). The alternative - polarizing UCN after their production and extraction from the source using magnetized foils or magnetic field gradients - at a minimum rejects half of the UCN.

The possibility of directly performing a UCN storage experiment inside the source has led to a new experimental concept described in Sec. IV.A. This would also enable the use of higher electrostatic voltages due to the dielectric properties of the SF-He. Breakdown strengths exceeding 25 kV/cm have recently been demonstrated in electrode gaps realistic for next generation neutron EDM measurements (Ito *et al.*, 2014).

Alternative superthermal converters include solid deuterium, deuterated methane or oxygen, as well as other (para)magnetic/spin polarized substances. (Atchison *et al.*, 2011). Oxygen and other materials for superthermal UCN production are based on increasing the phase space density and modes of UCN extraction and are discussed in Nesvishevski (2002) and Zimmer (2014a).

Solid deuterium (SD_2) molecules consisting of two spin-one deuterons combine to total nuclear spin $I = 0$ or 2 for ortho-deuterium ($o\text{D}_2$) and $I = 1$ for para-deuterium ($p\text{D}_2$). The rotational ground-state for spin-one bosons is $o\text{D}_2$. (For H_2 , the ground state is parahydrogen with $I = 0$.) Rotational excitations in SD_2 for

rotational quantum number J are given by:

$$E_J = \frac{\hbar^2}{2mR^2} J(J+1) = 3.75 \text{ meV} \times J(J+1), \quad (81)$$

comparable to cold neutron energies $< 10 \text{ meV}$ for low-lying excitations (Yu *et al.*, 1986). At room temperature (25 meV) the six $I = 0, 2$ $o\text{D}_2$ states and the three $I = 1$ $p\text{D}_2$ states are approximately equally populated, so the population of ortho:para states is 2:1. For UCN production, a concentration of $o\text{D}_2$ of $> 95\%$ is necessary, which requires low temperatures as well as a magnetic converter to couple to the dueteron spins. The typical converter material is hydrous iron (III) oxide, cooled to below the triple point of deuterium, in a separate apparatus outside the source (Liu *et al.*, 2003). The converted $o\text{D}_2$ is then transferred to the UCN source in gaseous state without losing the ortho-state configuration due to very long thermal relaxation times in the absence of a converter. The conversion cross section from cold neutrons to UCN for a deuterium density ρ_{H_2} is given by (Atchison *et al.*, 2005)

$$\sigma_{\text{sD}_2, 8\text{K}}^{\text{CN} \rightarrow \text{UCN}} \rho_{\text{H}_2} \sim 1.11 \pm 0.23 \times 10^{-8} \text{ cm}^{-1}. \quad (82)$$

However the momentum acceptance for cold neutrons is much greater than for SF-He. The UCN storage time inside the sD_2 source is given by

$$\frac{1}{\tau_{\text{UCN}, \text{sD}_2}} = \frac{1}{\tau_{\text{up}}} + \frac{1}{\tau_{o/p}} + \frac{1}{\tau_{\text{D-abs}}} + \frac{1}{\tau_{\text{H-abs}}} + \frac{1}{\tau_{\text{cryst}}} \quad (83)$$

with $1/\tau_{\text{up}}$ the losses due to thermal up-scattering, elastic scattering of UCN with mK temperature on nuclei at few K temperatures in the source, $1/\tau_{o/p}$ losses due to scattering on $p\text{D}_2$ and further absorption losses on deuterium and hydrogen, as well as losses due to scattering in the crystal. Most loss channels can be controlled to rates of $(150 \text{ ms})^{-1}$, totaling to $\tau_{\text{UCN}, \text{sD}_2} \sim 75 \text{ ms}$ over-all life-time in the perfect $o\text{D}_2$ crystal at 4 K . In total, UCN densities of 10^4 cm^{-3} are in principle feasible inside the source. In contrast to the SF-He source, which requires accumulation in the source for several hundred seconds followed by dilution into the guides and experimental volume, the sD_2 provides an effectively continuous source of UCN, provided efficient extraction to the experiment within a time $\tau_{\text{UCN}, \text{sD}_2}$. This restricts the sD_2 layer to $\sim 1 \text{ cm}$ thickness, not taking into account pre-moderation or thermal engineering issues that may require increased thickness of the sD_2 layer.

Though the typical life-times in solid deuterium and the energy dependent production rate have been well determined experimentally, the practical performance of solid deuterium based sources is typically lower than expected. For example, in practical sources the shrinkage of the crystal by about 10% during the cool-down from 18 K to 4 K causes cracks and reduces thermal contact to the cooling apparatus. Cracks in the crystal also change the neutron mean-free path in the source and thus affect

Material	V (neV)	Loss per bounce	Ref	Depolarization	Ref
DPe (300K)	214	1.3×10^{-4}	<i>a</i>	4×10^{-6}	<i>b</i>
DLC on Al substrate (70K)	270	1.7×10^{-4}	<i>c</i>	0.7×10^{-6}	<i>c</i>
DLC on Al substrate (300K)	270	3.5×10^{-4}	<i>c</i>	3×10^{-6}	<i>c</i>
DLC on PET substrate (70K)	242	1.6×10^{-4}	<i>c</i>	$15 \pm \times 10^{-6}$	<i>c</i>
DLC on PET substrate (300K)	242	5.8×10^{-4}	<i>c</i>	$(14 \pm 1) \times 10^{-6}$	<i>c</i>
Fomblin 300K	106.5	2.2×10^{-5}	<i>d</i>	1×10^{-5}	<i>e</i>
Be (10 K)	252	3×10^{-5}	<i>d</i>	1.1×10^{-5}	<i>e</i>
Be (300K)	252	$(4 - 10) \times 10^{-5}$	<i>d</i>	1.1×10^{-5}	<i>e</i>
NiP	213	1.3×10^{-4}	<i>f</i>	$< 7 \times 10^{-6}$	<i>g</i>
^{58}Ni	335	<i>h</i>			
Fe/steel/stainless	210	<i>h</i>			

TABLE VIII Properties of materials for UCN production, storage and transport showing loss per bounce and depolarization per bounce. DPe is dueterated polyethelen; DLC is diamond-like carbon. References *a*: (Brenner *et al.*, 2015); *b*:(Ito *et al.*, 2015); *c* (Atchison *et al.*, 2007); *d*: (Serebrov *et al.*, 2005); *e*: (Serebrov *et al.*, 2003); *f*:(Pattie *et al.*, 2017); *g*: (Tang *et al.*, 2017); *h* (Golub *et al.*, 1991).

Source	Type	Converter	Cycle time	UCN/cm ³ at EDM experiment	Comment
ESS	spallation	under discussion	-	-	future
ILL PF2	reactor	lD ₂ + turbine	continuous	50 /cm ³	operating
ILL SUN-II	reactor, CN beam	SF SF-He	200 s	< 10/cm ³ (note 1)	operating
ILL SuperSUN	reactor, CN beam	SF-He	500 s	> 50-1000/cm ³ (note 2)	planned
LANL	spallation	sD ₂	continuous	60/cm ³	operating
LANL upgrade	spallation	sD ₂	continuous	few 100/cm ³	planned
NCSU	reactor	sD ₂	continuous	> 1000/cm ³	planned
PIK	reactor	SF-He	few 100 s		future
PSI	spallation	sD ₂	few 100 s	~2/cm ³	
SNS	spallation	SF-He	few 100 s	500/cm ³	EDM chambers
TUM	reactor	sD ₂	continuous	~1000/cm ³	future
TRIUMF	spallation	SF-He	few 100 s	> 1000/cm ³	planned
TRIGA Mainz	pulsed reactor	sD ₂	10 min	~10/cm ³	operating
WWRM	reactor	SF-He	few 100 s	10 ⁴ /cm ³	planned

TABLE IX Existing and projected UCN sources and performance relevant to EDM experiments. Note that the numbers are difficult to compare and relate strongly to the actual experiment. Notes 1) UCN density includes dilution due to the volume of EDM chamber and guides; 2) UCN density includes dilution in volume; the source will have two stages, with polarized UCN production in the second stage, leading to less transport losses. Legend: ESS is the European Spallation Source, ILL PF-2 is the UCN source shown in Fig. 17 and Sun-II/SuperSun are SF-He sources at ILL; LANL refers to the Los Alamos S-D₂ source, NCSU is the sources at the North Carolina State University pulsed reactor, PIK is the Gatchina reactor, PSI the S-D₂ UCN source, SNS is the spallation neutron source with UCN production incorporated into the EDM experiment, TUM is the Technical University of München FRM-II reactor source, TRIUMF the SF-He source at the TRIUMF proton cyclotron, TRIGA is a pulsed reactor at Mainz University and WWRM is PNPI is St. Petersburg.

the extraction efficiency. Thermal stress and geometrical alignment of the source may also require preparation of the crystal from the gas phase instead of freezing from the liquid state. A further important aspect is guiding the neutrons from the sD₂ source to an experiment. For sD₂ sources placed inside a reactor, long guides to the experiment had previously been considered a major issue but was successfully tested at ILL by Zechlau (2016) with transmission greater than $> 50\%$ for 80 mm ID, 22 m long guides coated with NiMo85-15 and including three 90° bends.

A sD₂ source provides a steady flux of UCN from the source and can in principle be interfaced directly to the neutron-guide vacuum; however, any UCNs that diffuse back to the D₂ will be lost due to the short UCN storage time τ_{UCN} . On the other hand, the UCN density provided by a continuous sD₂ source does not depend on the size of the experiment (to first order), and large experiment volumes can be filled with UCN. Typical UCN storage experiments like a neutron EDM measurement use a chamber, which is filled for 10's of seconds, and the UCNs are stored for 100's of seconds. For EDM experiments, the duty cycle of the source can be less than 10%, as the filling times of UCN storage chambers are typically 10-100 s and the cycle time ≈ 1000 s, which is important for accelerator-based spallation neutron sources that share the primary accelerator beam. An example for such a quasi-continuous beam is the synchro-cyclotron at PSI (Anghel *et al.*, 2009), which provides about a 1 mA, 690 MeV, proton beam incident on a heavy metal spallation target for 4 s with a duty cycle of 1%. The ILL-Sussex-Rutherford EDM apparatus was moved to PSI to the use neutrons from the super-thermal sD₂ converter with reported performance comparable to the previous densities achieved at ILL (Rebrequend, 2014). Another pulsed sD₂ source is installed at the pulsed TRIGA reactor in Mainz, where a 200 MW-20 ms neutron pulse produces UCN, which leave the source quickly and can - with proper timing - be captured in an experiment using mechanical shutters. A density of order 10 UCN-cm⁻³ in a few 10's of liter-sized experiments can be achieved (Lauer and Zechlau, 2013).

The UCN source at Los Alamos National Lab consists of a spallation target for thermal neutron production, a cold plastic pre-moderator and a sD₂ crystal. UCN are directly extracted through a diamond-like-carbon coated guide and a shutter to the experiments. A density of 52 ± 9 UCN/cm³ has been seen at a port outside of the biological shield (Saunders *et al.*, 2013), and an upgrade providing significant improvement has been reported (Ito *et al.*, 2017).

A summary of existing UCN sources is provided in Table IX. The superfluid SF-He sources (SUN and SUN-II at ILL, use cold neutron beams and the source at RNPC coupled to a spallation target with extraction to vacuum) are in principle working at the level of theoretical esti-

mates. For these sources scaling, to larger neutron flux, resulting in larger heating from the primary beam require increased cryogenic capacity, but is not otherwise expected to significantly change the performance. At ILL, the SuperSUN source is currently being built. Also the sD₂ sources at LANL and at the TRIGA reactor at Mainz are also working as expected, though at comparably low average power. The pulses in a TRIGA reactor are short and the crystal quality does not suffer strongly from the resulting thermal stresses and radiation damage. Larger incident neutron flux has apparently produced radiation damage in the crystal (Wigner, 1946). The a recent upgrade of the LANL source demonstrates that the initial issues of these sources are mostly technical and can be mitigated (Ito *et al.*, 2017).

IV. EXPERIMENTS

In this section we review the current status and prospects of experimental efforts for the neutron, paramagnetic atoms and molecules, diamagnetic atoms ¹⁹⁹Hg and ¹²⁹Xe as well as octupole deformed ²²⁵Ra and ^{221/223}Rn, solid-state electron EDM measurements and future storage-ring measurements of proton and light nuclei EDMs. The results so far are summarized in Table I.

A. The Neutron

Miller *et al.* (1967) performed the first experiments to search for the neutron EDM with a cold neutron beam with the very first result $(-2 \pm 3) \times 10^{-22}$ e-cm. By 1980, the beam measurements became systematics limited due to complications arising from beam divergence and motional ($\vec{v} \times \vec{E}$) effects. These systematic issues led to experiments using stored UCN, trading the advantage of higher intensity of the neutron beams for long observation times (Altarev *et al.*, 1980). The layout of two recent stored-UCN experiments is shown in Fig. 20. For the ILL-Sussex-Rutherford experiment (Fig. 20a) (Baker *et al.*, 2006) a single chamber is used along with a comagnetometer, while the Gatchina experiment (Fig. 20b) (Altarev *et al.*, 1992) employs a pair of chambers with opposite electric fields, but predominantly common-mode magnetic field drifts (the magnetic-field variations in the two chambers are correlated and, for a homogeneous field, equal). The ILL experiment is analyzed as a spin-clock comparison using a variation of Ramsey's separated oscillatory field technique to measure two spin-polarized species (neutron and ¹⁹⁹Hg comagnetometer) in the same volume at the same time. In the Gatchina approach, both chambers have very similar systematics and the velocities of the UCN are small enough so that many systematic effects are negligible at the 10^{-26} e-cm level. The results for both experiments

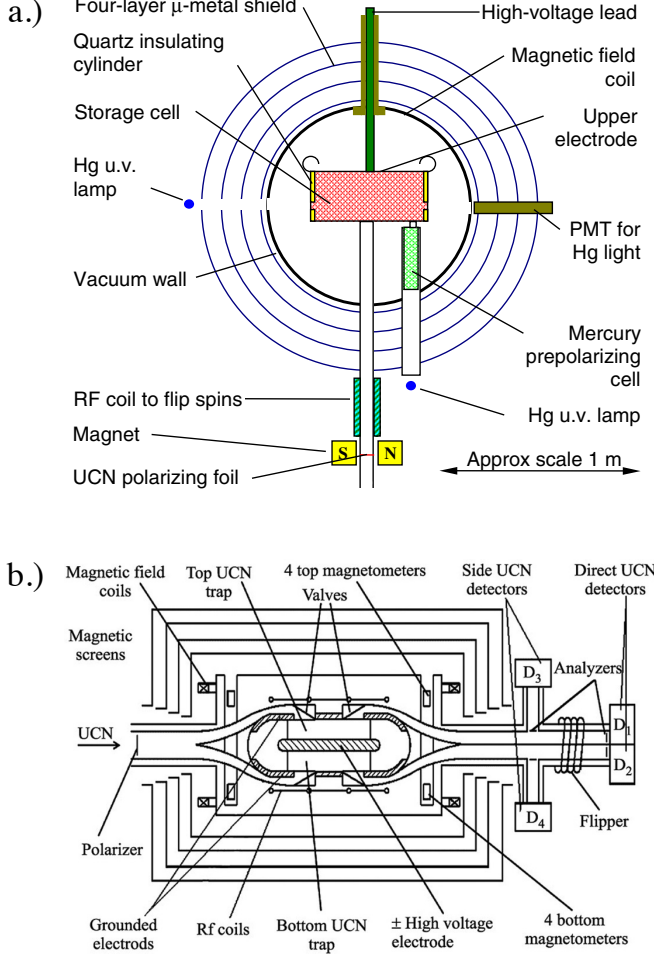


FIG. 20 (Color online) The most recent neutron EDM apparatus, which deployed stored UCN and different means for the control of systematic effects (a) the ILL-Sussex-Rutherford experiment with one chamber for UCN and a comagnetometer from Baker *et al.* (2006); (b) the Gatchina experiment with two neutron storage chambers with parallel and anti-parallel E and B field orientations measured simultaneously from Serebrov *et al.* (2015). Both experiments are run with the storage chamber in vacuum at room temperature. Figures used with permission.

are statistics limited. A detailed discussion of systematic effects is provided in Sec. IV.A.

In Ramsey's technique, an interferometer in time is realized by comparing the phase from a spin-clock with frequency ω_L , the Larmor precession frequency, with the phase of a reference clock with frequency ω_R after a fixed measurement time τ as illustrated in Fig. 21. The observation time τ is optimally chosen based on the storage time of the particles (in the case of trapped UCN a few-hundred seconds) or the particle flight time for a beam measurement (milli-seconds) and, in some cases, the transverse polarization lifetime T_2^* for the comagnet-

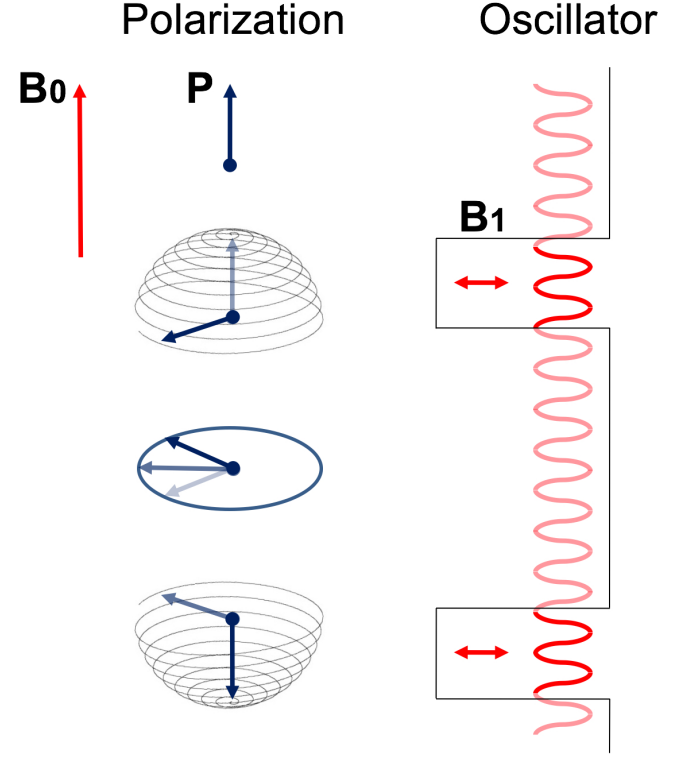


FIG. 21 (Color online) Ramsey's technique of separated oscillatory fields. The experiment starts out with polarized particles in a stable and homogeneous magnetic field B_0 , while a stable external oscillator running at ω_R near the Larmor frequency ω_L of the particles in the B_0 field. First a " $\pi/2$ pulse" is applied to the polarized particles, rotating the polarization to the plane normal to B_0 , alternatively creating a superposition of spin-up and spin-down. The spins and external clock and evolve independently, until a second " $\pi/2$ pulse" is applied. The second pulse measures the phase built up during the free precession interval. The time evolves from top to bottom in the figure.

tometer. The relative phase of the spins and the clock evolve at the difference frequency, and the phase after a time τ is $\Delta = (\omega_L - \omega_R)\tau$. This is read out using the polarization P_z , *i.e.* the projection of the spin along the B_0 field after the second pulse is applied. In terms of the number of neutrons detected with spin parallel (N_\uparrow) and antiparallel (N_\downarrow) to B_0 at the end of the free-precession cycle, the polarization is:

$$P_z = \frac{N_\uparrow - N_\downarrow}{N_\uparrow + N_\downarrow}. \quad (84)$$

For $\Delta = 0, \pi/2, \pi$, $P_z/P_0 = -1, 0, 1$, respectively, where P_0 is the maximum magnitude of the polarization. To maximize sensitivity to a change of the frequency, $\Delta\phi = \pm\pi/2$ is chosen to provide the maximum slope of the fringes:

$$\left. \frac{\partial P_z}{\partial \omega} \right|_{\Delta=\pi/2} \approx P_0 \tau. \quad (85)$$

The EDM signal adds an leading to

$$\delta P_z = \frac{2d_n E}{\hbar} P_0 \tau. \quad (86)$$

The statistical precision of the Ramsey measurement is:

$$\sigma_{d_n} = \frac{\hbar \sigma_{P_z}}{2EP_0\tau}, \quad (87)$$

where the error of each P_z measurement is

$$\sigma_{P_z} \approx 1/\sqrt{N_\uparrow + N_\downarrow}. \quad (88)$$

Magnetometers for Neutron EDM Experiments

Any uncompensated change in the magnetic field between two subsequent or spatially separated measurements with opposite electric field will falsely appear as an EDM:

$$d_{false:\Delta B} = \frac{\mu\Delta B}{E}. \quad (89)$$

For a random-noise spectrum of magnetic-field variations, this effect will be reduced in proportion to \sqrt{M} for M subsequent electric-field reversals; however, any correlation of the electric and magnetic-field, for example due to leakage currents across the storage cell, will not be averaged. In either case, monitoring the magnetic field is essential to a successful measurement. As an example, for a measurement precision of $\sigma_{d_n} = 10^{-28}$ e-cm and an electric field $E = 10^4$ V/cm and $M = 10^4$, the required magnetic field measurement precision is $\delta B \approx 2$ fT. This represents a significant challenge for magnetometry techniques. Due to unavoidable inhomogeneity and drifts of magnetic fields, the magnetic field can either be measured (i) directly at the position of the measurement, preferably at the same time, with a comagnetometer, or (ii) with magnetometers surrounding the experiment to estimate the full flux entering and leaving the experiment at the time of the measurement.

In the case of the stored UCNs, the observation time τ is several-hundred seconds, which restricts the choice of comagnetometers to species with coherence times comparable to τ . For the ILL-Sussex-Rutherford experiment nuclear-spin polarized ^{199}Hg was chosen (Green *et al.*, 1998) for several reasons: the upper limit on the ^{199}Hg EDM is much smaller than the neutron-EDM sensitivity (see Sec. IV.E); the coherence time of ^{199}Hg can be 100 s or more; the coherence time combined with the large signal-to-noise ratio of the optically pumped atoms provides high sensitivity to magnetic field variations. The ^{199}Hg vapor was polarized with a 254 nm light from a discharge lamp or laser in a pre-polarizing chamber, adjacent to the neutron EDM apparatus. Before the UCN were loaded, the polarized Hg vapor was added to the neutron storage volume at a pressure of $\approx 10^{-4}$ mbar,

the vapor pressure of Hg at room temperature. At this low pressure, the macroscopic magnetic field due to the ^{199}Hg did not appreciably shift the spin precession of the neutrons. Spin-precession (free induction decay) was initiated with a resonant $\pi/2$ pulse that rotated the Hg spins into the plane transverse to \vec{B}_0 . The ^{199}Hg precession frequency was determined by the time-dependence of the absorption of a weak probe beam of circularly polarized 254 nm light shined through the storage chamber during the first and last 15 seconds of the measurement, eliminating light shifts during the free-precession interval. The polarization and readout light intensities were balanced to optimize the performance of the magnetometer. With a mean velocity of $v_{rms} \approx 193$ m/s, the ^{199}Hg atoms sampled the entire storage volume in a time short compared to a Larmor cycle of $(7.79 \text{ Hz})^{-1}$ s effecting motional narrowing (Mundy, 1983). Spin-coherence times T_2^* were up to about 400 s, and the ^{199}Hg frequency was measured with precision $\approx 2 \mu\text{Hz}$ in a single measurement.

It was observed that the ^{199}Hg coherence time T_2^* dropped to about 130 s when the high voltage was applied. Cleaning the walls with an oxygen discharge at 1 torr restored the ^{199}Hg T_2^* to 400 s; other ways to improve this behavior are being investigated, including adding helium as buffer gas to reduce the Hg mean free path. Introducing helium gas also affects the high voltage breakdown strength of the storage cell. Another advantage of helium buffer gas is that the rate of depolarizing wall collisions of Hg atoms is reduced by the shorter mean free path. The use of a comagnetometer further reduces the choice of wall coatings for neutron storage, as any contact with metallic surfaces will cause loss of ^{199}Hg polarization, while preserving the UCN polarization. The presence of Hg also appeared to lead to increased breakdowns for voltages above about 150 kV applied to the electrode. Several planned future room-temperature neutron EDM experiments also plan to use ^{199}Hg as a comagnetometers.

Neutron-EDM Systematics

Improved sensitivity of EDM experiments led to the discovery of new systematic effects that have been incorporated by Pendlebury *et al.* (2015) into the analysis of the Baker *et al.* (2006) result. These can be (i) direct false effects, e.g. leakage currents caused by the applied high-voltage anywhere close to the EDM measurement setup that produce stray magnetic fields; (ii) indirect false effects, such as the geometric phase effect discussed below. To put this in perspective, for the neutron with an applied electric field of 10 kV/cm, an EDM of 10^{-26} e-cm the frequency shift is $\Delta\omega \approx 50$ nHz, which is the shift of neutron precession frequency for a magnetic field change of 2 fT. If the change or reversal of electric field results in

correlated magnetic field change (magnitude and sign), a false EDM would arise. For the storage chamber used by Baker *et al.* (2006) with $r = 0.2$ m and assuming a full turn around the cell, a leakage current of less than about 1 nA is required. (For smaller diameter chambers, the leakage-current requirements are more stringent.)

A leakage current would produce a magnetic field that changes or even reverses with the electric field magnitude and orientation. This would create a false EDM signal, that should be compensated or monitored by the comagnetometer or external magnetometers; however as noted below the UCN and ^{199}Hg positions are slightly different so a non-uniform leakage current induced magnetic field, which is likely to be the case, would not be perfectly compensated. For $E = 10$ kV/cm and a 50 cm diameter storage bottle, a leakage current of 1 nA spiraling half way around the bottle would shift the neutron frequency by about 15 nHz; combined with a height difference of 2 mm compared to the bottle height of 20 cm and assuming a linear dependence on position, the resulting false EDM not compensated by comagnetometry would be of order 10^{-28} e cm. Thermally induced currents (Johnson noise) in the electrodes with stationary patterns (Schnabel, 2014) can cause non-uniform magnetic fields easily exceeding 1 nT near the surface. Ideally, future experiments will use non-metallic electrodes and in general the use of non-metallic materials.

The geometric phase effect (Commins, 1991; Lamoreaux and Golub, 2005; Pendlebury *et al.*, 2004b) is the extra phase accumulated by a quantum system due to the rotation of the quantization axis, in this case due to the combination of motional fields and gradients of the magnetic field. To illustrate the origin of this effect, following Pendlebury *et al.* (2004b), consider the situation shown in Fig. 23 for a particle moving in a nearly circular trajectory near the wall of the radius R chamber with an axial magnetic field \vec{B}_0 nominally directed out of the page ($\vec{B}_0 \approx B_z \hat{z}$) and a magnetic field gradient, which produces radial components. With $\vec{E} \times \vec{v} = -E_z v_\phi \hat{\rho}$, and assuming cylindrical symmetry

$$B_\rho = -\frac{\partial B_z}{\partial z} \frac{R}{2} - \frac{v_\phi E_z}{c^2}, \quad (90)$$

where the azimuthal velocity component v_ϕ is positive for counter-clockwise and negative for clockwise rotation. Note that B_ρ changes magnitude when v_ϕ changes sign. In the frame of the particle, the radial component of the net magnetic field is *rotating* at a frequency $\omega_{Rot} = v_\phi/R$ and causes a shift of the Larmor frequency analogous to the Bloch-Siegert shift of NMR as generalized by Ramsey (Ramsey, 1955).

$$\Delta\omega = \omega_L - \omega_0 = \sqrt{(\omega_0 - \omega_{Rot})^2 + \omega_\rho^2} - (\omega_0 - \omega_{Rot}), \quad (91)$$

where $\omega_\rho = \gamma B_\rho$, with γ the particle's gyromagnetic ra-

tio. For $\omega_\rho^2 \gg (\omega_0 - \omega_{Rot})^2$ and $\omega_0 > \omega_{Rot}$

$$\Delta\omega \approx \frac{\omega_\rho^2}{2(\omega_0 - \omega_{Rot})}, \quad (92)$$

To first order, the shift for positive v_ϕ is

$$\Delta\omega_{v_\phi} = \frac{(\gamma B_\rho)^2}{2(\gamma B_0 - v_\phi/R)}, \quad (93)$$

where γ is the particle's gyromagnetic ratio (rad s $^{-1}$ T $^{-1}$). Because B_ρ changes magnitude when v_ϕ changes sign, this shift does not average to zero for the two signs of v_ϕ . Combining eqs. 90 and 93 the average shift for a positive and negative v_ϕ and a trajectory of radius R is

$$\Delta\omega_{avg} = \frac{1}{2} \frac{\gamma B_z [(\gamma \frac{\partial B_z}{\partial z} \frac{R}{2})^2 + (\gamma v_\phi E_z / c^2)^2] + \gamma^2 \frac{\partial B_z}{\partial z} v_\phi^2 E_z / c^2}{(\gamma B_z)^2 - (v_\phi/R)^2}. \quad (94)$$

When E_z is reversed, the last term in the numerator changes sign, producing a false-EDM signal

$$d_{false}^{GP} \approx \frac{\hbar \gamma^2 \frac{\partial B_z}{\partial z} v_\phi^2 R^2 / c^2}{4(v_L^2 - v_\phi^2)}, \quad (95)$$

where the ‘‘Larmor’’ velocity is $v_L = R\gamma B_z$, the size of the trajectory is R , and the effective velocity v_ϕ . Note that the false EDM in Eq. 95 the denominator apparently goes to zero as $v_\phi \rightarrow v_L$, which has led to characterization of an *adiabatic* regime with $|v_L| \gg |v_\phi|$ and a non-adiabatic regime, e.g. when $|v_L| \approx |v_\phi|$. In the adiabatic regime, the spins track the magnetic field in their frame. As a numerical example a gradient of 0.3 nT/m averaged over the volume of a UCN storage chamber with radius = 0.23 m and height = 0.12 m; the effective transverse velocity is $v_\phi \lesssim 8$ m/s for UCN and $v_\phi \approx 200$ m/s for room-temperature ^{199}Hg whereas $v_L \approx 200$ m/s and ≈ 50 m/s, respectively. For the neutrons, this results in $d_{false-GP} \approx 1 \times 10^{-28}$ e-cm, whereas for ^{199}Hg , $d_{false-GP} \approx 1 \times 10^{-26}$ e-cm. Consequently the geometric phase effect is actually much more significant for the ^{199}Hg comagnetometer (Baker *et al.*, 2006).

Reducing the magnetic-field gradients, affecting the effective velocity and radius of the trajectories, for example with diffusion in a buffer gas, which changes the mean-free path, and making the chamber smaller are all approaches considered to reduce the geometric-phase effect for future experiments. The residual field gradient in the TUMünchen magnetic shield of < 100 pT/m is sufficiently small to suppress geometric phases of the neutron EDM measurement to 1×10^{-28} e-cm. In fact any magnetic distortions or fields inside the chamber also contribute to a gradient in the chamber. In particular, dipole sources that originate from elements of the apparatus such as the doors and valves through which the UCN and ^{199}Hg enter the apparatus as well as magnetic contamination of the surface or magnetization of electrodes

that occur due to HV discharges. A magnetic dipole on the surface with a field of 10 pT at 2 cm distance from the surface (inside the chamber) is estimated to produce a false EDM signal of 10^{-28} e-cm. A thorough treatment of dipole-like contaminations and their effect on the geometric phase can be found in (Golub *et al.*, 2015; Lamoreaux and Golub, 2005; Pendlebury *et al.*, 2004a; Pignol and Roccia, 2012; Steyerl *et al.*, 2013, 2014). This also represents a significant challenge to the design of next-generation experiments.

More refined modeling (Golub *et al.*, 2015; Pignol and Roccia, 2012) as well as numerical studies (Bales *et al.*, 2016) result in similar estimates of this effect for more realistic trajectories and field maps. Recently, a new class of systematic effects previously unknown in spin physics has been discovered, which is based on non-equilibrium spin transport in a non-dissipative system (Bales *et al.*, 2016). This results in deviations from Gaussian distribution of spins' accumulated phase, which are best modeled with so-called Tsallis distributions (Bales *et al.*, 2016). Effects on the distribution as well as shifts that would arise from skewness of the distribution may modify the accuracy of systematic effects estimated in next-generation EDM and other spin-precession experiments, *e.g.* the muon $g - 2$ measurements (Nouri *et al.*, 2016).

The false EDM signal due to the geometric-phase effect depends on the magnetic field gradient and could be canceled, to first order, by an applied gradient $\partial B_z / \partial z|_{\text{appl}}$. A measure of the applied gradient took advantage of the fact that due to gravity, the UCN's settled in the bottle, whereas the distribution of the room-temperature Hg was essentially unaffected. Consequently the center of mass of the UCN is about 2.8 mm lower than the Hg. A pair of frequency measurements with \vec{E} and \vec{B} oriented parallel and antiparallel can be combined into the E_z -odd EDM signal and E_z even signal. For the applied magnetic field $B_z > 0$ ("B up") and taking the frequencies to be positive quantities,

$$d_n^{\text{meas}} = \frac{\hbar}{4|E_z|} [(\omega_n^{\uparrow\uparrow} - \omega_n^{\downarrow\uparrow}) - (\omega_{\text{Hg}}^{\uparrow\uparrow} - \omega_{\text{Hg}}^{\downarrow\uparrow})] \frac{\gamma_n}{\gamma_{\text{Hg}}} \approx d_n + d_{\text{Hg}}^{GP} + \dots, \quad (96)$$

where d_{Hg}^{GP} , given for the schematic model in eq. 95, is linear in $\frac{\partial B_z}{\partial z}$, and the $+\dots$ indicates additional E_z -odd false-EDM effects. The useful E_z -even combination is

$$R_a = \left| \frac{\omega_n^{\uparrow\uparrow} + \omega_n^{\downarrow\uparrow}}{\omega_{\text{Hg}}^{\uparrow\uparrow} + \omega_{\text{Hg}}^{\downarrow\uparrow}} \right| \frac{\gamma_{\text{Hg}}}{\gamma_n} = \frac{B_z + \frac{\partial B_z}{\partial z} \langle z_n \rangle}{B_z + \frac{\partial B_z}{\partial z} \langle z_{\text{Hg}} \rangle}. \quad (97)$$

Taking $\langle z_{\text{Hg}} \rangle = 0$ as the definition of B_z ,

$$R' = R_a - 1 \approx \frac{1}{B_z} \frac{\partial B_z}{\partial z} (\langle z_n \rangle - \langle z_{\text{Hg}} \rangle). \quad (98)$$

Here B_z is positive or negative for up and down orientations, respectively, and $\langle z_n \rangle < 0$. Combining eqs. 95, 96,

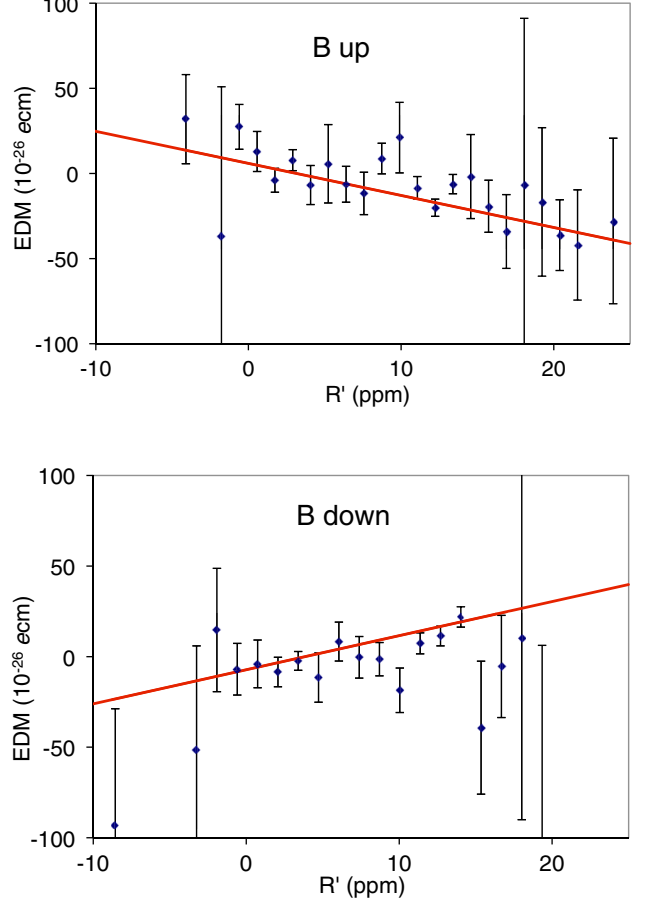


FIG. 22 (Color online) Dependence of the E_z -odd measured EDM signal, labeled “EDM” in the figure and d_n^{meas} in the text, on $R_a - 1$ for two B_z orientations. The data points with error bars are from a typical data run. The solid red lines are linear fits to the entire data set with the same slope for B -up and B -down, but different intercepts. Figure from Baker *et al.* (2006).

and 97, d_n^{meas}

$$d_n^{\text{meas}} = d_n^{\pm} \pm kR', \quad (99)$$

where the $d_n + d_n^{\pm}$ is the y-intercept for B_z and B_z down, respectively and k is the slope, assumed to have the same magnitude for B_z up and down. In Fig. 22, d_n^{meas} is plotted vs R' for B_z positive and negative. These data were fit to determine d_n^+ , d_n^- , and k . The final rEDM result found from crossing point $(d_n^+ + d_n^-)/2 =$ corrected for additional systematic errors most importantly due to a permanent dipole close to the stored UCNs, Earth's rotation and quadrupole fields was

$$(0.12 \pm 1.82) \times 10^{-26} \text{ e-cm}. \quad (100)$$

Another crucial systematic effect for the ^{199}Hg comagnetometer is the light shift, a modification of the atom

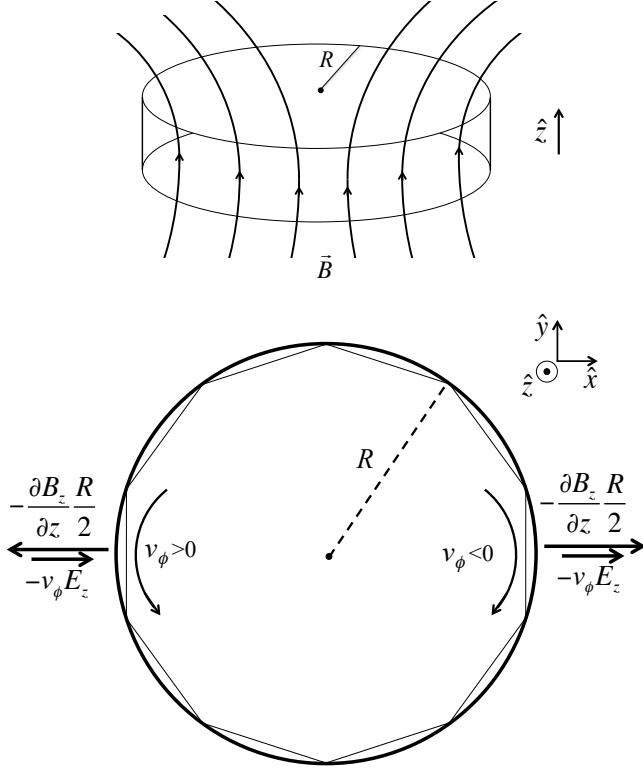


FIG. 23 Top: a non-uniform magnetic field that leads to radial magnetic field components in the upper part of the chamber. Bottom: Illustration of the a particle trajectories that combine with the motional magnetic field giving rise to the geometric phase effect. The left side shows a positive azimuthal velocity, and the right side shows a negative azimuthal velocity. The average frequency shift for the two counter-propagating trajectories is given by Eq. 95. Adapted from Pendlebury *et al.* (2004b).

Hamiltonian in the presence of the laser beam, which has the effect of and additional magnetic field (Cohen-Tannoudji, 1962). The broad emission line of the discharge lamp used by Baker *et al.* (2006) averages over the light-shift effect, and this effect is significantly reduced, but is of significant relevance for laser-based systems, as discussed in Sec. IV.A. Additionally a non-uniform light-shift can produces an effective magnetic field gradient and contribution to the geometric-phase false EDM estimated to be as large as $3.5 \cdot 10^{-27}$ e-cm. Light-shifts have also been investigated in detail with a laser-based system by Griffith *et al.* (2009) to study future cohabitating magnetometers showing that the effect can be set to exactly zero at a detuning of 8 MHz to the red. Other effects relevant for the neutrons are related to the changing energy distribution of the trapped UCN sample during the Ramsey measurement and the energy dependent probability of loss per collision with the walls and the frequency of wall collisions for different particle velocities.

A thorough reinvestigation of systematic effects for the ILL experiment has recently been reported by Pendlebury *et al.* (2015); however, the understanding of systematic effects was matched with the statistical precision of the experiment and reduction, control of and study of potentially smaller effects will be essential. Moreover the stability of all magnetic fields on the 1-1000 second time scale must be controlled at the level of few fT including magnetic fields due to the leakage currents. The control of systematics thus will have to rely on checks, for example intentionally varying intrinsic systematics. Ideas include a double chamber EDM experiment with a surrounding magnetometer array requiring that the magnetic gradient measured with the double chamber be consistent with the gradient measured with a surrounding (4-pi) magnetometer. An inconsistency can only come from internal magnetization, *e.g.* magnetization caused by a spark of the high voltage. We also anticipate that most future EDM experiments will introduce blind analysis techniques.

Neutron-EDM Prospects

A list of next-generation neutron EDM experiments is presented in Table X. All use UCN and have a similar goal of 10^{-27} - 10^{-28} e-cm sensitivity using a variety of different technical approaches and UCN production, transport and storage mechanisms, which are discussed in Sec. III.D.

The PSI experiment

For the neutron EDM program at the Paul-Scherrer Institute near Zurich a large collaboration will use the UCN source described in Sec. III.D. In a first generation effort, the original Sussex/ILL apparatus was moved and rebuilt with significant improvements to the neutron storage bottle lifetimes, neutron polarization detection, magnetic shielding, Hg comagnetometer and the addition of Cs magnetometers, with a recent run expected to provide a result at the 1×10^{-26} e-cm level. Plans are underway for an improved experiment with a double-EDM chamber that is expected to extend the sensitivity towards 1×10^{-27} e-cm.

The FRM-II/PanEDM experiments The EDM experiment, currently based at the FRM-II reactor (Altarev *et al.*, 2012a) with contributions from UC Berkeley, ILL, LANL, Mainz, MSU, PTB Berlin, RAL, TU München, University of Michigan, and Yale, is shown in Fig. 24. It is a modular concept with UCN confined in two adjacent room-temperature chambers with opposite electric field. Ramsey's technique will be applied to both cells simultaneously, and the EDM phase shift after the observation time τ has the opposite sign in the two chambers. In a later stage, cryogenic chambers with increased electric fields are envisaged. Magnetometry will be effected by ^{199}Hg comagnetometers in both cells and by two ^{199}Hg

Experiment	Source	Cell/medium	Goal (10^{-28} e-cm)
ILL Crystal ILL	cold beam	solid	<100
NIST crystal	cold beam	solid	< 10
PNPI-ILL EDM	Turbine	vacuum	~ 100 (stage 1) < 5 (stage 2)
PSI EDM (Sussex)	sD-2	vacuum	~ 50 (stage 1)
PSI EDM (“n2EDM”)	sD-2	vacuum	< 5 (stage 2)
FRM-II EDM (FRM-II)	sD-2	vacuum	<100 (stage 1)
PanEDM (ILL)	4-He	4-He	< 10 (stage 2)
LANL Room Temp.	sD-2	vacuum	10
JPARC	sD-2	vacuum	< 10
TRIUMF/RNPC EDM	4-He	vacuum	< 10
SNS EDM	4-He	4-He	< 5

TABLE X Ongoing and planned neutron-EDM efforts worldwide (2017) as describe in the text.

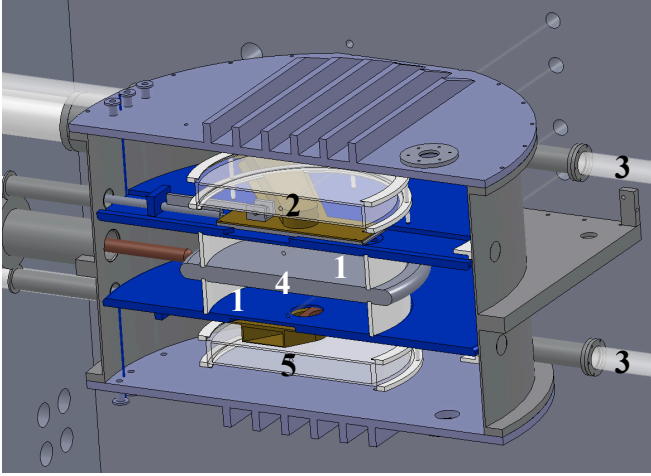


FIG. 24 (Color online) The concept of the EDM experiment based at FRM-II: Item (1) are the cylindrical chambers, where UCN are trapped in vacuum with the chambers at room temperature. The chambers are formed by the high voltage electrode in the center (4), an insulator ring and a ground electrode; (2) and (5) are 199-Hg magnetometer cells; (3) the access channels for additional magnetometers surrounding the EDM chambers (initially an array of 32 Cs sensors).

magnetometers above and below the EDM chambers. In addition an array of Cs atomic-vapor magnetometers is placed near the EDM chambers. The experiment will move for its initial stage to ILL within the PanEDM collaboration (including PNPI) to perform measurements using the SuperSUN UCN source at the former cryo-EDM beam line.

The SNS experiment

A major effort underway in the US is the cryogenic SNS-nEDM experiment with a number of novel features based on the proposal by Golub and Lamoreaux (1994). The plan is to produce UCN in SF-He from a cold neutron beam within the EDM-storage volumes. Cryogenic superconducting shielding and the high dielectric strength of SF-He are expected to provide reduced systematics and higher electric fields than room-temperature vacuum ex-

periments. A small amount of highly polarized ^3He will be introduced into the EDM chambers to serve both as a comagnetometer as well as a measuring device. UCN are captured by ^3He in a spin-singlet state due to an unbound resonance in $n+^3\text{He}$; thus the $n+^3\text{He} \rightarrow ^1\text{H}+^3\text{H}$ reaction is almost completely spin dependent, and the rate of emission of the proton (^1H) and triton (^3H) with a total energy of about 700 keV will measure the projection of the relative spin orientation of the neutron and ^3He . The proton and triton will be detected by scintillation in the SF-He due to the formation and decay of He^* molecules and emission of an 84 nm photon. The UV photons are converted to longer wavelengths for detection by photomultipliers after absorption on the surface coating of DPE (deuterated polyethylene, chosen due to the low loss of UCN on the deuterium). Thus as the UCN and ^3He spins precess during a measurement, the absorption is modulated at the difference of precession rates. The change of modulation frequency of the scintillation light with electric field would signal a difference of the two species' EDMs and, assuming the ^3He atomic EDM is much smaller due to Schiff screening, the neutron EDM. The precession frequency of ^3He is 32.43 MHz/T, compared to bloch MHz/T for the neutron, so any systematic effect (false EDM) due to a change of magnetic field correlated with the electric field is suppressed by a factor of about 10; however it is possible to shift the precession frequencies of both species with an oscillating magnetic field via the Ramsey-Bloch-Siegert effect (Eq. 92), with ω_{Rot} set between the two free-precession frequencies to “dress” the spins (Cohen-Tannoudji and Haroche, 1969). This results in much more sensitive comagnetometry. Alternatively, the ^3He spin-precession can be independently monitored with SQUID sensors to signal any changes in the magnetic field. The geometric phase will affect ^3He , and the mean free path of the ^3He atoms depends on temperature, which is nominally 0.7 K and can be adjusted to scan geometric-phase effects. After a measurement, the depolarized ^3He must be removed from the superfluid helium using a heat-flush/phonon wind technique (Mc-

Clintock *et al.*, 1992).

The TRIUMF/KEK experiment

The TRIUMF/KEK experiment is based on a SF-He source coupled to the high-intensity proton beam from the TRIUMF cyclotron (Masuda *et al.*, 2002). Due to the dilution of UCN when such a source is coupled to the experiment volume, the EDM chamber will be smaller than in other experiments. A further option discussed for this room-temperature neutron EDM experiment is the use of a low-pressure ^{129}Xe -based comagnetometer introduced in Sec. III.B with a proposed two-photon readout (Degenkolb and Chupp, 2011), as well as possibly a ^{199}Hg comagnetometer designed to address the geometric-phase and leakage-current systematic effects. Also, the stability of the magnetometers under breakdowns that may occur in strong electric fields is still being investigated.

EDM experiments at the European Spallation Source

The European Spallation source (ESS), expected to be commissioned in 2019, will provide relatively long pulses of neutrons at high intensity for a proposed fundamental-neutron-physics program (Pignol *et al.*, 2014). UCN source concepts have been developed (Pendlebury and Greene, 2014), including a SF-He concept, which considers focusing a cold-neutron beam from a large axis beam port, which brings cold neutrons into the source with high efficiency. Calculations suggest that 10^3 UCN per cm^{-3} would be delivered to an EDM experiment (Zimmer, 2014b). In a revival of the beam experiments, the pulsed structure of the ESS would provide velocity discrimination and could be used to monitor $\vec{v} \times \vec{E}$ effects with the much greater statistical power provided by the cold-neutron beam (Piegsa, 2014).

Crystal EDM

P-odd/T-odd rotation of the neutron spin in Laue diffraction of polarized neutrons incident on a crystal is sensitive to the neutron EDM interaction with the strong interplanar electric field. The first experiment on CdS was undertaken by Shull and Nathans (1967), who found $d_n = (2.4 \pm 3.9) \times 10^{-22}$ e-cm. Fedorov *et al.* (2011) carried out an experiment at the ILL cold neutron beam facility PF1B measuring the spin-rotation of monochromatic polarized neutrons incident on a quartz crystal. The effective electric field was estimated to be of order 10^8 V/cm. The final neutron spin directions were analyzed for different incident neutron spin to separate the EDM effect from the Mott-Schwinger interaction with atomic electrons in the crystal. The result $d_n = (2.5 \pm 6.5 \text{ (stat)} \pm 5.5 \text{ (sys)}) \times 10^{-24}$ e-cm in about a week of data taking. Prospects for an improved setup suggest that the sensitivity can be improved to 2×10^{-26} e-cm for 100 days of data taking (Fedorov *et al.*, 2011).

B. Paramagnetic atoms: Cs and Tl

The EDM of a paramagnetic system is most sensitive to the electron EDM d_e and a nuclear-spin independent electron-nucleus coupling corresponding to a scalar nuclear current. The tensor nuclear current contribution is several orders of magnitude smaller, and the pseudoscalar contribution vanishes in the limit of zero velocity (*i.e.* infinite nuclear mass).

The first direct atomic EDM experiment - measurement of the frequency shift of the cesium atom EDM in an atomic beam with a modulated electric field - was undertaken by Sandars and Lipworth (1964) and collaborators. There are many challenges to such a measurement that have led to the techniques applied to contemporary undertakings. First, the atomic beam, traveling at several-hundred m/s, transited an apparatus of length less than a meter so that line-widths of several kHz were observed (Ramsey's separated oscillatory field technique was used). Second, due to the unpaired electron, the cesium atom has a large magnetic moment that couples both to external magnetic fields and to the motional magnetic field $\vec{B}_m = \vec{v} \times \vec{E}/c^2$. The magnetic field produced by any leakage currents due to the high voltage would change with the modulation of the electric field and could provide a false-EDM signal. Misalignment of the applied magnetic and electric fields also produces a false signal. By determining the center of a resonance line to a precision less than the line width *i.e.* line splitting by more than 10,000, the frequency shift sensitivity was of order 0.1 Hz, and they obtained the result $d_{\text{Cs}} = (2.2 \pm 0.1) \times 10^{-19}$ e-cm with an electric field up to 60 kV/cm. The error is statistical only, and the finite EDM signal is attributed to the motional effect due to a misalignment of 10 mrad (Sandars and Lipworth, 1964). Subsequent work using other alkali-metal species with lower Z and less sensitivity T-odd/P-odd interactions to monitor magnetic-field effects - now called a comagnetometer - led to the result $d_{\text{Cs}} = (5.1 \pm 4.4) \times 10^{-20}$ e-cm (Carrico, 1968). Shortly after that publication, Weiskopf (1968) and collaborators presented a significantly improved result based on a longer interaction region, correspondingly narrower resonance lines and a sodium comagnetometer: $d_{\text{Cs}} = (0.8 \pm 1.8) \times 10^{-22}$ e-cm.

The cesium-atomic-beam EDM experiments were ultimately limited by the line widths, count-rate limitations, and by systematic errors due to motional magnetic field effects, though the atomic beams machines provided the capability to use other, lighter alkali-metal species, *i.e.* a comagnetometer, significantly reducing the motional-field systematic errors. One approach was to develop and refine atomic or molecular beam experiments in systems with significantly enhanced sensitivity to T-odd/P-odd interactions relative to cesium, *i.e.* a metastable atomic state in xenon, a heavier atom, thallium, used by Commin's group. Molecular beams of polar molecules and

molecular ions is discussed in Sec. IV.C.

Sandar's group performed an atomic beam experiment to search for an electric dipole moment in the 3P_2 metastable state of xenon with a comagnetometer beam of krypton (Player and Sandars, 1970). In the strong applied electric field, the parity-allowed splittings are proportional to $m_J^2 E^2$ and to the magnetic field component along to \vec{E} . The EDM signal would be a splitting linear in \vec{E} ; however transitions that change the magnetic quantum number m_J are not practical due to the sensitivity of the E^2 term to a change of the magnitude of the electric field. Thus the $\Delta|m_J| = 0$ transition $m_J = -1 \rightarrow m_J = +1$ was measured. With the xenon-krypton comparison, the difference of EDMs was found to be $|d_{Xe} - d_{Kr}| = (0.7 \pm 2.2) \times 10^{-22}$ e-cm, where the errors are 90% c.l.

Another approach was the vapor cell experiment developed by Hunter and collaborators (Murthy *et al.*, 1989). The confined atoms provided much narrower resonance line widths, approximately 50 Hz, and also greatly mitigated motional field effects. Though a comagnetometer was not practical in the vapor cell, the leakage currents were directly measured and set the systematic-error uncertainty in the final result

$$d_{Cs} = (-1.8 \pm 6.7_{stat} \pm 1.8_{sys}) \times 10^{-24} \text{ e-cm.} \quad (101)$$

Commins *et al.* (1994) developed a vertical counter propagating thallium atomic beam and subsequently added sodium beams as a comagnetometer (Regan *et al.*, 2002c). These experiments pioneered a new understanding of some of the most important systematic effects affecting EDM experiments including those mitigated by the comagnetometer and the geometric phase effect (Barabanov, 2006; Commins, 1991; Pendlebury, 2004). The most recent result can be interpreted as

$$d_{Tl} = (-4.0 \pm 4.3) \times 10^{-25} \text{ e-cm.} \quad (102)$$

Prospects for alkali-metal atoms

Laser cooling and trapping of the heaviest alkali-metal species cesium and francium offer promising new directions, and several approaches are being pursued. Cesium atomic fountain clocks based on launching atoms from a laser cooled or trapped sample have moved to the forefront of time-keeping. Narrow line widths ($\tau \approx 1$ s) are attained as the atoms move up and then down through a resonance region. While the ^{133}Cs atomic frequency standard uses the $\Delta m_F = 0$ transition, which is insensitive to magnetic fields in first order, an EDM measurement must use $\Delta m_F \geq 1$. From equation 5, with $T = 1$ s, $\tau \gg T$ and $N = 10^6$, the expected uncertainty on ω is expected to be about $\delta_\omega \approx 10^{-3}$ Hz, which is consistent with observations of the Allan variance representing the short-term instability of cesium fountain clocks ($\sigma_\omega/\omega \approx 10^{-13}$ for $\omega = 2\pi \times 9.2$ GHz - (Weyers *et al.*, 2009)). For an EDM measurement with an electric field of 100 kV/cm, which

may be feasible, each 1 second shot would have a sensitivity of 6×10^{-24} e-cm, comparable to the sensitivities of both the cesium and thallium measurements presented in Table I. Thus significant improvement is possible, and a demonstration experiment with about 1000 atoms per shot and $E = 60$ kV/cm was reported as a measurement of d_e by Amini *et al.* (2007). The result can be interpreted as $d_{Cs} = (-0.57 \pm 1.6) \times 10^{-20}$ e-cm (the authors use $\eta_e = 114$ for cesium). The major limitation in this demonstration was the necessity to map out the entire resonance-line shape spectrum, which is the combination of transitions among the nine hyperfine sub-levels and inhomogeneities of the applied magnetic field in the resonance region. This subjected the measurement to slow magnetic field drifts that would be monitored or compensated in the final experiment. If these problems are solved, the statistical sensitivity could be significantly improved with several orders of magnitude more atoms, higher electric field and duty-factor improvements; however the major systematic effect due to $\vec{v} \times \vec{E}$ was about 2×10^{-22} e-cm (Amini *et al.*, 2007). This could ultimately limit the sensitivity of a single species fountain measurement.

For francium, η_{d_e} , the ratio of atomic EDM to electron EDM from equation 65, is in the range 900 to 1200 (Ginges and Flambaum, 2004), and k_{Cs} should be similarly enhanced for francium. Francium can be produced in significant quantities in isotope-separator rare-isotope production facilities, and ^{210}Fr has been produced, laser cooled and trapped in a magneto-optical trap (MOT) (Gomez *et al.*, 2008). The experiment has been moved to the isotope-separator facility (ISAC) at TRIUMF in Vancouver, Canada. Francium isotopes have half lives of 20 minutes (for ^{212}Fr) or less, and any experiment would need to be "on-line," that is the EDM apparatus would be at the site of the rare-isotope production facility. The development of the cesium-fountain EDM measurement may lead the way to a future program with francium at a future facility such as the Facility for Rare Isotope Beams (FRIB) at Michigan State University.

The fountain concept allows line widths on the order of 1 Hz, limited by the time for the cold atoms with vertical velocity of a few m/s to rise and fall about 1 meter. Another idea being pursued by D. Weiss and collaborators is to stop and cool alkali-metal atoms in optical molasses near the apogee of their trajectory and trap them in an optical lattice formed in a build-up cavity (Fang and Weiss, 2009). Storage times in the lattice could be many seconds. The lattice would be loaded with multiple launches, filling sites that extend over 5-10 cm, and 10^8 or more atoms could be used for the EDM measurement. After loading the lattice, the atoms would be optically pumped to maximum polarization and then the population transferred to the $m_F = 0$ state by a series of microwave pulses. A large electric field (*e.g.* 150 kV/cm) would define the quantization axis in nominally zero mag-

netic field, and the energies would be proportional to m_F^2 due to the parity-allowed interaction. In another planned innovation, a Ramsey separated-field approach would be used with the free-precession interval initiated by pulses that transfer atoms to a superposition of $m_F = F$ and $m_F = -F$ states and terminated by a set of pulses coherent with the initial pulses. The relative populations transferred back to the $m_F = 0$ state would be probed by optical fluorescence that could be imaged with about 1 mm spatial resolution (Zhu *et al.*, 2013). With the large size of the lattice, the superposition of stretched levels ($m_F = \pm F$) would amplify the sensitivity by a factor of F relative to experiments that monitor $\Delta m_F = 1$ transitions (Xu and Heinzen, 1999). In a measurement time $\tau = 3$ s, and $N = 2 \times 10^8$, an EDM sensitivity of 6.5×10^{-26} e-cm for the cesium atom is expected. The optical lattice can also trap rubidium, which could be used as a comagnetometer.

Cold atom techniques have been developed over the past 25 years by a large number of groups, and appear to be able to provide statistical power and ways to monitor systematic effects. The continuing advances in technology of fountain clocks provides encouragement, though an EDM measurement provides a set of distinctly separate systematic effects. An EDM measurement in a lattice would allow measurements with two or more species, thus providing a comagnetometer to monitor leakage-current and other effects.

C. Paramagnetic polar molecules: YbF, ThO and HfF⁺

Molecular-beam EDM experiments exploit several features of diatomic, polar molecules with generally one light and one heavy atom, most significantly the strong interatomic electric field with characteristic strength of 10-100 GV/cm. The pioneering molecular-beam EDM approach of (Coveney and Sandars, 1983c) and (Wilkening *et al.*, 1984a) used thallium-fluoride (TlF) which is *diamagnetic* and is discussed in the next section. A number of groups have followed the lead of (Hudson *et al.*, 2002) and investigated paramagnetic molecules, and the most sensitive measurements in paramagnetic systems are from YbF (Hudson *et al.*, 2011), ThO (Baron *et al.*, 2014, 2016) and HfF⁺ (Cairncross *et al.*, 2017). In addition efforts using the molecular ion ThF⁺, which is similar in electronic structure, are underway by Loh *et al.* (2013).

Experimentally, the internal or body-frame electric dipole moment \vec{D} is oriented parallel or antiparallel to a relatively modest applied electric field in the lab $\vec{E}_{lab} = E_{lab}\hat{z}$ - in essence the molecule's electric polarizability is very large resulting in an effective molecular dipole moment $D_z \propto E_{lab}$. In the atomic beam, the average orientation of D_z can be expressed as a polarization $\mathcal{P}_z = D_z/|\vec{D}|$, for example the dependence of \mathcal{P}_z for YbF is shown in Fig. 25. For ThO and HfF⁺, which

are effectively fully electrically polarized by a relatively small laboratory electric field, the estimated effective internal electric fields are $E_{eff} \approx 84$ GV/cm and $E_{eff} \approx 23$ GV/cm, respectively (see Table III).

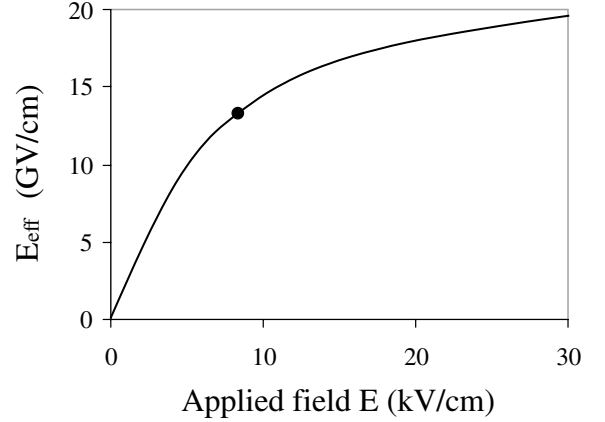


FIG. 25 The effective electric field E_{eff} in YbF as a function of E_{lab} . The fully saturated E_{eff} corresponds to $\mathcal{P}_z = 1$. Figure from Hudson *et al.* (2002).

The electronic energy level structure of a $^3\Sigma_{\Omega} = ^3\Delta_1$, *e.g.* $F = 1$ state in the polar molecule ThO, is shown in Fig. 26. The quantum numbers labels by capital greek letters indicate angular momentum projected on the internuclear axis: ($\Sigma = 3$ indicates the electron-spin triplet state, orbital angular momentum $\Lambda = 2$ is labeled by Δ , and the total of spin and orbital angular momentum and rotation is $\Omega = 1$.) The $^3\Delta_1$ state also results in a relatively small magnetic moment as the spin and orbital moments cancel. As shown, the laboratory electric field electrically polarizes the molecule providing two directions of the internal electric field with different splittings due to the EDM, but the same magnetic field splitting. Thus the two orientations of the molecular dipole, which can be separately probed, for example by tuning a probe laser, provide an effective *internal* comagnetometer.

The YbF experiment used ground-state $^2\Sigma_{1/2}^+$ molecules, where the + indicates positive reflection-symmetry along a plane containing the internuclear axis (Hudson *et al.*, 2002). The resulting P-odd/T-odd frequency shift is reported as

$$\omega^{EDM}(\text{YbF}) = (5.3 \pm 12.6_{stat} \pm 3.3_{syst}) \text{ mrad/s}, \quad (103)$$

which can be interpreted as an electron EDM assuming $E_{eff} = 14.5$ GV/cm and $C_S = 0$:

$$d_e(\text{YbF}) = (-2.4 \pm 5.7_{stat} \pm 1.5_{sys}) \times 10^{-28} \text{ e-cm} \quad (C_S = 0). \quad (104)$$

The setup of the ACME ThO experiment is shown in Fig. 27 The experiment used molecular-beam resonance

methods based on the Ramsey separated-oscillatory-fields technique. For ThO, the $^3\Delta_1$ state is a metastable state originally populated from the ground state by the 943 nm optical pumping light. In this case, $2DE_{lab}/\hbar \approx 100$ MHz, and 1090 nm optical transitions to an excited state with two opposite parity levels separated by 10 MHz are used to prepare and probe the orientations of a superposition of the $m = \pm 1$ levels. If the state-preparation light is polarized along \hat{x} , then the initial electron spin is along \hat{y} . The EDM signal is a rotation around \hat{z} , which is detected by the component of the electron spin along \hat{x} that reverses with the sign of $\vec{E}_{lab} \cdot \vec{B}$. The EDM frequency shift $\Delta\omega^{EDM}$ is the rotation angle divided by the $\tau \approx 1.1$ ms, the transit time from pump to probe positions. (τ is determined from the magnetic precession angle $\phi^B = -\mu|B_z|\tau/\hbar$, where μ is the molecular magnetic moment, which is relatively small due to cancellation of spin and orbital effects.) A number of additional experimental parameters are changed to separate background and false-EDM signals including the molecular orientation ($E_{eff} > 0$ or $E_{eff} < 0$), the magnetic field direction and magnitude, the electric field magnitude, the read-out laser polarization direction and various exaggerated imperfections. In all more than 40 parameters were varied. Systematics were evaluated through a combination of anticipated effects informed by earlier experiments in YbF (Hudson *et al.*, 2011) and PbO (Eckel *et al.*, 2013). The dominant systematic effects are generally the combi-

nation of two small effects, *e.g.* the AC stark shift caused by detuning of the pump and probe lasers along with misalignments, gradients of the circular polarization and imperfect reversal of the electric field. The final result of the first-generation ThO experiment is a P-odd/T-odd precession frequency

$$\omega^{EDM}(\text{ThO}) = (2.6 \pm 4.8_{stat} \pm 3.2_{syst}) \text{ mrad/s.} \quad (105)$$

From Eq. 66, these can be interpreted as the combination of contributions from the electron EDM d_e and from a nuclear-spin independent (scalar) coupling labeled C_S ; however adopting the “sole-source” approach (see Sec. I.B, this can be interpreted as

$$\begin{aligned} d_e(\text{ThO}) &= (-2.1 \pm 4.5) \times 10^{-29} \text{ e-cm} \quad (C_S = 0), \\ C_S(\text{ThO}) &= (-1.3 \pm 3.0) \times 10^{-9} \quad (d_e = 0). \end{aligned} \quad (106)$$

Further interpretation is provided in Sec. V. This is considered a “first-generation” ThO effort by the experimenters, and upgrades to cold molecular beam promise improved statistical uncertainty.

For $^{180}\text{Hf}^{19}\text{F}^+$, paramagnetic molecular ions in the metastable $^3\Delta_1$, $F = 3/2$ state have been confined in a radio frequency trap to measure the P-odd/T-odd energy shifts (Cairncross *et al.*, 2017). In this case, the effective electric field for a fully electrically polarized molecule in the lab frame was $|E_{eff}| \approx 23$ GV/cm (Fleig and Nayak, 2013; Petrov *et al.*, 2007; Skripnikov, 2017) and $\alpha_{C_S} \approx 2.0 \times 10^6$ rad/s (Skripnikov, 2017). It has also been pointed out that an experiment with the ^{177}Hf (18.6%) with nuclear spin $I = 7/2$ would be sensitive to the P-odd/T-odd. magnetic-quadrupole moment (Skripnikov *et al.*, 2017). The molecular ions were produced by laser ablation of Hf metal in a supersonic jet with a mixture of argon and SF₆ gas, which produced neutral ground state HfF molecules. The cold argon gas from the supersonic jet cooled the rotational and vibrational degrees of freedom of the molecules. UV lasers ionized the HfF, and the ions were initially trapped by an axial static field and a 50 kHz radial (quadrupole) field and then confined by a uniform electric field that rotates at 250kHz. The result was that the ions rotated in a circle of about 1 mm diameter. An axial magnetic field gradient created the bias field in the rest frame of the ions. The Ramsey-style EDM measurement consisted of preparation of a polarized spin state with lasers followed by a $\pi/2$ pulse, which created a superposition of $m_F = \pm 3/2$, a free precession time of about 700 ms, and a second $\pi/2$ pulse. The final phase was read out by selective laser depopulations of alternating $m_F = \pm 3/2$ levels followed by laser ionization and detection of the Hf⁺ and background ions by a microchannel plate. Systematic effects are studied by observing frequency shifts in channels that are not sensitive to the P-odd/T-odd effects. The important systematic effects included non-ideal reversal of the

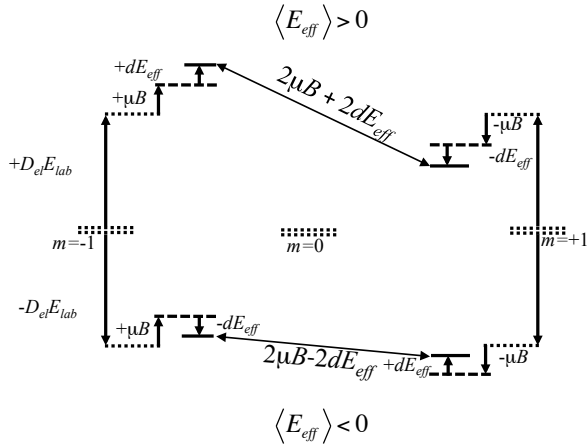


FIG. 26 Level structure of molecule in a $^3\Delta_1$, $J = 1$ state. The laboratory electric field E_{lab} splits the states by $\pm D_{el} E_{lab}$ into molecular dipole up and down. This results in the two orientations of the effective internal field E_{eff} , which is directed towards the lighter atom. The specific structure for the ThO experiment is shown; for HfF^+ $J = 3/2$ and the stretched states ($m = \pm 3/2$) move up and down similarly. In a magnetic field \vec{B} parallel or antiparallel to \vec{E}_{lab} , the $m = \pm 1$ states are further split by μB as shown. The EDM d further splits the $m = \pm 1$ states with $E_{eff} > 0$, but reduces the splitting with $E_{eff} < 0$ antiparallel to B .

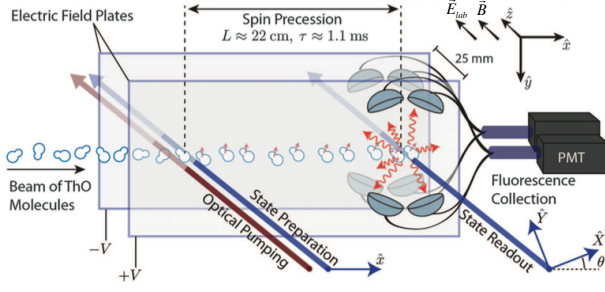


FIG. 27 (Color online) The experimental layout of the ACME ThO experiment from Baron *et al.* (2014).

rotating magnetic field combined with the different gyromagnetic ratios of the upper (labeled $E_{eff} > 0$) and lower (labeled $E_{eff} < 0$) pairs of states (doublets) due to Stark mixing with $J = 2$ states, geometric phases, and background. The difference of frequencies for two flips that project the EDM—flipping the bias magnetic field and flipping E_{eff} by selecting the upper to lower pair of states—was reported:

$$\omega^{BD}(\text{HfF}^+) = 2\pi(0.1 \pm 0.87_{stat} \pm 0.2_{syst}) \text{ mrad/s.} \quad (107)$$

Assuming $C_S = 0$, the resulting sole-source electron EDM is

$$d_e(\text{HfF}^+) = (0.9 \pm 7.7_{stat} \pm 1.7_{syst}) \times 10^{-29} \text{ e-cm,} \quad (108)$$

for $E_{eff} = 23 \text{ GV/cm}$. A second generation ion trap that may confine ten-times more HfF^+ ions in a larger volume combined with improved electrode design is expected to provide an order of magnitude higher sensitivity (Cairncross *et al.*, 2017). The JILA group also intends to perform an experiment on ThF^+ ($E_{eff} \approx 36 \text{ GV/cm}$), for which the ground state is $^3\Delta_1$ providing for coherence times that are not limited by the lifetime of an excited state.

An analysis of the paramagnetic molecule experimental results that accounts for d_e and C_S simultaneously is presented in Sec. V.

Another promising idea is to store paramagnetic molecular ions or other particles in an electrostatic storage ring of few meters diameter, used as a large ion trap⁸. Such a configuration enables the storage of molecular ions of all possible configurations of states. In TaO , for example, the ground state structure is $^2\Lambda_{\Omega} = ^3\Delta_1$, and ions could be trapped electrostatically for several hours in

bunches of up to 10^7 ions with kinetic energies of the order 100 keV. Preparation and readout of the molecular states relevant for EDM measurements would be done with lasers. Due to the angular frequency of the particles of less than kHz the small molecular magnetic dipole moment and the eddy-current (and RF) shielded environment provided by the vacuum housing of the storage ring, no compensation of the ambient magnetic fields is necessary. The long storage times in the ring allow for a large number or repetitions of the experiment for each configuration and the large number of ions stored in the ring potentially enables a significant enhancement of the sensitivity for eEDM and possibly achieve a significantly enhanced sensitivity to the electron-EDM of up to six orders of magnitude. At this level, EDMs and Majorana Neutrinos have model dependent connections, thus enabling a new path to access physics beyond the SM (Archambault *et al.*, 2004; Ng and Ng, 1996b). Additionally radium or radon ions could be stored, taking advantage of the octupole enhanced Schiff moment or nuclear EDM discussed below.

D. Solid-state systems

The electron EDM can also be measured in special ferro-electric and paramagnetic solid-state systems with quasi-free electron spins that can be subjected to applied electric and magnetic fields. Advantages of such a system are

- i. a high number density of unpaired electrons (10^{22} cm^{-3} providing signal amplification;
- ii. confinement of the electrons mitigating such effects as motional fields;
- iii. features of solid-state samples including collective effects, *e.g.* for ferro-electric systems, a large electric field spin-polarizes the electrons resulting in a magnetization that reverses with the electric field;
- iv. minimal magnetic order to mitigate spurious magnetic effects.

A cryogenic experiment increases the electron polarization and provides for detection of the resulting magnetization by SQUID magnetometers. Desired properties of an ideal material follows from the specific requirements of the EDM search (Buhmann, 2002; Liu and Lamoreaux, 2004; Shapiro, 1968; Sushkov *et al.*, 2009, 2010).

The polycrystal $\text{Gd}_3\text{Ga}_5\text{O}_{12}$ (gadolinium-gallium-garnet) provides seven unpaired atomic electrons, low conductivity ($10^{14} \Omega\text{-m}$) and high dielectric strength (1 GV/m). Enhancement of the electron EDM leads to an atomic EDM of Gd^{3+} atoms in the lattice $d_{\text{Gd}^{3+}} \approx 20d_e$, and the result $d_e = (-5.57 \pm 7.98_{stat} \pm 0.12_{syst}) \times 10^{-25} \text{ e-cm}$ was reached with 5 days of data averaging (Kim *et al.*,

⁸ A ring with in principle suitable parameters exists (von Hahn *et al.*, 2016).

2015). An experiment in the paramagnetic ferroelectric $\text{Eu}_{0.5}\text{Ba}_{0.5}\text{TiO}_3$ measured $d_e = (-1.07 \pm 3.06_{\text{stat}} \pm 1.74_{\text{sys}}) \times 10^{-25}$ e-cm. (Eckel *et al.*, 2012). Though this result is several orders of magnitude short of the sensitivity of paramagnetic molecules, improvements to magnetic noise and shielding can improve sensitivity. Other materials under consideration include SrTiO_3 doped with Eu^{2+} (Müller and Burkard, 1979; Viana *et al.*, 1994). Another approach in paramagnetic ferroelectrics, would detect the electric field produced by the electron EDMs aligned with the magnetically polarized spins (Heidenreich *et al.*, 2005).

E. Diamagnetic Atoms and molecules

Diamagnetic atoms have the experimentally attractive feature that they can be contained in room-temperature cells because the angular momentum of the atom, which resides in the nucleus, is well shielded by the closed electron shell, even as the atom sticks to the wall for short times. Diamagnetic atoms can also be spin polarized using optical-pumping techniques, providing the largest possible signal-to-noise ratios and optimal statistical precision. Combined with techniques to carefully monitor and control systematic effects, measurements with ^{129}Xe (Vold, 1984), with $^{129}\text{Xe}/^3\text{He}$ (Rosenberry, 2001) and the series of measurements with ^{199}Hg (Graner *et al.*, 2016; Griffith *et al.*, 2009; Romalis *et al.*, 2001) are the most sensitive EDM measurements to date. The most recent ^{199}Hg result stands alone in its sensitivity to various sources of CP violation (Graner *et al.*, 2016)

As discussed in Sec. II.F and in Eq. 67, the dominant contributions to the atomic EDM in diamagnetic atoms is the Schiff moment of the nucleus and the nuclear-spin-dependent electron-nucleus force with coefficient $C_T^{(0)}$. The Schiff moment itself can arise from T-odd/P-odd NN interactions and from the EDMs of the individual nucleons (both ^{129}Xe and ^{199}Hg have an unpaired neutron); however these sources can be related, depending on the nature of the P-odd/T-odd interactions.

Xenon

Xenon is the heaviest stable noble gas, and ^{129}Xe is a spin-1/2 isotope. Spin 1/2 atoms in cells have the advantages that only magnetic dipole interactions with external fields, with other atoms and with the cell walls are allowed. This leads to longer spin-coherence times and narrow line widths compared to nuclear spin greater than 1/2, which is subject, for example, to electric quadrupole interactions in particular with the cell walls (Chupp, 1990; Wu, 1990). Spin relaxation times of several 100's of seconds and longer are observed for free-induction decay. In natural xenon, the abundance of ^{129}Xe is 26%; however isotopically enriched gas is available. Polarization of ^{129}Xe greater than 10% is possible using spin-exchange, mediated by the hyperfine interaction, with

laser-optically-pumped alkali-metal vapor (Zeng, 1985). This also makes it possible to monitor the free-precession of ^{129}Xe polarization, which weakly polarizes the alkali-metal vapor.

The first EDM measurement in ^{129}Xe by Fortson and collaborators (Vold, 1984) used spin exchange with laser-optically-pumped rubidium to polarize ^{129}Xe in a stack of three cylindrical cells with electric fields of magnitude 3.2 to 4.9 kV/cm applied parallel and antiparallel to a uniform and well shielded 10 μT magnetic field. The stack of cells, treated as magnetometers, allows sums and differences of the free-precession frequencies to be used to determine the average magnetic field, and the average magnetic field gradient. A third combination of the three frequencies is the EDM signal. The magnitude of the applied electric field is notably much lower than in the atomic/molecular beam and neutron EDM experiments due to the compactness of the cells, the materials and the buffer gas. One potential systematic error for such a system was the effective magnetic field, due to the hyperfine interaction, caused by any rubidium polarization projection along the electric field axis that somehow changed when the electric fields were changed. One successful approach was to “quench” the polarization of the two rubidium isotopes with resonance RF magnetic fields (Oteiza, 1992). Another concern was any change in the leakage currents that flowed across the cells due to the applied voltages that was different for different cells. Both of the effects were studied and found to be small compared to the statistical error of the measurement. The EDM of ^{129}Xe was measured to be $d_{\text{Xe}} = (-0.3 \pm 1.1) \times 10^{-26}$ e-cm, where the error is statistical only.

Another approach to measure the ^{129}Xe EDM used spin-exchange pumped noble-gas masers of ^{129}Xe and ^3He (Bear, 1998; Chupp, 1994; Stoner, 1996). Spin-exchange optical pumping is practical, in principle, for any odd A noble gas, and a population inversion can be pumped in multiple species with the same sign of the magnetic moment. The two species have very different sensitivity to the Schiff moment and to other P-odd/T-odd interactions, which are approximately proportional to Z^2 , but similar sensitivity to magnetic field effects, particularly those produced by leakage currents that can change when the electric field is changed. Thus the ^3He served as a comagnetometer occupying nearly the same volume as the ^{129}Xe in a single measurement cell. The result

$$d(^{129}\text{Xe}) = (0.7 \pm 3.3 \pm 0.1) \times 10^{-27} \text{ e-cm}, \quad (109)$$

Several experimental efforts to improve the ^{129}Xe EDM sensitivity by 2-3 orders of magnitude are underway including the active maser (Yoshimi *et al.*, 2002), highly polarized liquid ^{129}Xe detected with SQUID magnetometers (Ledbetter *et al.*, 2012) and gas-phase experiments with ^3He comagnetometry and SQUID-magnetometer detection (Heil *et al.*, 2013; Kuchler *et al.*, 2014). The

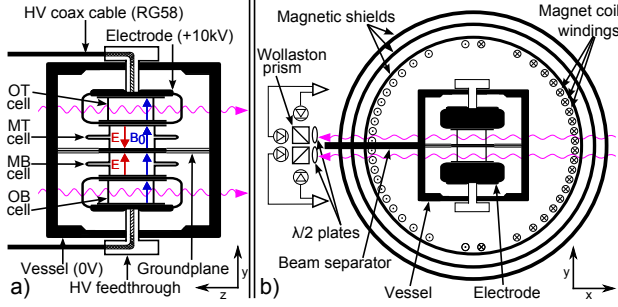


FIG. 28 (Color online) The experimental layout of the Seattle ^{199}Hg experiment from Graner *et al.* (2016).

SQUID-magnetometer experiments have demonstrated signal and noise that suggest one to three orders of magnitude improvement in sensitivity to the ^{129}Xe EDM is possible in the near future.

Mercury

The ^{199}Hg experiments undertaken by Fortson's group built on the ideas used in their ^{129}Xe buffer-gas cell experiment (Vold, 1984); however there are two crucial differences with mercury: it is more chemically reactive resulting in shorter coherence times, and it is heavier and thus generally more sensitive to sources of T and P violation. The most recent experiment (Graner *et al.*, 2016) used a stack of four cells sealed with sulfur-free Lesker KL-5 vacuum sealant and directly pumped and probed the ^{199}Hg with a 254 nm laser (Harber, 2000) as illustrated in Fig. 28. The outer two of the four cells have no electric field and the inner two have electric fields in opposite directions so that a difference of the free-precession frequencies for the two inner cells is an EDM signal. An EDM-like difference of the outer cell frequencies was attributed to spurious effects such as non-uniform leakage currents correlated with the electric field reversals and were therefore scaled and subtracted from the inner-cell frequency difference to determine the EDM frequency shift. The magnitudes of the leakage currents were also monitored directly and used to set a maximum E-field correlated frequency shift that contributed to the systematic-error estimate. Other systematic-error sources explored were effects of high-voltage sparks on the EDM signals and a number of possible correlations of experimentally monitored parameters (*e.g.* laser power and magnetic field fluctuations outside the magnetic shields). There were no apparent correlations, and the leakage current (± 0.5 pA) was so small that only upper limits on the systematic errors could be estimated. The most recent result is

$$d(^{199}\text{Hg}) = (0.49 \pm 1.29 \pm 0.76) \times 10^{-29} e\text{-cm}. \quad (110)$$

TlF

Molecular beam experiments using TlF were pursued

by Sandars (Harrison, 1969; Hinds, 1980), by Ramsey (Wilkening *et al.*, 1984b) and by Hinds (Cho, 1991; Schropp, 1987). For molecular beams, the systematic errors associated with the $\vec{v} \times \vec{E}$ and leakage current effects are mitigated by using a relatively small applied electric field to align the intermolecular axis as is the case with polar molecules discussed in IV.C. This results in a large internal electric field at the thallium nucleus (Coveney and Sandars, 1983b). The experiment is set up to detect an alignment of a spin or angular momentum along the electric field by detecting precession around the internuclear axis, *i.e.* the frequency shift when the relative orientation of applied electric field and magnetic fields are reversed. When the averaged projection of the thallium nuclear spin on the internuclear axis is taken into account ($\langle \cos \theta_{\sigma\lambda} \rangle = 0.524$), a frequency shift for full electric polarization is determined to be $d = (-0.13 \pm 0.22) \times 10^{-3}$ Hz. With the applied electric field of 29.5 kV/cm, this is interpreted as a permanent dipole moment of the thallium molecule of

$$d_{\text{TlF}} = (-1.7 \pm 2.9) \times 10^{-23} e \text{ cm}. \quad (111)$$

For TlF, the electron spins form a singlet, but both stable isotopes of thallium (^{203}Tl and ^{205}Tl) have nuclear spin $J^\pi = 1/2^+$, and the dipole distribution in the nucleus would be aligned with the spin through T and P violation. This gives rise to the Schiff moment. An alternative (and the original) interpretation is based on the observation that in the odd-A thallium isotopes, one proton remains unpaired and can induce the molecular EDM through both the resulting Schiff moment and through magnetic interactions (Coveney and Sandars, 1983b). Separating these, the proton EDM would produce a magnetic contribution to a molecular EDM of $d_{\text{TlF}}^{p\text{-mag}} = 0.13 d_p$, and a contribution to the Schiff moment that would produce a molecular EDM estimated to be $d_{\text{TlF}}^{p\text{-vol}} = 0.46 d_p$. The TlF molecular EDM can also arise from the electron EDM and from P- and T-violating scalar and tensor electron-hadron interactions; however paramagnetic systems are more sensitive to $C_S^{(0,1)}$ and diamagnetic systems such as TlF are more sensitive to $C_T^{(0,1)}$. Thus this measurement could be interpreted as a (model dependent) measurement of the proton EDM: $d_p = (-3.7 \pm 6.3) \times 10^{-23} e\text{-cm}$.

F. Octupole collectivity in diamagnetic systems

Recently experimental efforts have focused on exploiting the enhanced Schiff moment in isotopes with strong nuclear octupole collectivity. This is expected to arise when neutrons and protons near the Fermi surface populate states of opposite parity separated by total angular momentum $3\hbar$, which corresponds to proton and neutron numbers in the range Z or $N \approx 34, 56, 88$ and $N \approx 134$.

Such systems have reflection asymmetric states, which can lead to permanent octupole deformation or octupole vibration. In either case a large intrinsic dipole moment analogous to polar molecules (see Sec. IV.C) is polarized along the nuclear-spin by P-odd/T-odd interactions. This leads to the nuclear Schiff moment which is further enhanced by the electric polarizability of the nucleus (also analogous to the polar-molecules). In the two-state approximation, the resulting Schiff moment can be parameterized as

$$S \propto \eta e \frac{\beta_2 \beta_3^2 Z A^{2/3} r_0^3}{E_+ - E_-}, \quad (112)$$

where η represents the strength of the P-odd/T-odd interaction, β_2 and β_3 are the quadrupole and octupole deformation parameters and E_{\pm} are the energies of the opposite-parity states (Auerbach *et al.*, 1996; Haxton and Henley, 1983; Spevak and Auerbach, 1995; Spevak *et al.*, 1997b). Note that the octupole deformation parameter enters S quadratically, which means that both octupole vibrations and permanent deformation are equally effective (Zelevinsky *et al.*, 2008), though permanent deformation is indicative of (and indicated by) closely spaced parity doublets: $(E_+ - E_-) \approx 50\text{-}100$ keV. In ^{229}Pa , the splitting was originally reported to be as small as 0.22 keV (Ahmad *et al.*, 1982), and evidence of strong octupole correlations support a ground-state parity doublet with $I = 5/2$ (Ahmad *et al.*, 2015), which was also predicted theoretically by Chasman (1980). In fact the evidence of the closely-spaced doublet in ^{229}Pa provided motivation for the initial suggestion of octupole-enhanced Schiff moments by Haxton and Henley (1983).

There is strong evidence of octupole collectivity for nuclei with $A \approx 200 - 226$, including interleaved even/odd parity states in even- A nuclei (Cocks *et al.*, 1999), parity doublets in odd- A nuclei (Dahlinger *et al.*, 1988) and enhanced electric-dipole (E1) transition moments (Butler and Nazarewicz, 1991). The strongest direct evidence for octupole collectivity has come from recent measurement of E3 strength using Coulomb excitation of radioactive beams of ^{220}Rn and ^{224}Ra at ISOLDE (Gaffney *et al.*, 2013). The β_2 and β_3 for ^{220}Rn and ^{224}Ra are quite similar; however the larger moment Q_3 in $^{224/226}\text{Ra}$ compared to ^{220}Rn suggests that the deformation is permanent in ^{224}Ra , while ^{220}Rn is a vibrator (Gaffney *et al.*, 2013). On the other hand, a calculation by Dobaczewski (2015) indicates that ^{223}Rn may be permanently deformed.

An intriguing possibility for future experimental efforts is to use a molecule with an octupole-enhanced nucleus, for example ^{225}RaO (Flambaum, 2008). Though experimentally very challenging and potentially limited by production of appropriate molecules, this would take advantage of both the possible octupole-enhanced Schiff moment and the very large internal electric fields in the molecule.

²²⁵Ra An ongoing effort at Argonne National Lab uses

cold-atom techniques to measure the EDM of the ^{225}Ra atom (Bishof *et al.*, 2016; Parker *et al.*, 2015), which may have 2-3 orders of magnitude greater sensitivity to the P-odd/T-odd pion-nucleon couplings than ^{199}Hg based on atomic (Dzuba *et al.*, 2002) and nuclear physics calculations (Auerbach *et al.*, 1996; Engel *et al.*, 2000; de Jesus and Engel, 2005; Spevak *et al.*, 1997b).

The apparatus is shown in Fig. 29, and the atomic level structure of radium is shown in Fig. 30. The key components of the apparatus were the radium source, the Zeeman slower loading the magneto-optical trap (MOT) and the optical-dipole trap (ODT). The radium was provided by sources of up to 9 mCi, which provide both ^{225}Ra ($t_{1/2}=14$ d) and significantly greater quantities of ^{226}Ra ($t_{1/2}=1600$ y), which has no spin or EDM, but which is useful for diagnostics and tuning the optical traps. The Zeeman slower used the momentum transferred from photons in a counter-propagating laser beam which was kept close to the 714 nm intercombination-line resonance by the Zeeman shift in a spatially-varying magnetic field. The slowed atoms then entered the MOT operating on the same transition. Atoms that leak to the $7s6d^3\ ^3D_1$ level were repumped to the ground state with a 1429 nm laser. The trapping efficiency of the MOT was approximately 10^{-6} , largely limited by the lower scattering rate. Radium atoms were accumulated for about 40 s and cooled to ≈ 40 μK with typically 10^5 ^{226}Ra atoms or 10^3 ^{225}Ra atoms trapped in the MOT. From the MOT, atoms were transferred with high efficiency (80%) to the ODT, effected by a 40 W, 1550 nm, laser beam focused with an $f = 2$ m lens. By translating the lens, the ODT-trapped atoms were moved one meter into a separate chamber within a cylindrical-multilayer magnetic shield, where a standing-wave 1550 nm ODT held the atoms for the EDM measurement. The ODT holding time-constant of ≈ 40 s was limited by collisions with residual gas atoms. A pair of copper electrodes separated by 2.3 mm provide an electric field of 67 kV/cm.

The EDM measurement was based on a 100 second cycle consisting of 60 seconds to cool, trap and transfer the atoms into the ODT and two approximately 20 second free precession periods to extract the EDM signal. The Ramsey separated-oscillatory-field measurement consisted of state preparation with a circularly polarized laser beam (483 nm) followed by a nuclear-spin precession period of $(20 + \delta)$ seconds and measurement of atoms of the opposite polarization detected by absorption of the laser light imaged onto a CCD camera. By varying δ , the change in accumulated phase over the free-precession period, shown in Fig. 31, was converted to an EDM induced frequency shift.

A number of systematic effects were considered, the most important of which were Stark-shift related E^2 effects, correlations with drifts in the magnetic field between subsequent electric field flips, correlations with the ODT laser power, and Stark interference.

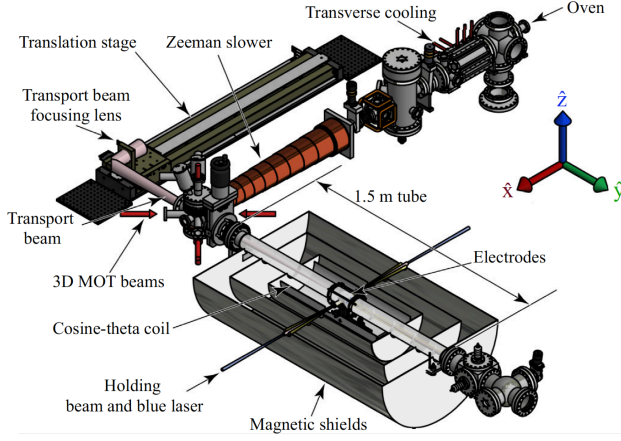


FIG. 29 (Color online) The experimental layout of the ^{225}Ra experiment from Bishof *et al.* (2016) and Parker *et al.* (2015).

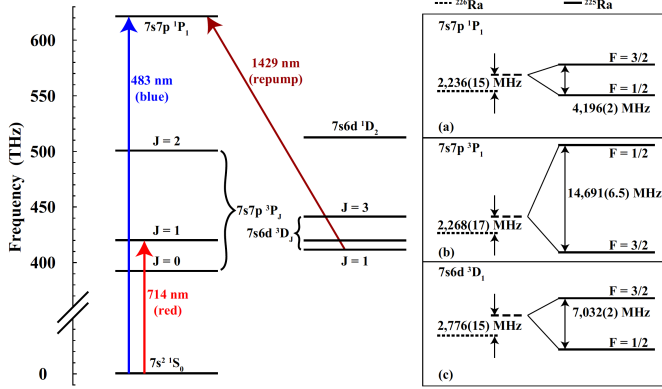


FIG. 30 (Color online) Radium energy-level diagram with the isotope shifts for ^{225}Ra ($I = 1/2$) and ^{226}Ra ($I = 0$) relative to the isotopic average are shown on the right; (a), (b) and (c) show the specific levels of interest. Figure from Bishof *et al.* (2016) and Parker *et al.* (2015).

The most recent ^{225}Ra EDM result

$$d(^{225}\text{Ra}) = (4 \pm 6_{\text{stat}} \pm 0.2_{\text{sys}}) \times 10^{-24} \text{ e-cm}, \quad (113)$$

represents at 95% upper-limit of 1.4×10^{-23} e-cm. This was a 36-fold improvement over the first run and an estimated 95% c.l. upper limit of 1.4×10^{-23} e-cm (95%)

A disadvantage of the imaging technique for probing the spin-state population is that only a small fraction of the atoms absorb the probe light so that the contrast is low and the statistical error is dominated by photon counting statistics and not the number of ^{225}Ra atoms. This can be mitigated by essentially counting atoms using the STIRAP technique (Bergmann *et al.*, 1998)

Estimated production rates at FRIB are based on fragmentation models on light targets, may provide several orders of magnitude more ^{225}Ra .

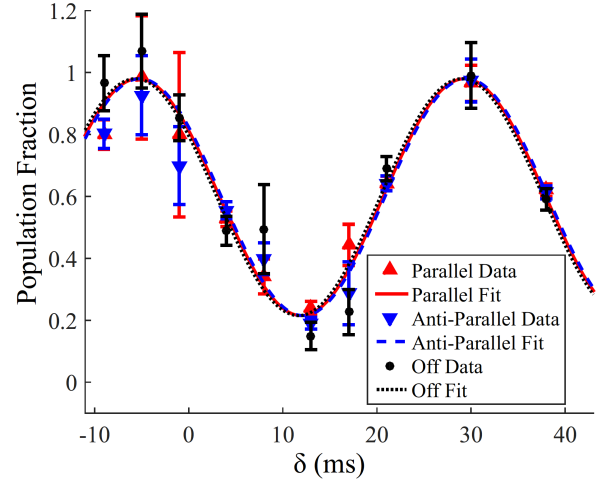


FIG. 31 (Color online) Phase-shift data showing the population of spin-down ^{225}Ra nuclei after the nuclear-spin precession cycle of $20 + \delta$ seconds. Figure from Bishof *et al.* (2016) and Parker *et al.* (2015).

$^{221/223}\text{Rn}$

Radon isotopes present the possibility of using techniques developed for the ^{129}Xe EDM measurements and exploiting potential enhancements due to octupole collectivity in $^{221/223}\text{Rn}$, which have $t_{1/2}$ on the order of 20-30 minutes. A program to develop an on-line EDM experiment at TRIUMF has been underway, and the prospects of producing and harvesting from the beam dump significantly greater quantities of atoms at FRIB is very promising (Pen *et al.*, 2014). The on-line EDM measurement consists of the following elements: 1.) on-line collection and transfer of radon isotopes, 2.) optical pumping polarization by spin exchange (SEOP), 3.) polarized gas transport to the EDM cell and gas recovery, 4.) EDM cells and high voltage, 5.) magnetic field, magnetic shielding and monitoring, 6.) spin-precession monitoring.

For collection and transfer, a 40 kV rare-gas isotope beam was incident on a tantalum foil (Warner *et al.*, 2005) for typically two half-lives and then transferred to a LN_2 -cooled cold-finger, from which the gas was then released by rapidly warming the cold finger and pushed into the SEOP cell by a piston of N_2 gas. The N_2 gas also served as a buffer gas for noble gas polarization and as an insulating gas for the high voltage applied to the EDM cells. Nearly 100% collection efficiency was demonstrated (Nuss-Warren *et al.*, 2004; Warner *et al.*, 2005). SEOP produced ^{209}Rn and ^{221}Rn polarization of $\approx 10\%$ (Kitano *et al.*, 1988; Tardiff *et al.*, 2008) and relaxation times ($T_1 \approx 15 \text{ s}$) (Tardiff *et al.*, 2008) were measured. Since each EDM measurement is limited by the spin-coherence time to about one minute, whereas the half-life of the Rn isotopes of interest is about 30 min. The Rn/ N_2 mixture can be recycled into the polarizer cell by a circulating system. A measurement cycle will

be initiated by a $\pi/2$ pulse after which the nuclear spins freely precess in the x - y plane (\vec{E} and \vec{B} are along \hat{z}). The radon-isotope free precession can be monitored by the gamma-ray anisotropy technique or by two-photon magnetometry (Degenkolb and Chupp, 2011).

Estimates of the $^{221/223}\text{Rn}$ production rates are based on measured rates at ISOLDE and TRIUMF. At ISOLDE (Gaffney *et al.*, 2013), 1.4×10^7 ^{220}Rn s^{-1} were delivered to the low-energy end of the REX-ISOLDE accelerator with a $1.6 \mu\text{A}$ 1.4 GeV proton beam incident on a thick UC target. With $10 \mu\text{A}$, 10^8 ^{221}Rn s^{-1} and 2×10^7 ^{223}Rn s^{-1} are expected. This would provide about 3×10^{10} nuclei for each 1-hour collection cycle. Estimated production rates at FRIB, based on fragmentation models on light targets *i.e.* the water in the FRIB beam dump, are up to $100\times$ greater; however extraction of a large fraction of this remains a challenge.

Radon spin precession can be measured by gamma-ray anisotropy or by direct optical detection. The gamma-anisotropy is a $P_2(\cos\theta)$ distribution of photons emitted after a polarized nucleus decays to the excited-states of the daughter. For a precessing-polarized sample, the detection rate for photons in a detector at a specific azimuthal position is modulated at twice the precession frequency (2ω). The statistical power of the gamma-ray anisotropy technique for the Radon-EDM measurement is limited by the intrinsic photo-peak count rate limit for typical high-purity germanium gamma-ray detectors. Optical detection monitors the projection of the nuclear spin along the laser propagation direction by monitoring transmission or fluorescence of circularly polarized light or optical rotation of linearly polarized light. For radon, the single and two photon transitions correspond to wavelengths of 178 nm and 257 nm respectively, and the two-photon magnetometry techniques discussed in Sec. III.B can be applied to radon atoms. In the transmission/fluorescence case, photons and angular momentum are absorbed by the atoms and the measurement is destructive in the sense that the initial state of an atom is changed and thus affects the spin-coherence time τ . Therefore the intensity of the light is adjusted to optimize the measurement. It is also possible to use the Ramsey separated-oscillatory-field technique to allow the spins to “precess in the dark.” With a fluorescence collection efficiency of 10%, a photon-statistics-limited EDM sensitivity of 3×10^{-26} could be achieved in one day assuming a 50% duty cycle, $E = 10 \text{ kV/cm}$ and $\tau = 15 \text{ sec}$. With anticipated FRIB production rates, a sensitivity of 3×10^{-28} e-cm in 100 days is a reasonable running-time scenario for an off-line experiment using isotopes harvested from the beam dump (Pen *et al.*, 2014). The octupole enhancement also provides for different isotopes of the same atomic species as comagnetometers, *e.g.* ^{211}Rn and ^{209}Rn .

G. Other prospects: Storage ring EDMs

Over the last two decades, EDM measurement techniques using storage rings have been developed using inspiration from the muon “g-2” experiment at Brookhaven National Laboratory (Bennett *et al.*, 2006). The concept, introduced by (Farley *et al.*, 2004), is based on the evolution of the momentum and spin of a charged particle in the presence of magnetic and electric fields.

For a relativistic particle of charge q and rest mass m , the equation of motion in the lab frame is

$$\frac{d\vec{p}}{dt} = q \left(\vec{v} \times \vec{B} + \vec{E} \right) \quad (114)$$

and the acceleration in the lab frame is (Jackson, 1975)

$$\begin{aligned} \vec{a} = \frac{d\vec{v}}{dt} &= \frac{q}{m\gamma} \left[\vec{v} \times \vec{B} + \vec{E} - \left(\frac{\vec{v} \cdot \vec{E}}{c^2} \right) \vec{v} \right] \\ &= \frac{q}{m\gamma} \left[\vec{\omega}_v \times \vec{v} + \frac{1}{\gamma^2 - 1} \left(\frac{\vec{v} \cdot \vec{E}}{c^2} \right) \vec{v} \right] \end{aligned} \quad (115)$$

where \vec{B} & \vec{E} are the static & uniform magnetic & electric fields in the lab frame, $\gamma = (1 - v^2/c^2)^{-1}$ is the Lorentz factor, t is the time in the lab frame, τ is the proper time in the particle rest frame. The rotation of the velocity in the lab frame is

$$\vec{\omega}_v = \frac{\gamma^2}{\gamma^2 - 1} \left(\frac{\vec{v} \times \vec{E}}{c^2} \right) - \vec{B}. \quad (116)$$

The torque on the particle’s spin \vec{s} is

$$\frac{d\vec{s}}{d\tau} = \gamma \left[\frac{d\vec{s}}{dt} \right] = \vec{\mu} \times \vec{B}' + \vec{d} \times \vec{E}' \quad (117)$$

where the magnetic moment $\vec{\mu}$ and the EDM \vec{d} are

$$\vec{\mu} = g(q/2m)\vec{s} \quad \vec{d} = \eta(q/2mc)\vec{s}, \quad (118)$$

and

$$\begin{aligned} \vec{B}' &= \gamma \left(\vec{B} - \frac{\vec{v} \times \vec{E}}{c^2} \right) - \frac{\gamma^2}{\gamma + 1} \frac{\vec{v} \cdot (\vec{v} \cdot \vec{B})}{c^2} \\ \vec{E}' &= \gamma \left(\vec{E} + \vec{v} \times \vec{B} \right) - \frac{\gamma^2}{\gamma + 1} \frac{\vec{v} \cdot (\vec{v} \cdot \vec{E})}{c^2}. \end{aligned} \quad (119)$$

For magnetic storage rings, $\vec{v} \times \vec{B} \approx 3000 \text{ kV/cm/T}$, which is about 100-times larger than a typical laboratory electric field \vec{E} for typical magnetic fields (e.g. $B = 1.45 \text{ T}$ for the Brookhaven $g-2$ experiment). In the lab frame, accounting for the Thomas precession (Thomas, 1927), the equation of motion for the spin is

$$\frac{d\vec{s}}{dt} = \left[\frac{d\vec{s}}{dt} \right]_{\text{rest}} + \frac{\gamma^2}{\gamma + 1} \frac{\vec{s} \times (\vec{v} \times \vec{a})}{c^2} \quad (120)$$

Combining the preceding equations, the evolution of the spin in the lab frame is

$$\begin{aligned}
\frac{d\vec{s}}{dt} &= \vec{\omega}_s \times \vec{s} \\
&= \left(\frac{q}{m\gamma}\right) \vec{s} \times \left[\vec{B} - \frac{\gamma}{(\gamma+1)} \frac{\vec{v} \times \vec{E}}{c^2} \right] \\
&+ \left(\frac{aq}{m}\right) \vec{s} \times \left[\vec{B} - \frac{\vec{v} \times \vec{E}}{c^2} - \frac{\gamma}{\gamma+1} \frac{\vec{v}(\vec{v} \cdot \vec{B})}{c^2} \right] \\
&+ \left(\frac{\eta q}{2mc}\right) \vec{s} \times \left[\vec{E} + \vec{v} \times \vec{B} - \frac{\gamma}{\gamma+1} \frac{\vec{v}(\vec{v} \cdot \vec{E})}{c^2} \right]
\end{aligned} \tag{121}$$

The first two terms combined, the non-covariant form of the Bargmann-Michel-Telegedi or BMT equation (Bargmann *et al.*, 1959) give the torque on the spin in the lab frame due to the magnetic moment. The third term in square brackets, proportional to η , is due to the EDM. Experiments measure the rotation of the spin with respect to the velocity in the lab frame, *i.e.* $\vec{\omega}_s - \vec{\omega}_v$

$$\begin{aligned}
\vec{\omega}_a &= \frac{aq}{m} \left[\vec{B} + \left(\frac{1}{a(\gamma^2 - 1) - 1} \right) \frac{\vec{v} \times \vec{E}}{c^2} - \frac{\gamma}{\gamma+1} \frac{\vec{v}(\vec{v} \cdot \vec{B})}{c^2} \right] \\
\vec{\omega}_d &= \frac{d}{\hbar J} \left[\vec{v} \times \vec{B} + \vec{E} - \frac{\gamma}{\gamma+1} \frac{\vec{v} \cdot \vec{E}}{c^2} \vec{v} \right] \\
&= \frac{d\vec{E}'}{\hbar J \gamma}.
\end{aligned} \tag{122}$$

Here a is the magnetic moment anomaly, $\vec{s} = \hbar \vec{J}$, and J is the spin of the particle. For leptons

$$a = \frac{g-2}{2} = \left(\frac{\mu}{\mu_B} \right) \left(\frac{e}{q} \right) \left(\frac{m}{m_e} \right) - 1 \tag{123}$$

and for bare nuclei (Khriplovich, 1998)

$$a = \frac{g-2}{2} = \frac{1}{2J} \left(\frac{\mu}{\mu_N} \right) \left(\frac{A}{Z} \right) - 1 = \frac{\kappa}{Z}, \tag{124}$$

where $\mu_{N(B)}$ is the nuclear (Bohr) magneton, $Z = q/e$, e is the elementary charge, $A = m/m_p$, $m_{p(e)}$ is the mass of the proton (electron), and κ is the customary anomalous magnetic moment. Measurement of $\vec{\omega}_a$ is the basis of the muon $g-2$ experiments, which currently show a greater than $3\text{-}\sigma$ discrepancy with the Standard-Model calculation (Bennett *et al.*, 2006). Note that the EDM precession $\vec{\omega}_d$ is perpendicular to $\vec{\omega}_a$.

The EDM experiments envision the charged particle of a carefully chosen energy with initially only longitudinal spin polarization, *i.e.* \vec{s} parallel to \vec{p} , is injected into a storage ring. In the presence of appropriately chosen static laboratory electric and magnetic fields, the spin polarization of the particle will slowly develop a spin component transverse to its velocity, *i.e.* pointing out of the

storage-ring plane, which is linearly proportional to η . After a suitably long circulation time, the direction of the particle's spin polarization vector is determined for example by measuring the polarization-dependent decay asymmetry in the case of the muon or elastic scattering for stable nuclei. The statistical uncertainty follows Eq. 6 with the substitution of E'/γ , the electric field in the particle rest frame:

$$\sigma_d = \frac{\gamma \hbar J}{E' P A} \frac{1}{\sqrt{N T \tau}}, \tag{125}$$

where the particle polarization is P and the experimental analyzing power is A , which are both ≤ 1 , N is the number of particles detected for a measurement of duration τ and T the total running time.

The key insight of the dedicated storage-ring EDM measurement technique (Farley *et al.*, 2004) is choosing the electric and magnetic fields as well as the particle's momentum such that the ω_a is suppressed. This is accomplished by first making \vec{E} , \vec{B} and the velocity all mutually orthogonal and then either choosing a radial electric field $E_r = aBv\gamma^2/(1 - ab^2\gamma^2)$, which cancels ω_a or by setting $\vec{B} \approx 0$ and storing particles with momentum $p = mc/\sqrt{a}$, *i.e.* purely electric confinement. A critical challenge is to minimize undesired radial magnetic fields due to misalignments and fringe fields, which would result in the transverse polarization due to the normal “ $g-2$ ” spin precession and would mimic the EDM signal. Injection of simultaneous counter-propagating beams into the storage ring has been proposed to control these effects (Anastassopoulos *et al.*, 2016). Choosing $B \approx 0$ requires effective magnetic shielding as discussed for the storage-ring proton-EDM experiment in sec. III.A.

Generic proposals have been made to search for EDMs with unstable charged ions using the beta-decay asymmetry for polarimetry similar to the muon $g-2$ concept (Khriplovich, 1998, 2000a,b) and with highly charged ions (Bondarevskaya *et al.*, 2011). Current efforts to develop storage ring EDM experiments for muons, protons, deuterons, and ^3He (helion) nuclei are summarized in Table XI.

Farley *et al.* (2004) presented the first storage ring proposal for a dedicated EDM measurement along with a detailed discussion of systematic effects. This proposal focused on a muon EDM measurement and chose technically feasible values for \vec{E} and β in order to make \vec{B}_a equal to zero. The EDM-sensitive spin precession is driven mainly by the motional electric field. The primary method to control for systematic effects due to undesired field components is to inject counter-propagating beams into the storage ring simultaneously. Unlike the EDM signal, the sign of the systematic effect would depend on the direction of beam propagation providing a way to disentangle the two sources of transverse polarization. Other false effects, such as the non-orthogonality of the

particle (units)	J	a	$ \vec{p} $ (GeV/c)	γ	$ \vec{B} $ (T)	$ \vec{E} $ (kV/cm)	$ \vec{E}' /\gamma$ (kV/cm)	R (m)	σ_d^{goal} (e cm)	Ref.
μ^\pm	1/2	+0.00117	3.094	29.3	1.45	0	4300	7.11	10^{-21}	E989
			0.3	3.0	3.0	0	8500	0.333	10^{-21}	E34
			0.5	5.0	0.25	22	760	7	10^{-24}	srEDM
			0.125	1.57	1	6.7	2300	0.42	10^{-24}	PSI
p^+	1/2	+1.79285	0.7007	1.248	0	80	80	52.3	10^{-29}	srEDM
			0.7007	1.248	0	140	140	30	10^{-29}	JEDI
d^+	1	-0.14299	1.0	1.13	0.5	120	580	8.4	10^{-29}	srEDM
			1.000	1.13	0.135	33	160	30	10^{-29}	JEDI
$^3\text{He}^{++}$	1/2	-4.18415	1.211	1.09	0.042	140	89	30	10^{-29}	JEDI

TABLE XI Relevant Parameters for Proposed Storage Ring EDM Searches. The present muon EDM limit is 1.8×10^{-19} e cm and the indirect limit on the proton EDM from derived from the atomic EDM limit of ^{199}Hg is 2×10^{-25} e cm. The magnetic moment anomaly is calculated using values for the unshielded magnetic moments of the particles from CODATA 2014 (Mohr *et al.*, 2016). The sign convention for the positively charged particles is such that the magnetic field is vertical and the particles are circulating. References are E989: Muon $g-2$ experiment at Fermilab (Gorringe and Hertzog, 2015); E34: Muon $g-2$ experiment at JPARC (Gorringe and Hertzog, 2015); srEDM: Muon EDM at JPARC (Farley *et al.*, 2004), “All-Electric” Proton EDM at Brookhaven (Anastassopoulos *et al.*, 2016), Deuteron EDM at JPARC (Morse, 2011); PSI: Compact Muon EDM (Adelmann *et al.*, 2010); JEDI: “All-In-One” Proton, Deuteron, & Helion EDM at COSY (Rathmann *et al.*, 2013b).

electric and magnetic fields, would be cancelled by summing over detectors positioned 180° apart azimuthally around the ring.

The current muon EDM limit $d_\mu \leq 10^{-19}$ e-cm is derived from ancillary measurements of the muon decay asymmetry taken during a precision measurement muon anomalous magnetic moment (Bennett *et al.*, 2009). The sensitivity of this measurement was limited by the fact that the apparatus was designed to be maximally sensitive to the spin precession to the muon anomalous magnetic moment. For a dedicated muon EDM experiment, under development at JPARC (Farley *et al.*, 2004) & PSI (Adelmann *et al.*, 2010), \vec{E} and γ are chosen to make $\vec{w}_a = 0$. The spin coherence time τ in this case is limited by the muon lifetime in the lab frame ($2.2 \mu\text{s} \times \gamma$). An alternative muon EDM approach using lower energy muons and a smaller and more compact storage ring is being developed at the PSI. A proposal for loading such a compact storage ring as well as an evaluation of the systematic effects due specifically to the lower muon energy is presented by Adelmann *et al.* (2010).

For the case of a proton EDM search, $\vec{B} = 0$, and choosing $\beta = 1/\sqrt{a+1}$ suppresses the $\vec{\beta} \times \vec{E}$ term (Anastassopoulos *et al.*, 2016). The electric storage ring with bending radius $R = (m/e)/(E\sqrt{a(a+1)})$ is generally only possible for particles with a positive magnetic moment anomalies ($a > 0$). With $E = 10^6$ V/m bending radii of $R \approx 10$ m is required for protons. Magnetic-shielding challenges are addressed in Sec. III.A. Progress has been made in describing the challenging problem of orbital & spin dynamics inside electrostatic rings (Hacımeroglu and Semertzidis, 2014; Mane, 2008, 2012, 2014a,b,c, 2015a,b,c; Metodiev *et al.*, 2015), developing simulation code for electrostatic rings (Talman and Talman, 2015a,b), and calculating the fringe fields for dif-

ferent plate geometries (Metodiev *et al.*, 2014).

To achieve sensitivity of 10^{-29} e-cm, impractically small residual magnetic fields would be required, thus two counter propagating beams within the same storage ring are envisioned, for which a vertical separation would develop in the presence of a radial magnetic field. After several cycles around the ring, this vertical separation would be large enough to measure using SQUID magnetometers as precision beam position monitors (BPMs). Efforts are underway to develop an electrostatic proton EDM storage ring at Brookhaven National Lab in Upton, NY, USA that would fit inside the tunnel of and along side the Alternating Gradient Synchrotron (AGS).

A magnetic storage ring could also be used to measure the deuteron EDM using a similar technique, and requires knowledge of how a spin-1 particle evolves in electromagnetic fields (Silenko, 2015). The two main differences from a muon EDM experiment are the need for more careful control of the beam properties to preserve the spin coherence and, of course, a different spin polarimetry scheme. A spread in the beam position and momentum smears the cancellation of the “g-2” spin precession which would, after many cycles, result in decoherence of the beam. Since the muon spin coherence time is limited by the finite muon lifetime, this is not as critical for the muon EDM experiment. The goal for the deuteron EDM experiment is to maintain the spin coherence for at least as long as the vacuum-limited ion storage time which is about 10^3 seconds for a vacuum of 10^{-10} Torr. The deuteron polarization would be analyzed by the asymmetry in elastic scattering from a carbon target (Brantjes *et al.*, 2012). The muon and deuteron EDM experiments, as well as a next generation muon anomalous magnetic moment experiment, are being pursued by the Storage Ring EDM collaboration (srEDM)

at the Japanese Proton Accelerator Center (JPARC) in Tokai, Japan.

A distinct but similar approach is currently being developed by the the Jülich Electric Dipole moment Investigations (JEDI) collaboration in Germany. Long term plans are to measure the EDMs of the proton, deuteron, and ^3He using an “all-in-one” storage ring. As an intermediate step, they plan on directly measuring the proton and deuteron EDMs at a lower statistical sensitivity using the presently available magnetostatic Cooler Synchrotron (COSY) storage ring with some modifications. The main challenge is to introduce beam-line elements that prevent the spin precession due to the magnetic moment anomaly from washing out the torque on the spin generated by the presence of an EDM. Although it has been suggested to synchronize this EDM torque to the magnetic moment anomaly spin precession (Orlov *et al.*, 2006), the approach being developed for COSY by the JEDI collaboration is to partially “freeze” or lock the spin to the momentum using an element called a “magic” RF Wien filter (Morse *et al.*, 2013). If the parameters of the the Wien filter are carefully chosen, one component of the particle’s spin does not undergo the usual magnetic moment anomaly spin precession, which would allow the EDM torque to build up a traverse polarization.

Spin polarimetry is critical for both measuring the EDM signal as well as for diagnosing and improving the spin coherence time. Significant progress has been made towards controlling systematics related to spin polarimetry for deuterons. Results indicate that precision polarimetry for both deuterons and protons is feasible at the ppm level, which is required for a $10^{-29} e \cdot \text{cm}$ EDM sensitivity. Preliminary efforts to measure and improve spin coherence times of deuterons using the COSY storage ring have also been reported (Bagdasarian *et al.*, 2014; Benati *et al.*, 2012, 2013). High precision (10^{-10}) control and monitoring of the spin motion of deuterons at COSY has also been demonstrated (Eversmann *et al.*, 2015). Plans are also underway to develop an ion source and polarimetry for ^3He by the JEDI collaboration. Although significant effort is still required to perform storage ring EDM experiments, they would provide the most direct and clean measurements of the EDM of light ions and muons and would improve the limits on their EDMs by several orders of magnitude.

V. INTERPRETATIONS OF CURRENT AND PROSPECTIVE EXPERIMENTS

In general there are many possible contributions to the EDM of any system accessible to experiment, for example the neutron EDM may arise due to a number of sources including short range, *e.g.* quark EDMs, and long range pion-nucleon couplings characterized by $\bar{g}_\pi^{(0)}$ and $\bar{g}_\pi^{(1)}$. One approach to putting EDM results in con-

text has been to use the upper limit from an experiment to set limits on individual phenomenological parameters making use of theoretical calculations, which establish the dependence on the individual parameters. This is the conventional approach, and is based on the reasoning that if the measured EDM is small then either all the contributions to the EDM (all the $\alpha_i C_i$) are small as well or large contributions must effectively cancel, that is have opposite signs and similar magnitudes. While such a cancellation would be fortuitous, it may be “required” in the sense that any underlying source of CP violation generally contributes CP violation in more than one way. Take, for example, a Left-Right Symmetric model, which contributes to both $\bar{g}_\pi^{(1)}$ and the short-range part of the neutron EDM, \bar{d}_n^{sr} as given in equations 47, 48 and 50; however a cancellation would require a value of $\sin \xi$ less than 2×10^{-6} . Thus in this model, either the phase α is very small or the mixing angle is very small, or both.

A. Sole source

Sole-source limits on the low-energy parameters are presented in Table XII along with the system that sets the limits. The most conservative upper limit is derived using the smallest $|\alpha_{ij}|$ from the ranges presented in tables III and IV. The sole-source short-range neutron contribution assumes $\bar{g}_\pi^0 = \bar{g}_\pi^1 = 0$ comes from the neutron-EDM limit. For the short-range proton contribution, the model of Coveney and Sandars (1983c) is used for TIF and from Dmitriev and Sen’kov (2003) for ^{199}Hg . The combination of light quark EDMs $d_d - 1/3d_u$ is derived from the limit on d_n . The parameter $\bar{\theta}$ and the combination of chromo-EDMs $\tilde{d}_d - \tilde{d}_u$ are derived from the sole-source limits on \bar{g}_π^0 and \bar{g}_π^1 , respectively.

B. Global Analysis

A global analysis of EDM results has been introduced by Chupp and Ramsey-Musolf (2015) which sets simultaneous limits on six low-energy parameters: d_e , C_S , C_T , \bar{g}_π^0 , \bar{g}_π^1 and the short-range component of the neutron EDM d_n^{sr} , and is updated here, in particular with new results from HfF^+ , ^{199}Hg and ^{225}Ra along with clarifications of the isospin dependence of C_T .

Paramagnetic systems: limits on d_e and C_S

Results are listed in Table I for paramagnetic systems Cs, Tl, YbF, ThO and HfF^+ . Following Dzuba *et al.* (2011) we take the electron EDM result reported by each author to be the combination

$$d_j^{\text{exp}} = d_e + \left(\frac{\alpha_{C_S}}{\alpha_{d_e}} \right)_j C_S. \quad (126)$$

Parameter	system	95% u.l.
d_e	ThO	9.2×10^{-29} e-cm
C_S	ThO	8.6×10^{-9}
C_T	^{199}Hg	3.6×10^{-10}
\bar{g}_π^0	^{199}Hg	3.8×10^{-12}
\bar{g}_π^1	neutron	2.2×10^{-12}
\bar{g}_π^2	^{199}Hg	3.8×10^{-13}
\bar{g}_π^3	TlF	4.1×10^{-10}
\bar{g}_π^4	^{199}Hg	2.6×10^{-11}
d_n^{sr}	neutron	3.3×10^{-26} e-cm
d_p^{sr}	TlF	8.7×10^{-23} e-cm
d_p^{sr}	^{199}Hg	2.0×10^{-25} e-cm
Other parameters		
d_d	$\approx 3/4 d_n$	2.5×10^{-26} e-cm
θ	$\approx \bar{g}_\pi^0/(0.02)$	1.9×10^{-10}
$\tilde{d}_d - \tilde{d}_u$	$5 \times 10^{-15} \bar{g}_\pi^{-1}$ e-cm	2×10^{-27} e-cm

TABLE XII Sole-source limits (95% c.l.) on the absolute value of the parameters presented in Sec. II.C assuming a single contribution to the EDM or, for molecules, the P-odd/T-odd observable. The lower part of the table presents limits on other parameters derived from the six low energy parameters.

The $\alpha_{C_S}/\alpha_{d_e}$ are listed in Table III. As pointed out by Dzuba *et al.* (2011), though there is a significant range of α_{d_e} and α_{C_S} from different authors for several cases, there is much less dispersion in the ratio $\alpha_{C_S}/\alpha_{d_e}$.

In Figure 32, we plot d_e vs C_S for the $d_{\text{para}}^{\text{exp}}$ for ThO and HfF⁺ along with 68% and 95% confidence-level contours for χ^2 on the d_e - C_S space, where

$$\chi^2 = \sum_i \frac{[d_i^{\text{exp}} - d_e - (\frac{\alpha_{C_S}}{\alpha_{d_e}})_i C_S]^2}{\sigma_i^2}, \quad (127)$$

and i includes Cs, Tl, YbF, ThO and HfF⁺, but only ThO and HfF⁺ have significant impact. The range of $(\frac{\alpha_{C_S}}{\alpha_{d_e}})_j$ expressed in Table III, about 10%, is accommodated by adding in quadrature to the total experimental uncertainty for each system. The resulting constraints from all paramagnetic systems on d_e and C_S at 68% c.l. are

$$d_e = (0.3 \pm 9.2) \times 10^{-28} \text{ e cm} \quad C_S = (0.6 \pm 3.2) \times 10^{-9}. \quad (128)$$

The upper limits at 95% confidence level are

$$|d_e| < 1.9 \times 10^{-28} \text{ e cm} \quad |C_S| < 6.3 \times 10^{-9} \quad (95\% \text{ c.l.}). \quad (129)$$

Note that the constraint on C_S is actually better than that from ThO alone.

Corresponding 95% c.l. constraints on $\delta_e(v/\Lambda)^2$ and $\text{Im} C_{eq}^{(-)}(v/\Lambda)^2$, obtained from those for d_e and C_S by dividing by -3.2×10^{-22} e cm and -12.7 , respectively are

$$|\delta_e(v/\Lambda)^2| < 6.7 \times 10^{-7} \quad \text{Im} C_{eq}^{(-)}(v/\Lambda)^2 < 7.5 \times 10^{-10}. \quad (130)$$

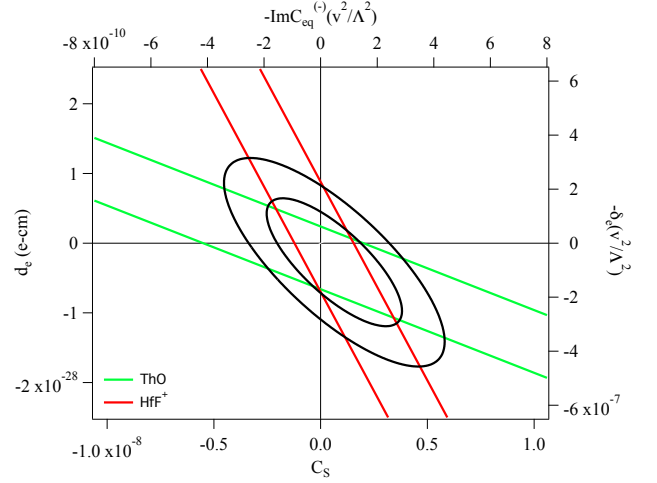


FIG. 32 (Color online) Electron EDM d_e as a function of C_S from the experimental results in ThO and HfF⁺ with 1σ experimental error bars. Also shown are 68% and 95% χ^2 contours for all paramagnetic systems including Cs, Tl, YbF. Also shown on the top and right axes are the corresponding dimensionless Wilson coefficients δ_e and $\text{Im} C_{eq}^{(-)}$ normalized to the squared scale ratio $(v/\Lambda)^2$.

Hadronic parameters and C_T

Since the introduction of the global analysis (Chupp and Ramsey-Musolf, 2015), there have been three significant developments in the diamagnetic/hadronic systems:

- the four-times more sensitive result for ^{199}Hg (Graner *et al.*, 2016)
- reanalysis of the neutron-EDM which increased the uncertainty and moved the centroid by about $1/4$ σ (Pendlebury *et al.*, 2015),
- results from the octupole deformed ^{225}Ra (Parker *et al.*, 2015)

There are experimental results in five systems and four parameters d_n^{sr} , C_T , $\bar{g}_\pi^{(0)}$ and $\bar{g}_\pi^{(1)}$, which are fully constrained once d_e and C_S are fixed from the paramagnetic-systems results. In order to provide estimates of the allowed ranges of the four parameters, χ^2 is defined as

$$\chi^2(\mathbf{C}_j) = \sum_i \frac{(d_i^{\text{exp}} - d_i)^2}{\sigma_{d_i^{\text{exp}}}^2}, \quad (131)$$

where d_i is given in equation 9. The four parameters \mathbf{C}_j are varied to determine χ^2 contours for a specific set of α_{ij} . For 68% confidence and four parameters, $(\chi^2 - \chi_{\min}^2) < 4.7$. The α_{ij} are varied over the ranges presented in Table IV to reflect the hadronic-theory uncertainties. Estimates of the constraints are presented as ranges in Table XIII, which has been updated from Chupp and Ramsey-Musolf (2015). The significant improvement in limits on C_T is largely due to

the change in sensitivity estimates ($\alpha_{iC_T^0}$) due to the recent calculations of the tensor form factors (see Eq. 64). Limits on $\bar{g}_\pi^{(0)}$ also improve by about 50% while limits on $\bar{g}_\pi^{(1)}$ and \bar{d}_n^{sr} are about 50% less stringent.

In this global analysis the short-range neutron contribution is notably much less well constrained than the experimental limit on the neutron EDM because $\bar{g}_\pi^{(0)}$ and $\bar{g}_\pi^{(1)}$ also contribute to the neutron EDM and these are less constrained by the combinations of ^{199}Hg , ^{129}Xe , ^{225}Ra and TIF results; however the constraints do have significant correlations. The correlations of pairs of parameters are illustrated in Fig. 33, which shows the 68% contour on plots of allowed values of d_n^{sr} vs $\bar{g}_\pi^{(0)}$, $\bar{g}_\pi^{(1)}$ and $C_T^{(0)}$ as well $\bar{g}_\pi^{(1)}$ vs $\bar{g}_\pi^{(0)}$.

In this global analysis approach, the constraints on each parameter depend on all experiments, which severely weakens the upper limits due to the range of sensitivity of the EDM results and the range of theoretical uncertainties of the α_{ij} given in Table IV. It is illustrative show how the parameters depend on the experimental results from ^{199}Hg , ^{129}Xe , ^{225}Ra and the neutron, all of which promise significant improvement in experimental sensitivity in the coming years. Then we can show the dependence of the parameters on the experimental results with the inverse of the matrix α_{ij} from eq. 9:

$$\begin{bmatrix} \bar{d}_n^{sr} \\ \bar{g}_\pi^{(0)} \\ \bar{g}_\pi^{(1)} \\ C_T^{(0)} \end{bmatrix} = \begin{bmatrix} 5.2 & 4.7 \times 10^4 & 9.5 \times 10^3 & 21 \\ -2.8 \times 10^{14} & -3.1 \times 10^{18} & -6.3 \times 10^{17} & -1.4 \times 10^{15} \\ -7.0 \times 10^{13} & -7.7 \times 10^{17} & -1.6 \times 10^{17} & -4.8 \times 10^{14} \\ 1.9 \times 10^{16} & 1.4 \times 10^{19} & 3.6 \times 10^{19} & 8.4 \times 10^{16} \end{bmatrix} \begin{bmatrix} d_n \\ d_{\text{Xe}} \\ d_{\text{Hg}} \\ d_{\text{Ra}} \end{bmatrix}, \quad (132)$$

for the best values from Table IV with $\alpha_{\text{Hg}, \bar{g}_\pi^{(1)}} = 1.6 \times 10^{-17}$ and $\alpha_{\text{Ra}, \bar{d}_n^{sr}} = -8 \times 10^{-4}$. For example

$$\bar{d}_n^{sr} = 5.2d_n + 4.7 \times 10^4 d_{\text{Xe}} + 9.5 \times 10^3 d_{\text{Hg}} + 21d_{\text{Ra}}$$

This combined with the results from Table I shows that the ^{129}Xe and ^{225}Ra results have comparable contributions to the constraints and that improving each by a factor of about 500 would make their impact similar to that of ^{199}Hg in the context of this global analysis.

VI. SUMMARY AND CONCLUSIONS

We live in exciting times for EDMs. The observation and explanations of the baryon asymmetry call for Beyond-Standard-Model sources of CP violation that produce EDMs that may be discovered in the next generation of experiments in a variety of systems. Experiment has marched forward with greater sensitivity recently achieved for the neutron and ^{199}Hg , the tremen-

dous advance in complexity and sensitivity for polar-molecule experiments sensitive to the electron EDM and with new techniques providing results from the octupole deformed ^{225}Ra . The next generation of experiments on the neutron will take advantage of new ideas and techniques incorporated into UCN sources and EDM techniques at a number of laboratories around the world; and new approaches to magnetic shielding and magnetometry/comagnetometry will be essential to achieving the next step in sensitivity in all systems. Storage rings and rare isotopes are expected to be new approaches that move forward in the coming years.

Interpretations of EDM limits and eventually finite results continue to advance with more quantitative connections to baryogenesis and clarification of effective-field theory approaches that connect fundamental quantum field theory to low-energy parameters relevant to the structure of nucleons, nuclei, atoms and molecules. The theory of EDMs brings together theoretical approaches at each of these scales, however the nucleus is a particularly difficult system for calculations and introduces the largest uncertainties in connecting experiment to theory. The best experimental result - in ^{199}Hg - is challenged by significant nuclear theory uncertainties. With the increasing interest in EDMs due to their role in connecting cosmology, particle physics and nuclear/atomic and molecular physics, the motivations for tackling these problems in hadronic theory become stronger.

Even in light of current uncertainties, interpretation of EDM results from the sole-source perspective or in the context of a global analysis show that CP violating parameters are surprisingly small. In the case of the QCD parameter $\bar{\theta}$ this leads to the strong-CP problem and its solution via the axion hypothesis, which may also provide an explanation of non-baryonic dark matter, and experimental searches for the axion. A generic approach to CP violation consistent with current limits combined with an assumption that the phases are of order unity, the mass scale probed is tens of TeV or greater, which emphasizes the complementarity of EDMs and the LHC as well as future higher-energy colliders. In the context of models that introduce new phases such as SUSY variants and Left-Right Symmetric Models, the phases appear to be far less than naturally expected, or the mass scale of CP violation quite large, which introduces challenges with the connection to Electroweak Baryogenesis.

The definitive observation of an EDM in any system will be a tremendous achievement, but a single system alone may not clarify the questions arising in the connections to fundamental theory and to cosmology, for example separating weak and strong CP-violation. We therefore conclude by calling for efforts in several systems - paramagnetic systems most sensitive to the electron EDM and electron-spin-dependent CP violating interactions as well as diamagnetic atoms/molecules, nucleons and nuclear systems where hadronic CP violation

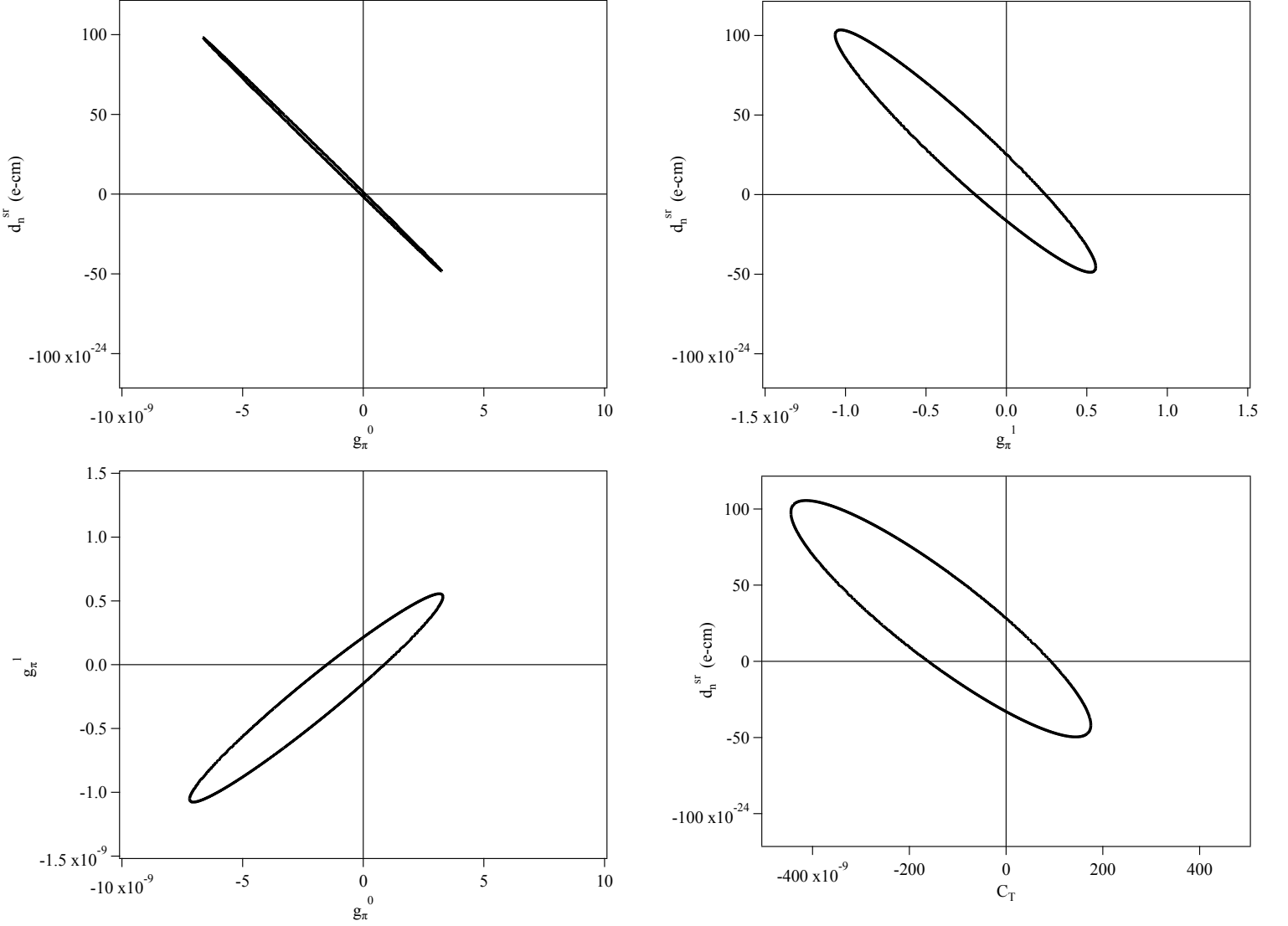


FIG. 33 Combinations of hadronic parameters allowed by experimental results for the best values for α_{ij} in table IV with $\alpha_{\text{Hg}, g_\pi^{(1)}} = 1.6 \times 10^{-17}$ and $\alpha_{\text{Ra}, \bar{d}_n^{sr}} = -8 \times 10^{-4}$. The allowed values at 68% c.l. are contained within the ellipses for each pair of parameters.

	\bar{d}_n^{sr} (e cm)	$\bar{g}_\pi^{(0)}$	$\bar{g}_\pi^{(1)}$	$C_T^{(0)}$
Range from best values with $\alpha_{g_\pi^1}(\text{Hg}) = +1.6 \times 10^{-17}$	$(-4.8-9.8) \times 10^{-23}$	$(-6.6-3.2) \times 10^{-9}$	$(-1.0-0.5) \times 10^{-9}$	$(-3.5-1.6) \times 10^{-7}$
Range from best values with $\alpha_{g_\pi^1}(\text{Hg}) = 0$	$(-4.3-3.4) \times 10^{-23}$	$(-2.3-2.9) \times 10^{-9}$	$(-0.6-1.3) \times 10^{-9}$	$(-3.2-4.0) \times 10^{-7}$
Range from best values with $\alpha_{g_\pi^1}(\text{Hg}) = -4.9 \times 10^{-17}$	$(-9.3-2.6) \times 10^{-23}$	$(-1.8-6.3) \times 10^{-9}$	$(-1.2-0.4) \times 10^{-9}$	$(-11-3.8) \times 10^{-7}$
Range from full variation of α_{ij}	$(-12-12) \times 10^{-23}$	$(-7.9-7.8) \times 10^{-9}$	$(-1.3-1.1) \times 10^{-9}$	$(-6.6-4.6) \times 10^{-7}$
Upper limits (95% c.l.)	23×10^{-23}	15×10^{-9}	2.3×10^{-9}	11×10^{-7}

TABLE XIII Revised values and ranges for coefficients for diamagnetic systems and the neutron. The first three rows give the 68% c.l. range allowed by experiment combined with the best values of the coefficients α_{ij} covering the reasonable range of $\alpha_{\text{Hg}, g_\pi^{(1)}}$ with $\alpha_{\text{Ra}, \bar{d}_n^{sr}} = -8 \times 10^{-4}$; the fourth row gives ranges of coefficients for the entire reasonable ranges of the coefficients α_{ij} given in Table IV, and the bottom row presents the 95% c.l. upper limits on the coefficients for the full reasonable ranges of the coefficients.

is dominant. We also call for advanced theory efforts, in particular nuclear theory, which must improve to sharpen interpretation of EDM results in all systems.

ACKNOWLEDGMENTS

The authors would like to thank everyone in the community who has provided input and advice as well as encouragement. In particular we are grateful to Martin Burghoff, Will Cairncross, Vincenzo Cirigliano, Skyler Degenkolb, Matthew Dietrich, Peter Geltenbort, Takeyasu Ito, Martin Jung, Zheng-Tian Lu, Kent Leung, Kia Boon Ng, Natasha Sachdeva, Z Sun, Yan Zhou, and Oliver Zimmer. The authors also acknowledge the Excellence Cluster Universe, MIAPP, the Munich Institute for Astronomy and Astrophysics and MITP, the Mainz Institute for Theoretical Physics for hosting and providing the opportunity to collaborate. TC has been supported by US Department of Energy grant No. DE-FG0204ER41331; PF is supported by the Deutsche Forschungsgemeinschaft (DFG) Priority Program SPP 1491 Precision Experiments with Cold and Ultra-Cold Neutrons ; MJRM is supported by US Department of Energy Grant DE-SC0011095; JS is supported by Michigan State University.

REFERENCES

- Aad, G., *et al.* (ATLAS, CMS) (2015), *Proceedings, Meeting of the APS Division of Particles and Fields (DPF 2015)*, Phys. Rev. Lett. **114**, 191803, arXiv:1503.07589 [hep-ex].
- Adelmann, A., K. Kirch, C. J. G. Onderwater, and T. Schietinger (2010), Journal of Physics G: Nuclear and Particle Physics **37** (8), 085001.
- Afach, S., *et al.* (2015), Opt. Express **23** (17), 22108.
- Ahmad, I., R. R. Chasman, J. P. Greene, F. G. Kondev, and S. Zhu (2015), Phys. Rev. C **92**, 024313.
- Ahmad, I., J. E. Gindler, R. R. Betts, R. R. Chasman, and A. M. Friedman (1982), Phys. Rev. Lett. **49**, 1758.
- Aleksandrov, E. B., M. V. Balabas, A. K. Vershovskii, A. E. Ivanov, N. N. Yakobson, V. L. Velichanskii, and N. V. Senkov (1995), Opt. Spectrosc. **78**, 325.
- Alexandrov, E. B., M. V. Balabas, D. Budker, D. English, D. F. Kimball, C.-H. Li, and V. V. Yashchuk (2002), Phys. Rev. A **66**, 042903.
- Allmendinger, F., W. Heil, S. Karpuk, W. Kilian, A. Scharth, U. Schmidt, A. Schnabel, Yu. Sobolev, and K. Tullney (2014), Phys. Rev. Lett. **112** (11), 110801, arXiv:1312.3225 [gr-qc].
- Altarev, I., P. Fierlinger, T. Lins, M. G. Marino, B. Niessen, G. Petzoldt, M. Reisner, S. Stuibler, M. Sturm, J. Taggart Singh, B. Taubenheim, H. K. Rohrer, and U. Schlaepfer (2015a), Journal of Applied Physics **117** (23), 233903, <http://dx.doi.org/10.1063/1.4922671>.
- Altarev, I., P. Fierlinger, T. Lins, M. G. Marino, *et al.* (2015b), J. Appl. Phys. **117** (233903), 1.
- Altarev, I., *et al.* (1980), Nucl. Phys. A **341**, 269.
- Altarev, I., *et al.* (1992), Phys. Lett. B. **276**, 242.
- Altarev, I., *et al.* (2012a), *5th International Workshop on From Parity Violation to Hadronic Structure and More (PAVII1) Rome, Italy, September 5-9, 2011*, Nuovo Cim. **C035N04**, 122.
- Altarev, I., *et al.* (2012b), Patent **WO 2012156278 A1**.
- Altarev, I., *et al.* (2014), Rev. Sci. Instrum. **85**, 075106, arXiv:1403.6467 [physics.ins-det].
- Altmannshofer, W., A. J. Buras, and P. Paradisi (2008), Phys. Lett. **B669**, 239, arXiv:0808.0707 [hep-ph].
- Altmannshofer, W., R. Harnik, and J. Zupan (2013), JHEP **11**, 202, arXiv:1308.3653 [hep-ph].
- Amini, J. M., C. T. Munger, and H. Gould (2007), Phys. Rev. A **75**, 063416.
- Anastassopoulos, V., *et al.* (2016), Review of Scientific Instruments **87** (11), 115116, <http://aip.scitation.org/doi/pdf/10.1063/1.4967465>.
- Anghel, A., *et al.* (2009), Nuclear Instruments and Methods in Physics Research Section A: Accelerators, Spectrometers, Detectors and Associated Equipment **611** (23), 272.
- Archambault, J. P., A. Czarnecki, and M. Pospelov (2004), Phys. Rev. **D70**, 073006, arXiv:hep-ph/0406089 [hep-ph].
- Arkani-Hamed, N., A. Gupta, D. E. Kaplan, N. Weiner, and T. Zorawski (2012), arXiv:1212.6971 [hep-ph].
- Arvanitaki, A., N. Craig, S. Dimopoulos, and G. Villadoro (2013), JHEP **02**, 126, arXiv:1210.0555 [hep-ph].
- Assamagan, K., *et al.* (2016), arXiv:1604.05324 [hep-ph].
- Asztalos, S. J., *et al.* (ADMX) (2010), Phys. Rev. Lett. **104**, 041301, arXiv:0910.5914 [astro-ph.CO].
- Atchison, F., *et al.* (2005), Phys. Rev. C **71**, 054601.
- Atchison, F., *et al.* (2011), Eur. Phys. Lett. **95**, 12001.
- Atchison, T., T. Brys, M. Daum, P. Fierlinger, *et al.* (2007), Phys. Rev. C **76**, 044001.
- Auerbach, N., V. V. Flambaum, and V. Spevak (1996), Phys. Rev. Lett. **76**, 4316.
- Babu, K. S., S. M. Barr, and I. Dorsner (2001), Phys. Rev. **D64**, 053009, arXiv:hep-ph/0012303 [hep-ph].
- Bagdasarian, Z., *et al.* (2014), Phys. Rev. ST Accel. Beams **17**, 052803.
- Baker, C., S. Balashov, J. Butterworth, P. Geltenbort, K. Green, P. Harris, M. van der Grinten, P. Iaydjiev, S. Ivanov, J. Pendlebury, D. Shiers, M. Tucker, and H. Yoshiki (2003), Physics Letters A **308** (1), 67.
- Baker, C., D. Doyle, P. Geltenbort, K. Green, M. van der Grinten, *et al.* (2006), Phys. Rev. Lett. **97**, 131801, arXiv:hep-ex/0602020 [hep-ex].
- Bales, M. J., P. Fierlinger, and R. Golub (2016), Europhysics Lett. **116**, 43002.
- Ban, S., J. Engel, J. Dobaczewski, and A. Shukla (2010), Phys. Rev. C **82**, 015501.
- Barabanov, A. (2006), Phys. Rev. A; Physical Review A" **74** (5), 10.1103/PhysRevA.74.052115.
- Barger, V. D., J. L. Hewett, and R. J. N. Phillips (1990), Phys. Rev. **D41**, 3421.
- Bargmann, V., L. Michel, and V. L. Telegdi (1959), Phys. Rev. Lett. **2**, 435.
- Baron, J., *et al.* (ACME) (2014), Science **343**, 269, arXiv:1310.7534 [physics.atom-ph].
- Baron, J., *et al.* (ACME) (2016), arXiv:1612.09318 [physics.atom-ph].
- Barr, S. M., and A. Zee (1990), Phys. Rev. Lett. **65**, 21, [Erratum: Phys. Rev. Lett. **65**, 2920 (1990)].
- Bear, D. (1998), Phys. Rev. A **57** (6), 5006.
- Benati, P., *et al.* (2012), Phys. Rev. ST Accel. Beams **15**, 124202.

- Benati, P., *et al.* (2013), Phys. Rev. ST Accel. Beams **16**, 049901.
- Bennett, G. W., *et al.* (Muon g-2) (2006), Phys. Rev. **D73**, 072003, arXiv:hep-ex/0602035 [hep-ex].
- Bennett, G. W., *et al.* (Muon (g-2)) (2009), Phys. Rev. **D80**, 052008, arXiv:0811.1207 [hep-ex].
- Bergmann, K., H. Theuer, and B. W. Shore (1998), Rev. Mod. Phys. **70**, 1003.
- Bernreuther, W., and M. Suzuki (1991a), Rev. Mod. Phys. **63**, 313.
- Bernreuther, W., and M. Suzuki (1991b), Rev. Mod. Phys. **63**, 313.
- Bhattacharya, T., V. Cirigliano, S. Cohen, R. Gupta, A. Joseph, H.-W. Lin, and B. Yoon (PNDME) (2015a), Phys. Rev. **D92** (9), 094511, arXiv:1506.06411 [hep-lat].
- Bhattacharya, T., V. Cirigliano, S. Cohen, R. Gupta, H.-W. Lin, and B. Yoon (2016), Phys. Rev. **D94** (5), 054508, arXiv:1606.07049 [hep-lat].
- Bhattacharya, T., V. Cirigliano, R. Gupta, H.-W. Lin, and B. Yoon (2015b), Phys. Rev. Lett. **115** (21), 212002, arXiv:1506.04196 [hep-lat].
- Bian, L., T. Liu, and J. Shu (2015), Phys. Rev. Lett. **115**, 021801, arXiv:1411.6695 [hep-ph].
- Bishof, M., R. H. Parker, K. G. Bailey, J. P. Greene, R. J. Holt, M. R. Kalita, W. Korsch, N. D. Lemke, Z.-T. Lu, P. Mueller, T. P. O'Connor, J. T. Singh, and M. R. Dietrich (2016), Phys. Rev. C **94**, 025501.
- Bloom, A. (1962), Appl. Opt. **1**, 1.
- Bondarevskaya, A., A. Prozorov, L. Labzowsky, G. Plunien, D. Liesen, and F. Bosch (2011), Physics Reports **507** (1), 1.
- Bork, J., H.-D. Hahlbohm, R. Klein, and A. Schnabel (2002), Proceedings 13th International Conference on Biomagnetism (Biomag2002), 970.
- Bouchard, C., C. C. Chang, T. Kurth, K. Orginos, and A. Walker-Loud (2016), arXiv:1612.06963 [hep-lat].
- Brantjes, N., *et al.* (2012), Nuclear Instruments and Methods in Physics Research Section A: Accelerators, Spectrometers, Detectors and Associated Equipment **664** (1), 49.
- Brenner, T., P. Fierlinger, P. Geltenbort, E. Gutmiedl, *et al.* (2015), Appl. Phys. Lett. **107**, 21.
- Bsaisou, J., J. de Vries, C. Hanhart, S. Liebig, U.-G. Meissner, D. Minossi, A. Nogga, and A. Wirzba (2015), JHEP **03**, 104, [Erratum: JHEP05,083(2015)], arXiv:1411.5804 [hep-ph].
- Budker, D., and M. Romalis (2007), Nature Physics **3**, 227.
- Buhmann, S. (2002), Phys. Rev. A; Physical Review A” **66** (4), 10.1103/PhysRevA.66.042109.
- Burghoff, M. (2015), 2nd Status Meeting of the DFG Priority Program 1491, Wildbad Kreuth.
- Butler, P., and W. Nazarewicz (1991), Nuclear Physics A **533** (2), 249.
- Cabrera, B. (1988), journal, 312.
- Cairncross, W. B., D. N. Gresh, M. Grau, K. C. Cossel, T. S. Roussy, Y. Ni, Y. Zhou, J. Ye, and E. A. Cornell (2017), arXiv:1704.07928 [physics.atom-ph].
- Callan, C. G., and S. B. Treiman (1967), Phys. Rev. **162**, 1494.
- Callan, J., Curtis G., R. Dashen, and D. J. Gross (1976), Phys. Lett. B **63**, 334.
- Carrico, J. (1968), Phys. Rev.; Physical Review” **174** (1), 125.
- Chao, W., and M. J. Ramsey-Musolf (2014), JHEP **10**, 180, arXiv:1406.0517 [hep-ph].
- Charles, J., O. Deschamps, S. Descotes-Genon, H. Lacker, A. Menzel, S. Monteil, V. Niess, J. Ocariz, J. Orloff, A. Perez, W. Qian, V. Tisserand, K. Trabelsi, P. Urquijo, and L. Vale Silva ((CKMfitter Group)) (2015), Phys. Rev. D **91**, 073007.
- Chasman, R. (1980), Physics Letters B **96** (1), 7.
- Chibane, Y., S. K. Lamoreaux, J. M. Pendlebury, and K. F. Smith (1995), Measurement Science and Technology **6** (12), 1671.
- Chien, Y. T., V. Cirigliano, W. Dekens, J. de Vries, and E. Mereghetti (2016), JHEP **02**, 011, [JHEP02,011(2016)], arXiv:1510.00725 [hep-ph].
- Cho, D. (1991), Phys. Rev. A; Physical Review A” **44** (5), 2783.
- Chupp, T. (1990), Phys. Rev. Lett. **64** (19), 2261.
- Chupp, T. (1994), Phys. Rev. Lett. **72** (15), 2363.
- Chupp, T., and M. Ramsey-Musolf (2015), Phys. Rev. **C91** (3), 035502.
- Chupp, T. E., R. J. Hoare, R. L. Walsworth, and B. Wu (1994), Phys. Rev. Lett. **72**, 2363.
- Cirigliano, V., W. Dekens, J. de Vries, and E. Mereghetti (2016a), Phys. Rev. **D94** (3), 034031, arXiv:1605.04311 [hep-ph].
- Cirigliano, V., W. Dekens, J. de Vries, and E. Mereghetti (2016b), Phys. Rev. **D94** (1), 016002, arXiv:1603.03049 [hep-ph].
- Cirigliano, V., Y. Li, S. Profumo, and M. J. Ramsey-Musolf (2010), JHEP **1001**, 002, arXiv:0910.4589 [hep-ph].
- Cirigliano, V., S. Profumo, and M. J. Ramsey-Musolf (2006), JHEP **07**, 002, arXiv:hep-ph/0603246 [hep-ph].
- Cocks, J., *et al.* (1999), Nuclear Physics A **645** (1), 61.
- Cohen, D., U. S. S. Ahlfors, E. Hamalainen, and E. Hagren (2002), Proceedings 13th International Conference on Biomagnetism (Biomag2002), 919.
- Cohen-Tannoudji, C. (1962), Ann. Phys. **7**, 423.
- Cohen-Tannoudji, C., and S. Haroche (1969), J. Physique **30**, 153.
- Commins, E., J. Jackson, and D. DeMille (2007), American Journal of Physics **75** (6), 532.
- Commins, E., S. Ross, D. DeMille, and B. Regan (1994), Phys. Rev. A **50**, 2960.
- Commins, E. D. (1991), American Journal of Physics **59** (12), 1077.
- Commins, E. D. (1993), Physica Scripta **1993** (T46), 92.
- Commins, E. D. (1999), Advances In Atomic, Molecular, and Optical Physics **40**, 1.
- Commins, E. D. (2007), Journal of the Physical Society of Japan **76** (11), 111010, <http://dx.doi.org/10.1143/JPSJ.76.111010>.
- Contino, R., *et al.* (2016), arXiv:1606.09408 [hep-ph].
- Coveney, P., and P. Sandars (1983a), J. Phys. B. **16**, 3727.
- Coveney, P., and P. Sandars (1983b), Journal of Physics B: Atomic and Molecular Physics **16** (20), 3727.
- Coveney, P. V., and P. G. H. Sandars (1983c), Journal of Physics B: Atomic and Molecular Physics **16** (20), 3727.
- Crawford, C. (2015), private communication.
- Crewther, R., P. Di Vecchia, G. Veneziano, and E. Witten (1979), Phys. Lett. B **88**, 123.
- Curtin, D., P. Jaiswal, and P. Meade (2012), JHEP **08**, 005, arXiv:1203.2932 [hep-ph].
- Czarnecki, A., and B. Krause (1997), Phys. Rev. Lett. **78**, 4339, arXiv:hep-ph/9704355 [hep-ph].
- Dahlinger, M., E. Kankeleit, D. Habs, D. Schwalm, B. Schwartz, R. Simon, J. Burrows, and P. Butler (1988), Nuclear Physics A **484** (2), 337.

- Dang, H. B., A. C. Makoof, and M. V. Romalis (2010), Appl. Phys. Lett. **97**, 151110.
- Degenkolb, S. (2016), PhD. Dissertation - University of Michigan.
- Degenkolb, S., and T. Chupp (2011), BAPS-DAMOP 2011 **K2** (0), 10.
- Demir, D. A., OLebedev, K. A. Olive, M. Pospelov, and A. Ritz (2004), Nucl. Phys. B **680**, 339.
- Derevianko, A. (2005), Phys. Rev. A; Physical Review A” **72** (4), 10.1103/PhysRevA.72.040101.
- Dickerson, S., *et al.* (2012), Rev. Sci. Instr. **83**, 065108.
- Dimopoulos, S., and D. W. Sutter (1995), Nucl. Phys. B **452**, 496, arXiv:hep-ph/9504415 [hep-ph].
- Dine, M., and A. Kusenko (2003), Rev. Mod. Phys. **76**, 1, arXiv:hep-ph/0303065 [hep-ph].
- Dmitriev, V. F., and R. A. Sen’kov (2003), Phys. Atom. Nucl. **66**, 1940.
- Dobaczewski, J. (2015), private communication doi.
- Donoghue, J. F., B. R. Holstein, and M. Musolf (1987), Phys. Lett. **B196**, 196.
- Dress, W. B., P. D. Miller, J. M. Pendlebury, P. Perrin, and N. F. Ramsey (1977), Phys. Rev. **D15**, 9.
- Dubbers, D., and M. G. Schmidt (2011), Rev. Mod. Phys. **83**, 1111, arXiv:1105.3694 [hep-ph].
- Dzuba, V., V. Flambaum, and P. Silvestrov (1985a), Phys. Lett. **154B**, 93.
- Dzuba, V., V. Flambaum, and P. Silvestrov (1985b), Phys. Lett. B **154**, 93.
- Dzuba, V. A., V. V. Flambaum, J. S. M. Ginges, and M. Kozlov (2002), Phys. Rev. **A66**, 012111.
- Dzuba, V. A., V. V. Flambaum, and C. Harabati (2011), Phys. Rev. **A84**, 052108.
- Dzuba, V. A., V. V. Flambaum, and S. G. Porsev (2009), Phys. Rev. A **80**, 032120.
- Eckel, S., P. Hamilton, E. Kirilov, H. W. Smith, and D. DeMille (2013), Phys. Rev. **A87** (5), 052130.
- Eckel, S., A. O. Sushkov, and S. K. Lamoreaux (2012), Phys. Rev. Lett. **109**, 193003, arXiv:1208.4420 [physics.atom-ph].
- Ellis, J. R., J. S. Lee, and A. Pilaftsis (2008), JHEP **0810**, 049.
- Engel, J., J. L. Friar, and A. C. Hayes (2000), Phys. Rev. C **61**, 035502.
- Engel, J., M. J. Ramsey-Musolf, and U. van Kolck (2013), Prog.Part.Nucl.Phys. **71**, 21, arXiv:1303.2371 [nucl-th].
- Eversmann, D., *et al.* (JEDI collaboration) (2015), Phys. Rev. Lett. **115**, 094801.
- F.Allmendinger, W.Heil, S.Karpuk, W.Kilian, *et al.* (2014), Phys. Rev. Lett. **112**, 110801.
- Fang, F., and D. S. Weiss (2009), Opt. Lett. **34** (2), 169.
- Farley, F. J. M., K. Jungmann, J. P. Miller, W. M. Morse, Y. F. Orlov, B. L. Roberts, Y. K. Semertzidis, A. Silenko, and E. J. Stephenson (2004), Phys. Rev. Lett. **93**, 052001.
- Fedorov, V. V., *et al.* (2011), Phys. Lett. **B694**, 22, arXiv:1009.0153 [hep-ex].
- Feinberg, G. (1958), Phys. Rev. **112**, 1637.
- Filippone, B., *et al.* (2014), .
- Flambaum, V. (2008), Phys. Rev. **A77**, 024501.
- Flambaum, V., I. Khriplovich, and O. Sushkov (1986a), Nuclear Physics **A449**, 750.
- Flambaum, V. V., and J. S. M. Ginges (2002), Phys. Rev. A **65**, 032113.
- Flambaum, V. V., I. B. Khriplovich, and O. P. Sushkov (1986b), Nucl. Phys. A **449**, 750.
- Fleig, T., and M. K. Nayak (2013), Phys. Rev. A **88**, 032514.
- Friar, J., B. Gibson, G. Payne, A. Bernstein, and T. Chupp (1990), Phys. Rev. C **42** (6), 2310.
- Fuyuto, K., and M. Ramsey-Musolf (2017), arXiv:1706.08548 [hep-ph].
- Gaffney, L. P., *et al.* (2013), Nature **497** (7448), 199.
- Garwin, R. L., and L. M. Lederman (1959), Il Nuovo Cimento (1955-1965) **11** (6), 776.
- Ginges, J., and V. Flambaum (2004), Phys. Rept. **397**, 63, arXiv:physics/0309054 [physics].
- Giudice, G., and A. Romanino (2004), Nucl. Phys. B **699**, 65, arXiv:hep-ph/0406088 [hep-ph].
- Goldemberg, J. (1963), Phys. Rev.; Physical Review” **129** (6), 2580.
- Golub, R., C. Kaufman, G. Müller, and A. Steyerl (2015), Phys. Rev. A **92**, 062123.
- Golub, R., and K. Lamoreaux (1994), Phys. Rept. **237**, 1.
- Golub, R., and M. Pendlebury (1977), Phys. Lett. **62A**, 337.
- Golub, R., D. Richardson, and S. Lamoreaux (1991), Adam Hilger.
- Gomez, E., S. Aubin, L. A. Orozco, G. D. Sprouse, E. Iskrenova-Tchoukova, and M. S. Safronova (2008), Phys. Rev. Lett. **100**, 172502.
- Gorringe, T., and D. Hertzog (2015), Progress in Particle and Nuclear Physics **84**, 73 .
- Graner, B., Y. Chen, E. G. Lindahl, and B. R. Heckel (2016), Phys. Rev. Lett. **116** (16), 161601, arXiv:1601.04339 [physics.atom-ph].
- Green, K., P. G. Harris, P. Iaydijev, D. J. R. May, *et al.* (1998), Nucl. Instr. Meth. A **404**, 381.
- Griffith, W., M. Swallows, T. Loftus, M. Romalis, B. Heckel, *et al.* (2009), Phys. Rev. Lett. **102**, 101601.
- Grzadkowski, B., M. Iskrzynski, M. Misiak, and J. Rosiek (2010), JHEP **1010**, 085, arXiv:1008.4884 [hep-ph].
- Hacıömeröğlu, S., and Y. K. Semertzidis (2014), Nuclear Instruments and Methods in Physics Research Section A: Accelerators, Spectrometers, Detectors and Associated Equipment **743**, 96 .
- von Hahn, R., *et al.* (2016), Review of Scientific Instruments **87** (6), 063115, <http://dx.doi.org/10.1063/1.4953888>.
- Hall, L. J., and Y. Nomura (2012), JHEP **01**, 082, arXiv:1111.4519 [hep-ph].
- Harber, D. (2000), Phys. Rev. A **63** (1), 013402.
- Harrison, G. (1969), Phys. Rev. Lett. **22** (23), 1263.
- Haxton, W., and E. Henley (1983), Phys. Rev. Lett. **51**, 1937.
- Heidenreich, B. J., *et al.* (2005), Phys. Rev. Lett. **95**, 253004, arXiv:physics/0509106 [physics.atom-ph].
- Heil, W., C. Gemmel, S. Karpuk, Y. Sobolev, K. Tullney, F. Allmendinger, U. Schmidt, M. Burghoff, W. Kilian, S. Knappe-Grneberg, A. Schnabel, F. Seifert, and L. Trahms (2013), Annalen der Physik **525** (8-9), 539.
- Hinds, E. (1980), Phys. Rev. A **21** (2), 480.
- ’t Hooft, G. (1976), Phys. Rev. Lett. **37**, 8.
- Hudson, J., D. Kara, I. Smallman, B. Sauer, M. Tarbutt, *et al.* (2011), Nature **473**, 493.
- Hudson, J. J., B. E. Sauer, M. R. Tarbutt, and E. A. Hinds (2002), Phys. Rev. Lett. **89**, 023003, arXiv:hep-ex/0202014 [hep-ex].
- Ibe, M., and T. T. Yanagida (2012), Phys. Lett. **B709**, 374, arXiv:1112.2462 [hep-ph].
- Ibrahim, T., and P. Nath (1998), Phys. Rev. D **58**, 111301, arXiv:hep-ph/9807501 [hep-ph].
- Inoue, S., M. J. Ramsey-Musolf, and Y. Zhang (2014), arXiv:1403.4257 [hep-ph].
- Institut-Laue-Langevin, (2008), Yellow Book .

- Ito, T., *et al.* (2014), ArXiv **1401.5435**.
- Ito, T., *et al.* (2015), LANL Internal Report **to be published**.
- Ito, T., *et al.* (2017), private communication.
- Jackiw, R., and C. Rebbi (1976), Phys. Rev. Lett. **37**, 172.
- Jackson, J. D. (1975), *Classical Electrodynamics*, second edition ed. (John Wiley & Sons, New York).
- de Jesus, J. H., and J. Engel (2005), Phys. Rev. **C72**, 045503, arXiv:nucl-th/0507031 [nucl-th].
- Jost, R. (1957), Helv. Phys. Acta **30**, 409.
- Kane, G., P. Kumar, and J. Shao (2010), Phys. Rev. D **82**, 055005, arXiv:0905.2986 [hep-ph].
- Katz, A., M. Perelstein, M. J. Ramsey-Musolf, and P. Winslow (2015), Phys. Rev. **D92** (9), 095019, arXiv:1509.02934 [hep-ph].
- Khrplovich, I. (1998), Physics Letters B **444** (1), 98.
- Khrplovich, I. (2000a), Nuclear Physics A **663**, 147c.
- Khrplovich, I. (2000b), Hyperfine Interactions **127** (1), 365.
- Khrplovich, I. B., and S. K. Lamoreaux (1997), *CP Violation Without Strangeness: Electric Dipole Moments of Particles, Atoms, and Molecules* (Springer-Verlag Berlin Heidelberg, Berlin).
- Kim, Y. J., C.-Y. Liu, S. K. Lamoreaux, G. Visser, B. Kunkler, A. N. Matlashov, J. C. Long, and T. G. Reddy (2015), Phys. Rev. D **91**, 102004.
- Kitano, M., F. P. Calaprice, M. L. Pitt, J. Clayhold, W. Happer, M. Kadar-Kallen, M. Musolf, G. Ulm, K. Wendt, T. Chupp, J. Bonn, R. Neugart, E. Otten, and H. T. Duong (1988), Phys. Rev. Lett. **60**, 2133.
- Klinkhamer, F. R., and N. S. Manton (1984), Phys. Rev. **D30**, 2212.
- Kobayashi, M., and T. Maskawa (1973), Prog. Theor. Phys. **49**, 652.
- Koch, H.-C., G. Bison, Z. D. Grujić, W. Heil, M. Kasprzak, P. Knowles, A. Kraft, A. Pazgalev, A. Schnabel, J. Voigt, and A. Weis (2015), The European Physical Journal D **69** (8), 202.
- Kominis, I. K., T. W. Kornack, J. C. Allred, and M. V. Romalis (2003), Nature **422** (6932), 596.
- Kornack, T. W., S. J. Smullin, S.-K. Lee, and M. V. Romalis (2007), Appl. Phys. Lett. **90**, 223501.
- Kuchler, F., P. Fierlinger, and D. Wurm (2014), *Proceedings, 25th International Nuclear Physics Conference (INPC 2013)*, EPJ Web Conf. **66**, 05011.
- Kuchler, F., *et al.* (2016), *Proceedings, 6th International Symposium on Symmetries in Subatomic Physics (SSP 2015): Victoria, BC, Canada, June 8-12, 2015*, Hyperfine Interact. **237** (1), 95.
- Lamoreaux, S. K., and R. Golub (2005), Phys. Rev. A **71**, 032104.
- Landau, L. (1957a), Zh. Eksp. Teor. Fiz. **32**, 405.
- Landau, L. (1957b), Soviet Phys. JETP **5** (2), 336.
- Landau, L. (1957c), Nuclear Physics **3** (1), 127.
- Lauer, T., and T. Zechlau (2013), Eur. Phys. J. A **49** (8), 104.
- Lebedev, O., and M. Pospelov (2002), Phys. Rev. Lett. **89**, 101801, arXiv:hep-ph/0204359 [hep-ph].
- Ledbetter, M., S. Pustelny, D. Budker, M. Romalis, J. Blanchard, and A. Pines (2012), Phys. Rev. Lett. **108**, 243001, arXiv:1201.4438 [physics.atom-ph].
- Lee, S.-K., and M. V. Romalis (2008), Journal of Applied Physics **103** (8), 084904, <http://dx.doi.org/10.1063/1.2885711>.
- Lee, T. D., and C. N. Yang (1957), Brookhaven National Laboratory (BNL), Upton, NY Technical Report BNL-443 (T-91).
- Leung, K. K. H., S. Ivanov, F. M. Piegsa, M. Simson, and O. Zimmer (2016), Phys. Rev. C **93**, 025501.
- Li, Y., S. Profumo, and M. Ramsey-Musolf (2009), Phys. Lett. B **673**, 95, arXiv:0811.1987 [hep-ph].
- Li, Y., S. Profumo, and M. Ramsey-Musolf (2010), JHEP **1008**, 062, arXiv:1006.1440 [hep-ph].
- Liebler, S., S. Profumo, and T. Stefaniak (2016), JHEP **04**, 143, arXiv:1512.09172 [hep-ph].
- Lins, T. (2016), PhD. Dissertation - Technical University of Muenchen.
- Liu, C.-P. (2007), Phys. Rev. C; Physical Review C" **76** (3), 035503.
- Liu, C. Y., and S. K. Lamoreaux (2004), *Proceedings, 2nd International Symposium on Cosmology and particle astrophysics (CosPA 2003)*, Mod. Phys. Lett. **A19**, 1235.
- Liu, C.-Y., S. K. Lamoreaux, A. Saunders, D. Smith, *et al.* (2003), Nucl. Instr. Meth. A **508**, 257.
- Loh, H., K. C. Cossel, M. C. Grau, K.-K. Ni, E. R. Meyer, J. L. Bohn, J. Ye, and E. A. Cornell (2013), Science **342** (6163), 1220, <http://science.sciencemag.org/content/342/6163/1220.full.pdf>.
- Lüders, G. (1954), Danske Videnskabernes Selskab, Mat.-fys. Medd. **28** (5), 0.
- Mane, S. (2008), Nuclear Instruments and Methods in Physics Research Section A: Accelerators, Spectrometers, Detectors and Associated Equipment **596** (3), 288.
- Mane, S. (2012), Nuclear Instruments and Methods in Physics Research, Section A: Accelerators, Spectrometers, Detectors and Associated Equipment **687**, 40.
- Mane, S. (2014a), Nuclear Instruments and Methods in Physics Research Section A: Accelerators, Spectrometers, Detectors and Associated Equipment **764**, 167.
- Mane, S. (2014b), Nuclear Instruments and Methods in Physics Research Section A: Accelerators, Spectrometers, Detectors and Associated Equipment **767**, 252.
- Mane, S. (2014c), Nuclear Instruments and Methods in Physics Research Section A: Accelerators, Spectrometers, Detectors and Associated Equipment **758**, 77.
- Mane, S. (2015a), Nuclear Instruments and Methods in Physics Research Section A: Accelerators, Spectrometers, Detectors and Associated Equipment **794**, 3.
- Mane, S. (2015b), Nuclear Instruments and Methods in Physics Research Section A: Accelerators, Spectrometers, Detectors and Associated Equipment **769**, 26.
- Mane, S. (2015c), Nuclear Instruments and Methods in Physics Research Section A: Accelerators, Spectrometers, Detectors and Associated Equipment **770**, 36.
- Martensson-Pendrill, A.-M. (1985), Phys. Rev. Lett. **54**, 1153.
- Martensson-Pendrill, A.-M., and P. Oster (1987), Physica Scripta **36** (3), 444.
- Masuda, Y., T. Kitagaki, K. Hatanaka, M. Higuchi, S. Ishimoto, Y. Kiyanagi, K. Morimoto, S. Muto, and M. Yoshimura (2002), Phys. Rev. Lett. **89**, 284801.
- McClintock, P. V. E., D. J. Meredith, and J. K. Wigmore (1992), journal.
- McKeen, D., M. Pospelov, and A. Ritz (2012), Phys. Rev. **D86**, 113004, arXiv:1208.4597 [hep-ph].
- McKeen, D., M. Pospelov, and A. Ritz (2013), Phys. Rev. **D87** (11), 113002, arXiv:1303.1172 [hep-ph].
- Metodiev, E., K. Huang, Y. Semertzidis, and W. Morse (2014), Physical Review Special Topics - Accelerators and Beams **17** (7), 10.1103/PhysRevSTAB.17.074002.

- Metodiev, E., *et al.* (2015), Nuclear Instruments and Methods in Physics Research Section A: Accelerators, Spectrometers, Detectors and Associated Equipment **797**, 311 .
- Meyer, E. R., and J. L. Bohn (2008), Phys. Rev. A **78**, 010502(R), arXiv:0805.0161 [physics.atom-ph].
- Miller, P. D., W. B. Dress, J. K. Baird, and N. F. Ramsey (1967), Phys. Rev. Lett. **19**, 381.
- Mohr, P. J., D. B. Newell, and B. N. Taylor (2016), Rev. Mod. Phys. **88**, 035009.
- Morrissey, D. E., and M. J. Ramsey-Musolf (2012), New J. Phys. **14**, 125003, arXiv:1206.2942 [hep-ph].
- Morse, W. M. (2011), Hyperfine Interactions **199** (1), 93.
- Morse, W. M., Y. F. Orlov, and Y. K. Semertzidis (2013), Phys. Rev. ST Accel. Beams **16**, 114001.
- Mosyagin, N., M. Kozlov, and A. Titov (1998), J. Phys. B **31**, L763.
- Müller, K. A., and H. Burkard (1979), Phys. Rev. B **19**, 3593.
- Mundy, J. N. (1983), journal **21**, 441.
- Murthy, S., D. Krause, Z. Li, and L. Hunter (1989), Phys. Rev. Lett. **63**, 965.
- Nesvishevski, V. (2002), Physics of Atomic Nuclei **65** (3), 400.
- Ng, D., and J. N. Ng (1996a), Mod. Phys. Lett. **A11**, 211, arXiv:hep-ph/9510306 [hep-ph].
- Ng, D., and J. N. Ng (1996b), Mod. Phys. Lett. **A11**, 211, arXiv:hep-ph/9510306 [hep-ph].
- Nouri, N., A. Biswas, M. A. Brown, R. Carr, B. Filippone, C. Osthelder, B. Plaster, S. Slutsky, and C. Swank (2015), JINST **10** (12), P12003, arXiv:1508.04133 [physics.ins-det].
- Nouri, N., M. A. Brown, R. Golub, and B. Plaster (2016), arXiv:1607.04691 [nucl-ex].
- Nouri, N., and B. Plaster (2014a), JINST **9** (11), P11009.
- Nouri, N., and B. Plaster (2014b), Nuclear Instruments and Methods in Physics Research Section A: Accelerators, Spectrometers, Detectors and Associated Equipment **767**, 92 .
- Nuss-Warren, S., E. Tardiff, T. Warner, G. Ball, J. Behr, T. Chupp, K. Coulter, G. Hackman, M. Hayden, M. Pearson, A. Phillips, M. Smith, and C. Svensson (2004), Nuclear Instruments and Methods in Physics Research Section A: Accelerators, Spectrometers, Detectors and Associated Equipment **533** (3), 275 .
- Olive, K. A., *et al.* (Particle Data Group) (2014), Chin. Phys. **C38**, 090001.
- Orlov, Y. F., W. M. Morse, and Y. K. Semertzidis (2006), Phys. Rev. Lett. **96**, 214802.
- Oteiza, E. R. (1992), *Search for a Permanent Electric Dipole Moment in XENON-129 Using Simultaneous HELIUM-3 Magnetometry*, Ph.D. thesis (HARVARD UNIVERSITY.).
- Parker, R., *et al.* (2015), Phys. Rev. Lett. **114** (23), 233002, arXiv:1504.07477 [nucl-ex].
- Pattie, R., *et al.* (2017), Nuclear Instruments and Methods in Physics Research Section A: Accelerators, Spectrometers, Detectors and Associated Equipment **872**, 64 .
- Patton, B., E. Zhivun, D. Hovde, and D. Budker (2014), Phys. Rev. Lett. **113** (0), 013001.
- Pen, A., T. Mastren, G. F. Peaslee, K. Petrasky, P. A. DeYoung, D. J. Morrissey, and S. E. Lapi (2014), Nuclear Instruments and Methods in Physics Research Section A: Accelerators, Spectrometers, Detectors and Associated Equipment **747**, 62 .
- Pendlebury, J. (2004), Phys. Rev. A; Physical Review A **70** (3), 10.1103/PhysRevA.70.032102.
- Pendlebury, J., and G. Greene (2014), Physics Procedia **51**, 78 .
- Pendlebury, J., W. Heil, Y. Sobolev, P. G. Harris, *et al.* (2004a), Phys. Rev. A **70**, 032102.
- Pendlebury, J. M., W. Heil, Y. Sobolev, P. G. Harris, J. D. Richardson, R. J. Baskin, D. D. Doyle, P. Geltenbort, K. Green, M. G. D. van der Grinten, P. S. Iaydjiev, S. N. Ivanov, D. J. R. May, and K. F. Smith (2004b), Phys. Rev. A **70**, 032102.
- Pendlebury, J. M., *et al.* (2015), Phys. Rev. **D92** (9), 092003, arXiv:1509.04411 [hep-ex].
- Petrov, A. N., N. S. Mosyagin, T. A. Isaev, and A. V. Titov (2007), Phys. Rev. A **76**, 030501.
- Piegsa, F. M. (2014), Physics Procedia **51**, 59 .
- Piegsa, F. M., M. Fertl, S. N. Ivanov, M. Kreuz, K. K. H. Leung, P. Schmidt-Wellenburg, T. Soldner, and O. Zimmer (2014), Phys. Rev. C **90**, 015501.
- Pignol, G., and S. Roccia (2012), Phys. Rev. A **85**, 042105.
- Pignol, G., T. Soldner, and C. Theroine (2014), Physics Procedia **51**, 3 , {ESS} Science Symposium on Neutron Particle Physics at Long Pulse Spallation Sources, {NPPatLPS} 2013.
- Plaster, B. (2015), .
- Player, M. A., and P. G. H. Sandars (1970), Journal of Physics B: Atomic and Molecular Physics **3** (12), 1620.
- Pondrom, L., *et al.* (1981), Phys. Rev. D **23** (3), 814.
- Pospelov, M., and A. Ritz (1999), Phys. Rev. Lett. **83**, 2526, arXiv:hep-ph/9904483 [hep-ph].
- Pospelov, M., and A. Ritz (2000), Nucl. Phys. B **573**, 177, arXiv:hep-ph/9908508 [hep-ph].
- Pospelov, M., and A. Ritz (2005), Ann. Phys. **318**, 119, arXiv:hep-ph/0504231 [hep-ph].
- Purcell, E. M., and N. F. Ramsey (1950), Phys. Rev. **78**, 807.
- Pustelny, S., W. Gawlik, S. M. Rochester, D. F. J. Kimball, V. V. Yashchuk, and D. Budker (2006), Phys. Rev. A **74**, 063420.
- Ramsey, N. (1982), Annual Review of Nuclear and Particle Science **32** (1), 211, <http://dx.doi.org/10.1146/annurev.ns.32.120182.001235>.
- Ramsey, N. (1984), Acta Physica Hungarica **55**, 117.
- Ramsey, N. F. (1955), Phys. Rev. **100**, 1191.
- Ramsey, N. F. (1956), *Molecular Beams* (Oxford U.P.).
- Ramsey, N. F. (1990), Annual Review of Nuclear and Particle Science **40** (1), 1, <http://dx.doi.org/10.1146/annurev.ns.40.120190.000245>.
- Ramsey-Musolf, M., and S. Su (2008), Phys. Rept. **456**, 1, arXiv:hep-ph/0612057 [hep-ph].
- Rathmann, F., A. Saleev, and N. N. Nikolaev (srEDM, JEDI) (2013a), *Proceedings, 3rd Symposium on Prospects in the Physics of Discrete Symmetries (DISCRETE 2012)*, J. Phys. Conf. Ser. **447**, 012011.
- Rathmann, F., A. Saleev, N. N. Nikolaev, the Jedi, and srEdm collaborations (2013b), Journal of Physics: Conference Series **447** (1), 012011.
- Rebrequend, (2014), journal **00** (0), 0000.
- Regan, B., E. Commins, C. Schmidt, and D. DeMille (2002a), Phys. Rev. Lett. **88**, 071805.
- Regan, B., E. Commins, C. Schmidt, and D. DeMille (2002b), Phys. Rev. Lett. **88**, 171805.
- Regan, B., E. Commins, C. Schmidt, and D. DeMille (2002c), Phys. Rev. Lett. **88**, 171805.
- Riotto, A., and M. Trodden (1999), Ann. Rev. Nucl. Part. Sci. **49**, 35, arXiv:hep-ph/9901362 [hep-ph].
- Roberts, B., V. Dzuba, and V. Flambaum (2015), Annual Review of Nuclear and Particle Science **65** (1), 63, <http://dx.doi.org/10.1146/annurev-nucl-102014-022331>.

- Romalis, M. V., W. C. Griffith, and E. N. Fortson (2001), Phys. Rev. Lett. **86**, 2505, arXiv:hep-ex/0012001.
- Rosen, M. S., T. E. Chupp, K. P. Coulter, R. C. Welsh, and S. D. Swanson (1999), Review of Scientific Instruments **70** (2), 1546.
- Rosenberry, M. (2001), Phys. Rev. Lett. **86** (1), 22.
- Sakharov, A. (1991), Soviet Physics Uspekhi **34** (5), 392.
- Salpeter, E. (1958), Phys. Rev. **112**, 1642.
- Sandars, P. (1965), Phys. Lett. **14**, 194.
- Sandars, P. (1966), Phys. Lett. **22**, 290.
- Sandars, P. (1968a), J. Phys. B. **1**, 499.
- Sandars, P. (1968b), J. Phys. B. **1**, 511.
- Sandars, P., and E. Lipworth (1964), Phys. Rev. Lett. **13** (24), 718.
- Sandars, P. G. H. (2001), Contemporary Physics **42** (2), 97, <http://dx.doi.org/10.1080/00107510010027781>.
- Saunders, A., *et al.* (2013), Rev. Sci. Instr. **84**, 013304.
- Schiff, L. (1963), Phys. Rev.; Physical Review” **132** (5), 2194.
- Schnabel, A. (2014), private communication **00** (0), 0000.
- Schropp, D. (1987), Phys. Rev. Lett. **59** (9), 991.
- Seng, C.-Y. (2015), Phys. Rev. **C91** (2), 025502, arXiv:1411.1476 [hep-ph].
- Seng, C.-Y., and M. Ramsey-Musolf (2016), arXiv:1611.08063 [hep-ph].
- Seng, C.-Y., J. de Vries, E. Mereghetti, H. H. Patel, and M. Ramsey-Musolf (2014), arXiv:1401.5366 [nucl-th].
- Sen’kov, R. (2008), Phys. Rev. A **77** (1), 014101.
- Serebrov, A., M. S. Lasakov, A. Vasiljev, I. A. Krasnoshchokova, Y. P. Rudnev, A. Fomin, V. E. Varlamov, P. Geltenbort, J. Butterworth, A. R. Young, and U. Pesavento (2003), Phys. Lett. **A313**, 373.
- Serebrov, A., N. Romanenko, O. Zhrebtssov, M. Lasakov, *et al.* (2005), Phys. Lett. **A335**, 327.
- Serebrov, A. P., *et al.* (2008), Phys. Rev. C **78**, 035505.
- Serebrov, A. P., *et al.* (2015), Phys. Rev. **C92** (5), 055501.
- Shabalin, E. (1978), Sov. J. Nucl. Phys. **28**, 75.
- Shabalin, E. (1983), Sov. Phys. Usp. **26**, 297.
- Shapiro, F. L. (1968), Soviet Physics Uspekhi **11** (3), 345.
- Shindler, A., T. Luu, and J. de Vries (2015), Phys. Rev. **D92** (9), 094518, arXiv:1507.02343 [hep-lat].
- Shull, C. G., and R. Nathans (1967), Phys. Rev. Lett. **19**, 384.
- Silenko, A. J. (2015), Journal of Physics G: Nuclear and Particle Physics **42** (7), 075109.
- Singh, G., P. Dilavore, and C. O. Alley (1972), Review of Scientific Instruments **43** (9), 1388.
- Skrinikov, L. V. (2017), ArXiv e-prints arXiv:1704.07318 [physics.atom-ph].
- Skrinikov, L. V., A. N. Petrov, and A. V. Titov (2013), J. Chem. Phys. **139**, 221103.
- Skrinikov, L. V., A. V. Titov, and V. V. Flambaum (2017), Phys. Rev. A **95**, 022512.
- Smith, J. H., E. M. Purcell, and N. F. Ramsey (1957), Phys. Rev. **108**, 120.
- Song, Y.-H., R. Lazauskas, and V. Gudkov (2013), Phys. Rev. C **87**, 015501, arXiv:1211.3762 [nucl-th].
- Spevak, V., and N. Auerbach (1995), Phys. Lett. B **359**, 254.
- Spevak, V., N. Auerbach, and V. Flambaum (1997a), Phys. Rev. **C56**, 1357.
- Spevak, V., N. Auerbach, and V. V. Flambaum (1997b), Phys. Rev. C **56**, 1357.
- Sternheimer, R. M. (1959), Phys. Rev. **113**, 828.
- Stetcu, I., C.-P. Liu, J. L. Friar, A. Hayes, and P. Navratil (2008), Phys. Lett. B **665**, 168, arXiv:0804.3815 [nucl-th].
- Steyerl, A., C. Kaufman, G. Mller, S. S. Malik, and A. M. Desai (2013), arXiv:1307.4654 [nucl-ex].
- Steyerl, A., C. Kaufman, G. Mller, S. S. Malik, A. M. Desai, and R. Golub (2014), Phys. Rev. **A89** (5), 052129, arXiv:1403.0861 [nucl-ex].
- Steyerl, A., and S. S. Malik (1989), Nucl. Instr. Meth. **A284** (0), 20.
- Stoner, R. (1996), Phys. Rev. Lett. **77** (19), 3971.
- Sumner, T. J., J. M. Pendlebury, and K. F. Smith (1987), Journal of Physics D: Applied Physics **20** (9), 1095.
- Sun, Z., M. Reisner, P. Fierlinger, A. Schnabel, S. Stuibler, and L. Li (2016), Journal of Applied Physics **119** (19), 193902, <http://dx.doi.org/10.1063/1.4949516>.
- Sushkov, A. O., S. Eckel, and S. K. Lamoreaux (2009), Phys. Rev. A **79**, 022118.
- Sushkov, A. O., S. Eckel, and S. K. Lamoreaux (2010), Phys. Rev. A **81**, 022104.
- Talman, R. M., and J. D. Talman (2015a), Phys. Rev. ST Accel. Beams **18**, 074004.
- Talman, R. M., and J. D. Talman (2015b), Phys. Rev. ST Accel. Beams **18**, 074003.
- Tang, Z., *et al.* (2017), Nucl. Instr. Meth. in Phys. Res. A **827**, 32.
- Tardiff, E. (2012), PhD. Dissertation - University of Michigan.
- Tardiff, E. R., J. A. Behr, T. E. Chupp, K. Gulyuz, R. S. Lefferts, W. Lorenzon, S. R. Nuss-Warren, M. R. Pearson, N. Pietralla, G. Rainovski, J. F. Sell, and G. D. Sprouse (2008), Phys. Rev. C **77**, 052501.
- Thiel, F., A. Schnabel, S. Knappe-Grüneberg, D. Stollfu, and M. Burghoff (2007), Review of Scientific Instruments **78** (3), 035106, <http://dx.doi.org/10.1063/1.2713433>.
- Thomas, L. (1927), The London, Edinburgh, and Dublin Philosophical Magazine and Journal of Science **3** (13), 1, <http://dx.doi.org/10.1080/14786440108564170>.
- Tureanu, A. (2013), *Proceedings, 21st International Conference on Integrable Systems and Quantum Symmetries (ISQS21)*, J. Phys. Conf. Ser. **474**, 012031.
- Viana, R., P. Lunkenheimer, J. Hemberger, R. Böhmer, and A. Loidl (1994), Phys. Rev. B **50**, 601.
- Voigt, J., S. Knappe-Grneberg, A. Schnabel, R. Krber, *et al.* (2013), Metrol. Meas. Syst. **20**, 239.
- Vold, T. (1984), Phys. Rev. Lett. **52** (25), 2229.
- de Vries, J., R. Higa, C.-P. Liu, E. Mereghetti, I. Stetcu, *et al.* (2011), Phys. Rev. C **84**, 065501, arXiv:1109.3604 [hep-ph].
- Warner, T., G. Ball, J. Behr, T. Chupp, P. Finlay, G. Hackman, M. Hayden, B. Hyland, K. Koopmans, S. Nuss-Warren, M. Pearson, A. Phillips, M. Schumaker, M. Smith, C. Svensson, and E. Tardiff (2005), Nuclear Instruments and Methods in Physics Research Section A: Accelerators, Spectrometers, Detectors and Associated Equipment **538** (13), 135 .
- Weisskopf, M. (1968), Phys. Rev. Lett. **21** (24), 1645.
- Weyers, S., B. Lipphardt, and H. Schnatz (2009), Phys. Rev. A **79**, 031803.
- Wigner, E. (1946), J. Appl. Phys. **17**, 857.
- Wilkening, D. A., N. F. Ramsey, and D. J. Larson (1984a), Phys. Rev. **A29**, 425.
- Wilkening, D. A., N. F. Ramsey, and D. J. Larson (1984b), Phys. Rev. **A29**, 425.
- Wirzba, A., J. Bsaisou, and A. Nogga (2017), Int. J. Mod. Phys. **E26** (01n02), 1740031, arXiv:1610.00794 [nucl-th].
- Wu, Z. (1990), Phys. Rev. A **42** (5), 2774.
- Xu, G., and D. J. Heinzen (1999), Phys. Rev. A **59**, R922.
- Yamanaka, N. (2017), Int. J. Mod. Phys. **E26** (4), 1730002,

- arXiv:1609.04759 [nucl-th].
- Yamanaka, N., and E. Hiyama (2016), JHEP **02**, 067, arXiv:1512.03013 [hep-ph].
- Yashchuk, V., D. Budker, and M. Zolotarev (1999), AIP Conf. Proc. l **457**, 177.
- Yoshimi, A., K. Asahi, K. Sakai, M. Tsuda, K. Yogo, H. Ogawa, T. Suzuki, and M. Nagakura (2002), Physics Letters A **304** (1-2), 13 .
- Yu, Z.-C., S. S. Malik, and R. Golub (1986), z. Phys. B - Condensed Matter **62** (62), 137.
- Zechlau, T. (2016), PhD Thesis.
- Zeldovich, Y. (1959), Sov. Phys. JETP **9**, 1389.
- Zelevinsky, V., A. Volya, and N. Auerbach (2008), Phys. Rev. C **78**, 014310.
- Zeng, X. (1985), Phys. Rev. A **31** (1), 260.
- Zhivun, E., A. Wickenbrock, B. Patton, and D. Budker (2014), Appl. Phys. Lett. **105** (0), 192406.
- Zhu, K., N. Solmeyer, C. Tang, and D. S. Weiss (2013), Phys. Rev. Lett. **111**, 243006.
- Zimmer, O. (2014a), arXiv **1406.3783** (0), doi.
- Zimmer, O. (2014b), Physics Procedia **51**, 85 .
- Zimmer, O., and R. Golub (2015), Phys. Rev. **C92** (1), 015501, arXiv:1303.1944 [physics.ins-det].
- Zimmer, O., and G. R. (2015), Phys. Rev. C. **92**, 015501.
- Zinkstok, R. T., S. Witte, W. Ubachs, W. Hogervorst, and K. S. Eikema (2006), Phys. Rev. A **73**, 061801.